OKINAWA INSTITUTE OF SCIENCE AND TECHNOLOGY
GRADUATE UNIVERSITY

Thesis submitted for the degree

Doctor of Philosophy
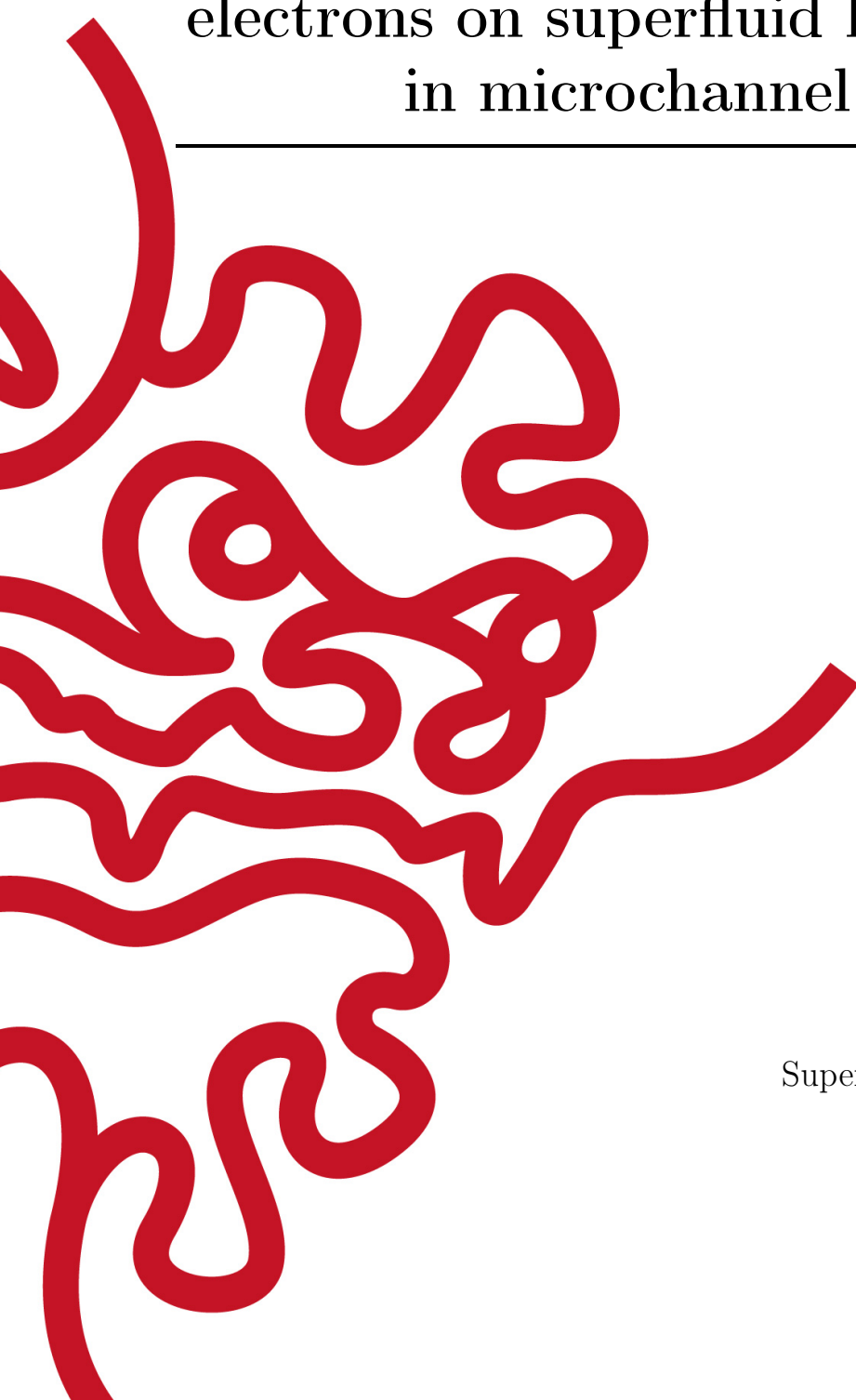
Detection of the Rydberg states of electrons on superfluid helium confined in microchannel devices

by

Shan Zou

Supervisor: **Denis Konstantinov**

July, 2022

Declaration of Original and Sole Authorship

I, Shan Zou, declare that this thesis entitled *Detection of the Rydberg states of electrons on superfluid helium confined in microchannel devices* and the data presented in it are original and my own work.

I confirm that:

- No part of this work has previously been submitted for a degree at this or any other university.

- References to the work of others have been clearly acknowledged. Quotations from the work of others have been clearly indicated, and attributed to them.

- In cases where others have contributed to part of this work, such contribution has been clearly acknowledged and distinguished from my own work.

- None of this work has been previously published elsewhere, with the exception of the following:

  S. Zou, D. Konstantinov and D. Rees, *Dynamical ordering in a 2D electron crystal confined in a narrow channel geometry*, Phys. Rev. B **104**, 045427 (2021)

  S. Zou, S. Grossenbach and D. Konstantinov, *Observation of the Rydberg Resonance in Surface Electrons on Superfluid Helium Confined in a 4-μm Deep Channel*, Journal of Low Temperature Physics, Online publication (2022)

Date: July, 2022

Signature:

Abstract

Detection of the Rydberg states of electrons on superfluid helium confined in microchannel devices

The potential for quantum information processing with surface-state electrons (SSE) on liquid helium has been pointed out in one of the historically first proposals for quantum computing [1]. The quantized Rydberg states of the vertical motion of SSE, as well as the spin states of SSE, present two promising candidates for the experimental implementation of qubit states. However, the lack of a sensitive state-readout method for a single electron has so far prevented much progress in implementation of these states for quantum computing. In order to overcome this obstacle, this PhD project seeks to lay the experimental groundwork for the realization of Rydberg state detection of SSE on liquid helium confined in microchannel devices, as well as their potential use for spin state detection. We start from the transport measurements of SSE in a microchannel setup, since well-understood transport behavior of SSE can help us to detect the Rydberg transition. An unusual transport effect is reported and discussed. By employing the time-resolved measurements, we show that the effect is due to the dynamical interaction of the electron crystal with the surface excitations of the liquid substrate. Next, the feasibility of detecting the transition between Rydberg states in a 4-μm deep channel device is demonstrated using two different methods, the conductivity method and the image-charge method. We find that the observed transition frequency for the two lowest Rydberg states, which is in the range of $0.4 - 0.5$ THz, is determined by the image charges induced by SSE in

the conducting electrodes of the microchannel device and the applied potentials, and is in a good agreement with our analytical and numerical calculations. Owing to the low sensitivity of this method, the number of SSE in the device is required to be large, on the order of 10^4, that is the sensitivity is far below the final goal of single electron readout. Taking advantage of the LC (tank) resonating circuits, we significantly improve the measurement sensitivity by employing a resonator albeit with a relatively low quality factor. Finally, we present our ongoing experimental efforts to optimize the resonator setup, in particularly increasing its quality factor, which is an important step towards realizing an ultra-sensitive readout of the single-electron Rydberg states.

Acknowledgment

First of all, I would like to acknowledge the invaluable contribution of my supervisor, Prof. Denis Konstantinov, for all the support he had given me in the past four years. His constant supports and vast knowledge of the field of electrons on helium system were essential to the completion of this thesis. I have been fortunate to complete my Ph.D. study under such a supportive and knowledgeable supervisor who builds me up as an experimentalist.

This work would also not have been possible without the help from many postdocs and technicians in our group and many other units in OIST. First, I'd like to thank Dr. Alexander Badrutdinov and Dr. Jui-Yin Lin, who taught me a lot about the nanofabrications from the beginning of my research. I am also grateful to Dr. Oleksiy Zadorozhko and Dr. Emil Joseph, for providing invaluable supports on the low temperature experiments and mechanical engineering when I was new to this lab. Many thanks to Dr. Asem Elarabi for his support on electrical engineering.

I would also like to thank all the brilliant researchers I've had collaborated with over the past few years, Dr. David Rees and Mr. Sebastian Grossenbach, for their contributing directions and discussions during my work.

Thanks also to the other present and past lab members that I did not directly work with but who gave me a new point of view during my work, Dr. Erika Kawakami, Dr. Shota Norimoto, Dr. Ivan Kostylev, Dr. Mohamed Hatifi and many others.

Abbreviations

BC	Bragg-Cherenkov
CCD	Charge-Coupled Device
Circuit QED	Circuit Quantum Electrodynamics
CPW	Coplanar-Waveguide
DL	Dimple Lattice
FEM	Finite Element Modeling
MW	Microwave
NMR	Nuclear Magnetic Resonance
PCB	Printed Circuit Board
RF	Radio Frequency
SEM	Scanning Electron Microscope
SNR	Signal-to-Noise Ratio
SSE	Surface State Electrons
ST	Sommer-Tanner
WS	Wigner Solid

Nomenclature

Some commonly used symbols in this work.

$\hat{b}_{\mathbf{q}}^{\dagger}$, $\hat{b}_{\mathbf{q}}$	Bosonic creation and annihilation operators
g	Gravitational acceleration
$\mathbf{q}$	Wave vector of ripplons
$\mathbf{k}$	In-plane wave vector of electrons
$\hbar$	Reduced Planck constant
n_s	Density of SSE
$E_{\perp}$	Pressing field exerting on SSE
Γ	Plasma parameter
k_B	Boltzmann constant
m_e	Free electron mass
m_q	Effective mass of ripplons
ϵ_0	Vacuum permittivity
α	Surface tension of liquid helium-4
σ	Electrical conductivity
ρ	Mass density of liquid helium-4
$\xi(\mathbf{r})$, ξ_q	Surface displacement and its Fourier transform
Ω_q	Dispersion relation for ripplons
μ	Electron mobility

In this thesis, all the equations are set to be in **cgs** unit, unless mentioned.

Contents

List of Figures

List of Tables

Introduction

Electrons floating on the surface of liquid helium represent a very clean, homogeneous and controllable two-dimensional electron system which has been widely used to study the behavior of strongly-correlated electron systems. Additionally, in 1999 Platzman and Dykman proposed using the quantized states of electron vertical motion as the qubit states for quantum computing [1]. The Rydberg state qubit is assumed to have sufficiently long relaxation time since the surface-state electrons (SSE) display the highest mobility among all known condensed-matter systems. However, a recent study shows that the relaxation time of the excited Rydberg states is shorter than 1 μs due to the inelastic ripplon scattering of electrons from the surface-capillary waves (ripplons) [2]. On the other hand, the spin states of surface electrons on liquid helium are expected to have extremely long coherence time (exceeding 100 s), much longer than that in any other solid-state materials, which makes SSE spins a viable resource for quantum computing [3]. It was proposed that coupling of the spin states to the Rydberg states [4] or the states of the confined lateral motion of an electron [5] can greatly facilitate the spin-state manipulation and detection, which would open a new pathway towards building a scalable quantum computer. In the above proposals, the spin-orbit coupling is introduced by creating a difference in the Zeeman splitting of the orbital states in a sufficiently strong gradient of an applied magnetic field. Most recently, the electrons trapped on the surface of solid neon were demonstrated as another promising platform for realizing qubits [6].

Successful implementation of the proposed schemes for quantum state detection and manipulation demands confinement and manipulation of electrons, at the level of a single

particle, in a some kind of microstructured device. The circuit quantum electrodynamics (circuit QED) architecture comprising of a superconducting coplanar-waveguide (CPW) resonator integrated with an electron trap has already demonstrated capability for the single-electron quantum state detection [6, 7]. The microchannel devices, which were extensively used to study the transport properties of SSE on the superfluid helium [8–11], might provide another very useful platform for such purposes. A typical device consists of an array of microchannels fabricated on a silicon substrate and filled with the superfluid helium by the capillary action. The surface of superfluid inside the channels is charged with SSE, which can be shuttled along the channels by applying ac potentials to the conducting electrodes incorporated into the channel's structure. In addition, the applied electrostatic potential provides fine control of the number of electrons in the channels, for example realizing a one-dimensional (1D) chain of electrons along the channel [12, 13]. Such devices have shown an unprecedented electron-transport efficiency by employing a charge-coupled device (CCD) configuration [14], which is well suited for building a quantum-CCD architecture proposed for the trapped-ion quantum computing [15]. Also, it was shown that the microchannel structure can be incorporated with other mesoscopic devices, such as a point-contact constriction, which enhance capabilities for charge manipulation [16].

Motivated by the possibility to realize the spin-orbit coupling of the spin states of SSE and their Rydberg states, therefore the spin state detection in SSE, this PhD project aims to lay the experimental groundwork for realization of the Rydberg state detection for SSE on liquid helium confined in a small-scale device. This thesis consists of five chapters. **Chapter 1** focuses on the relevant background theory of electrons on the surface of liquid helium. We demonstrate that many properties of this system are already well-understood theoretically, which makes it convenient to serve as a qubit system. **Chapter 2** presents an overview of the experimental methods, as well as some frequently used analytical and numerical methods for characterization of the microchannel devices. In particular,

we focus on the electric field distribution across the device and the resulting density distribution of electrons, which are of great importance for understanding the results of the transport measurements and Rydberg state detection presented in later chapters. In addition, the hydrodyanmical properties of superfluid helium in a confined structure are also discussed for the sake of improving our field distribution analysis. **Chapter 3** focuses on our transport measurements of SSE in the microchannel devices. In particular, an unusual nonequilibrium transport phenomenon is discussed based on the results of our time-resolved transport measurements. In **Chapter 4**, we present the first measurements of the microwave-excited Rydberg resonance of SSE confined in a 4-μm deep channel device, using both conductivity and image-charge detection methods. In **Chapter 5**, we demonstrate that employment of a LC helical resonator significantly increases the sensitivity of the image-charge detection. This chapter is concluded with the discussion of further improvement in the image-charge detection method towards realization of a single-electron Rydberg state detection.

Chapter 1

Electrons on superfluid helium overview

A two-dimensional electron system (2DES) is a well established scientific model in solid-state physics. It is an ensemble of electrons that is free to move in two dimensions, but tightly confined in the third direction. This tight confinement leads to quantized energy levels for motion in this direction. The surface-state electrons (SSE) on liquid helium is a system that matches this definition of 2DES. In the SSE system, electrons are bound to the surface of liquid helium forming states with hydrogen-like energy spectrum along the vertical direction. On the other hand, the in-plane motion of electrons is usually free and independent of the motion normal to the surface. The existence of SSE was predicted independently by Cole *et al.* [17] and by Shikin [18] in 1969, and later was experimentally proved by demonstrating its various properties, such as the lifetime of the surface-bound states [19–21], SSE mobility and magnetoconductivity [22–30], the liquid to solid phase transition of SSE [31–34], as well as the excitation of the quantized surface-bound (Rydberg) states [35–37].

In this chapter, following the most commonly used theoretical approaches in solid-state physics, we discuss the fundamental properties of SSE on liquid helium surface, thus laying the theoretical groundwork for the remaining parts of this thesis. In Section 1.1, we briefly summarize the general properties of the SSE system. Section 1.2 presents the Hamiltonian of a single electron for the motion perpendicular to the surface of liquid

helium, the hydrogen-like energy spectrum of this motion, and the effect of an external electric field. In Section 1.3, we extend the single electron case to a many-electron system and discuss the phase diagram and the collective in-plane motion of many electrons. Section 1.4 introduces the elementary excitations of the liquid surface, so called ripplons. We will discuss the coupling between electrons and ripplons, in particular the details of coupling of ripplons to a single electron. In Section 1.5, we reviewed electron mobility using the classical Boltzmann kinetic equation approach, while a phenomenological description of the electron mobility for SSE in solid state is given in Section 1.6. In Section 1.7, we discussed the transition linewidth of the excited Rydberg states. Finally, in Section 1.8, we briefly summarize the proposals and achievements in the realization of qubits using the electron-on-helium system.

1.1 General properties of SSE

As a clean many-body system, SSE on liquid helium exhibit some remarkable properties comparing with other condensed-matter systems. A comparison with the conventional semiconductor 2DES is listed below:

- **Effective mass:** It is well known in solid-state physics that the effective mass of an electron is obtained from the energy spectrum $E(k)$ of an electron due to its interaction with the crystal lattice, with $m^* = \frac{1}{\hbar^2} \frac{\partial^2 E}{\partial k^2}$. In this case, the effective mass is usually different from the free electron mass. For example, for electrons in GaAs, $m^* \simeq 0.067 m_e$. On the other hand, in the electrons-on-helium system SSE interact with a uniform neutralizing background due to the applied uniform electric field. As a result, the effective mass is very close to the free electron mass m_e.

- **Effective Rydberg energy and Bohr radius**: For semiconductor 2DES, the shallow levels are often described in the frame of the effective-mass-approximation with the Hamiltonian $H_{m^*} = -\frac{\hbar^2}{2m^*}\nabla^2 - \frac{e^2}{\varepsilon r} + V(z)$, where ε is the static dielec-

tric constant of the semiconductor and $V(z)$ represents the quantum well potential provided by the GaAs/AlGaAs interface [38]. For SSE, the energy spectrum of this hydrogen-like bound state is determined by the weak binding potential due to a weakly polarized liquid $\varepsilon \simeq 1$, leading to large Bohr radius and small Rydberg energy. The Rydberg energy spectrum and surface-bound states of SSE will be discussed in Section 1.2.

- **Density:** In semiconductor 2DES, the electron density is fully determined by the doping and can reach 10^{12} cm^{-2} or even higher. Thus the inter-electron distance is several nanometers, which is comparable to the thermal de Broglie wavelength λ_{de} of an electron, with $\lambda_{\mathrm{de}} = \sqrt{\frac{2\pi\hbar^2}{mk_{\mathrm{B}}T}}$, where T is the ambient temperature and k_B is the Boltzmann constant. On the other hand, the SSE system is a clear example of a classical system. In typical experiments, the density of SSE on helium surface ranges from $10^6 - 10^9$ cm^{-2}, which is limited by the hydrodynamic instability of the liquid helium [39, 40]. This gives the average distance between two adjacent electrons around $0.3 - 10$ μm. Because of the large inter-electron distance, there is no overlap between electron wavefunctions. Thus, SSE on liquid helium is a nondegenerate 2DES, even at very low temperatures. The phase diagram of SSE on liquid helium will be discussed in Section 1.3.

- **Mobility:** SSE on liquid helium have the highest known electron mobility among all known 2D electron systems due to the absence of typical scattering mechanisms presented in other systems. The highest measured mobility μ is in the order of 10^{10} cm^2 V^{-1} s^{-1} [22, 41], while in typical semiconductors $\mu \sim 10^4 - 10^7$ cm^2 V^{-1} s^{-1} [42]. The details of electron mobility and scattering mechanism will be given in Section 1.4.

Table 1.1 summarizes the basic properties of SSE on helium and 2DES in GaAs heterostructures.

	SSE (^{4}He)	GaAs/AlGaAs [38]
Effective mass (m^*/m_e)	1	0.067
Effective Rydberg Energy (K)	7.6	61.6
Effective Bohr radius (Å)	77.8	103.4
Typical surface density (cm^{-2})	$10^6 - 10^9$	$10^{11} - 10^{12}$
Mobility ($\text{cm}^2/\text{V} \cdot \text{s}$)	$10^6 - 10^{10}$	$10^4 - 10^6$

Table 1.1: Basic properties of SSE on helium and 2DES in GaAs heterostructures.

1.2 Bound state of a single electron in the vertical direction

Let's start with the case of a single electron floating on the surface of liquid helium. We consider separately the cases of zero and non-zero applied perpendicular electric field.

1.2.1 Hamiltonian of a single electron for the motion in the vertical direction

For a singe electron, as was first proposed by Cole *et al.* [17, 43], the interaction between electron and helium atoms can be described by a potential $V(z)$, where z is the distance of the electron from the helium surface, according to

$$V(z) = \begin{cases} V_{\text{rep}}, & z \leq 0 \\ V_{\text{att}} = -\Lambda e^2/(z + z_0), & z > 0. \end{cases} \tag{1.1}$$

Here, $V_{\text{rep}} \simeq 1$ eV is the short-range repulsion due to the Pauli exclusion principle, which prevents electron from entering the liquid and V_{att} is the weak attractive Coulomb potential, due to the polarization of the helium atoms. This potential can be simplified as the interaction of electron with an image-charge $e\Lambda = e(\varepsilon - 1)/4(\varepsilon + 1)$ in the liquid. In Eq. (1.1), $z_0 \approx 1$ Å is an empirical adjustable off-set parameter which accounts for the finite width of the vapor-liquid interface [44]. The motion in the z-direction is then

described by a 1D Hamiltonian

$$\hat{H}_z = -\frac{\hbar^2}{2m_e}\frac{\partial^2}{\partial z^2} + V(z), \tag{1.2}$$

where m_e is the mass of the free electron. Introducing the effective Bohr radius a_0 and Rydberg constant R_y according to

$$a_0 = \frac{\hbar^2}{\Lambda e^2 m_e}, \quad R_y = \frac{m_e \Lambda^2 e^4}{2\hbar^2}, \tag{1.3}$$

and rewriting the stationary Schrödinger equation $H_z\psi_n(z) = E_n\psi_n(z)$ in terms of the dimensionless coordinate $\xi = z/a_0$ and energy $\varepsilon_n = E_n/R_y$, we obtain the Schrödinger equation in a form

$$\left(-\frac{\partial^2}{\partial \xi^2} - \frac{2}{\xi}\right)\psi_n(\xi) = \varepsilon_n\psi_n(\xi). \tag{1.4}$$

Here, we assumed an infinite barrier $V_{\text{rep}} \to \infty$ and $z_0 = 0$ to simplify our calculations. The above equation is identical to the Schrödinger equation for the radial part of the wave function of an electron in the hydrogen atom, with the solution

$$\psi_n(z) = \frac{2}{n}\left(\frac{1}{a_0 n}\right)^{3/2} z e^{-\frac{z}{a_0 n}} L_{n-1}^{(1)}\left(\frac{2z}{a_0 n}\right), \tag{1.5}$$

where $L_n^{(\alpha)}(x) = \frac{x^{-\alpha}e^x}{n!}\frac{d^n}{dx^n}\left(e^{-x}x^{n+\alpha}\right)$ is the generalized Laguerre polynomial. Thus, the energy spectrum of such surface-bound (Rydberg) states of an electron above flat surface of liquid helium is given by

$$E_n = -\frac{R_y}{n^2} = -\frac{m_e\Lambda^2 e^4}{2\hbar^2 n^2}, \quad n = 1, 2, 3, \ldots \quad . \tag{1.6}$$

The value of Rydberg energy is $R_y = 159.123$ GHz or approximately 7.6 K, therefore for typical experimental temperatures below 1 K, the electrons freeze into the ground state of their vertical motion, thus forming a 2D system. The lowest three energy levels and the corresponding wave functions are presented in Fig. 1.1. The average distances

from the helium surface for the ground, first and second excited states are $\langle 1 | z | 1 \rangle \simeq$ 11.42 nm, $\langle 2 | z | 2 \rangle \simeq 45.66$ nm, $\langle 3 | z | 3 \rangle \simeq 102.73$ nm, respectively, which significantly exceed the atomic length scales, with the Bohr radius of electron in the hydrogen atom about 0.53 Å.
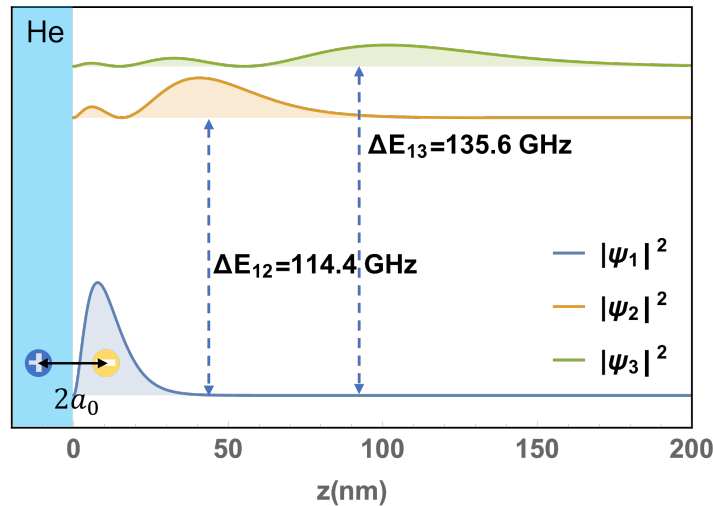
Figure 1.1: Energy spectrum and energy eigenstates of an electron bound to the surface of liquid helium. The lowest three energy levels $n = 1, 2, 3$ are shown together with the probability density of the corresponding eigenstates. The spectrum resembles that of an electron in the hydrogen or Rydberg atom.

Electrons in the ground state can be excited to the higher Rydberg states by external millimeter-wavelength electromagnetic radiation. The major process that affects the lifetime and coherence of these states is the scattering by the surface excitations (ripplons). In Section 1.4, we will work out the corresponding scattering rates.

1.2.2 Vertical states in the presence of an external electric field

Under the typical experimental conditions, electrons are bound to the surface not only by attraction to the image charges but also by an external holding electric field applied perpendicular to the liquid surface. The interaction of an electron with a uniform external field $\vec{E} = E_\perp \hat{e}_z$ results in the electron potential energy $eE_\perp z$. This allows us to vary the energy spacing between Rydberg states and tune it in resonance with MW radiation.

It can be convenient to compare the strength of the external field $E_\perp$ in terms of a characteristic electric field E_Λ, which evaluates the effective electric field due to the image charge, with $E_\Lambda = \frac{\hbar^2}{4 m_e e a_0^3} \approx 405 \, \text{V/cm}$. We start from two extreme cases:

- In the case of the weak external field $E_\perp \ll E_\Lambda$, the energy correction to the n-th energy level is given by the usual first-order perturbation theory: $\Delta E_n^{(1)} = eE_\perp \langle n| z |n\rangle$, where $|n\rangle$ corresponds to the Rydberg states in zero electric field.

- In the presence of a sufficiently strong holding field, the trapping potential $\Lambda e^2/a_0$ provided by the image charge is negligible and we have a linear trapping potential $eE_\perp z$. The eigenenergy of the Hamiltonian with a linear potential is well-known [45], $E_n = eE_\perp \zeta_n/\gamma_F$, where $\gamma_F = (2m_e eE_\perp/\hbar^2)^{1/3}$ and the discrete numbers ζ_n are related to the roots of the Airy function $\text{Ai}(z)$, with $\text{Ai}(-\zeta_n) = 0$. The corresponding wave functions are given in terms of the Airy functions $\psi_n \propto \text{Ai}[(z - \frac{\zeta_n}{\gamma_F})\gamma_F]$.

However, for most of the experimental conditions considered in this thesis we work with intermediate holding fields for which the attractive image potential is not negligible. In this case, it is difficult to work out the analytical solution for the Hamiltonian. Instead, we can numerically solve the corresponding Schrödinger equation and find the eigenenergies E_n and the corresponding eigenstates. Alternatively, one can use the variational method where the wave function can be approximated by a trial solution $\chi_n(z)$ resembling the unperturbed wave function ψ_n. E.g., the ground state trail solution can be looked for in a form $\chi(z) = 2\gamma^{3/2} z e^{-\gamma z}$, where γ is the fitting parameter determined by the condition $\partial \langle \chi| H |\chi\rangle /\partial\gamma = 0$. Fig. 1.2 shows the eigenenergies for the lowest two Rydberg states (a) and the frequency of transition from the ground state to the first excited state $(E_2 - E_1)/2\pi\hbar$ (b) obtained using three different methods. Blue lines are results obtained by numerically solving the Schrödinger equation. Red lines are results obtained by using the variational method. Green lines are the analytical Airy solutions obtained by neglecting the image charge potential. One can see that the Airy function asymptote fails for weak $E_\perp$, while for sufficiently strong $E_\perp$ the transition frequencies obtained by the three
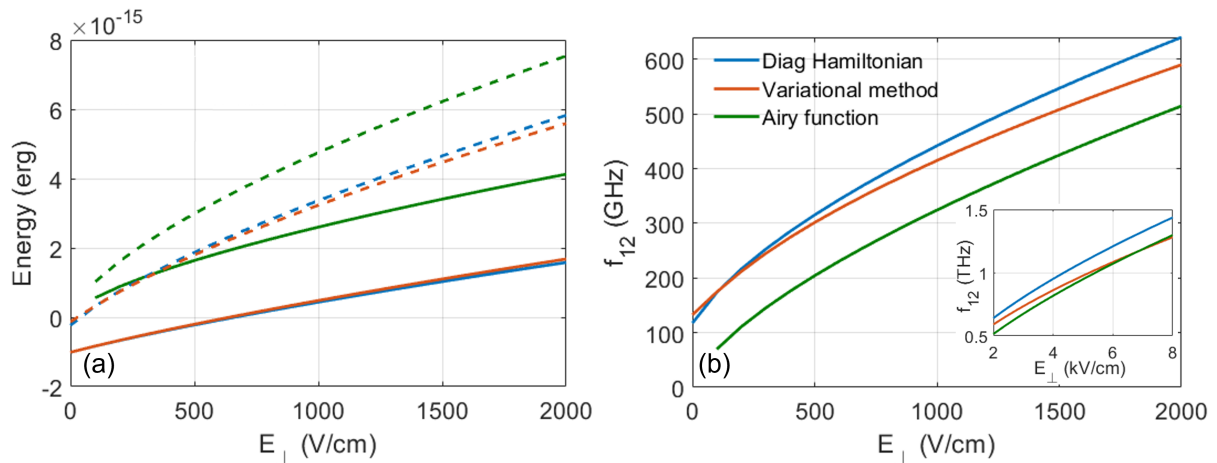
Figure 1.2: Variation of the energy level spacing due to the Stark effect. (a) The energies of the lowest two Rydberg states (solid line: $n = 1$, dashed line: $n = 2$) versus $E_\perp$. Blue lines are results from a numerical solution of the Schrödinger equation. Red lines are results obtained from the variational method. Green lines are the analytical solution of the Airy function by neglecting the image charge potential. (b) Frequency of transition from the ground state to the first excited Rydberg state as a function of the electric field strength. Inset: the same for large values of $E_\perp$.

methods are in good agreement (see inset of Fig. 1.2(b)). Also, in Ref. [46] it was shown that the variational ansatz can be given by an analytical expression

$$\frac{\gamma}{\gamma_0} = \frac{3\lambda}{4} \left\{ \sinh\left[\frac{1}{3}\sinh^{-1}\left(\frac{9\lambda}{4}\right)\right] \right\}^{-1}, \tag{1.7}$$

where $\gamma_0 = a_0^{-1}$ and $\lambda = \sqrt{E_\perp / 2E_\Lambda}$.

1.3   The in-plane motion of SSE

In the previous section, we considered the confined motion of an electron in the vertical direction. In a typical experiment, the surface of liquid helium is charged with many electrons, thus forming 2D sheet of electrons in the x-y plane. In this section, we describe the in-plane motion of such a system assuming that all SSE occupy the ground Rydberg state of the vertical motion.

1.3.1   In-plane Hamiltonian and phase diagram

The Hamiltonian for the motion parallel to the helium surface for an infinitely large electron system can be written as

$$H^{2D} = K_e + U_C = \sum_i \frac{p_i^2}{2m_e} + \frac{1}{2} \sum_{\mathbf{k}, i \neq j} \frac{2\pi e^2}{k} e^{i\mathbf{k} \cdot (\mathbf{r}_i - \mathbf{r}_j)}, \tag{1.8}$$

where first term represents the in-plane kinetic energy K_e, and the second term is the 2D Fourier transform of the Coulomb interaction energy $U_C = e^2/|\mathbf{r}_i - \mathbf{r}_j| = \sum_{\mathbf{k}}(2\pi e^2/k)e^{i\mathbf{k} \cdot (\mathbf{r}_i - \mathbf{r}_j)}$, where $k = |\mathbf{k}|$ and $\mathbf{r}_i$ is the coordinate of i-th electrons. One should note that the image charges and external holding electric field $E_\perp$ provide a uniform positive background, thus does not affect the in-plane Hamiltonian, whereas for a 2DES in semiconductor the neutralizing background is provided by the atomic lattice, which imposes a periodic potential on electrons and results in the energy band structure [47].

Phase diagram and Wigner solid

It was pointed out by Wigner [48] in 1934 that a degenerate Fermi gas/liquid is not the only possible ground state for an interacting electron system. A 3D electron system embedded in a structureless positive background can also form lattice structure to minimize its energy at relatively low density, where the potential energy greatly exceeds the kinetic energy. This lattice structure is called the Wigner solid (WS). Later, it was suggested by Crandall and Platzman [49, 50] that a similar phenomenon should occur in low-dimensional systems, such as the SSE system on helium. From the 2D Hamiltonian given by Eq. (1.8) one can see that the phase diagram of a 2D electron system is determined by the competition between the long-range Coulomb interaction and the kinetic energy of electrons. One could define a dimensionless plasma parameter Γ as the ratio of the interaction energy to the kinetic energy, $\Gamma = U_C/K_e$. The phase boundary between electron liquid and electron solid can therefore be obtained by setting the plasma parameter equal to a critical value $\Gamma = \Gamma_0$; this is the so called Lindemann criterion. The phase diagram of SSE on

a bulk liquid surface was first analyzed by Platzman and Fukuyama [50]. This study prompted an experimental search for WS in the electrons-on-helium system. The first experimental proof of Wigner crystallization was given by Grimes and Adams in 1979 [31], who measured the critical value of $\Gamma_0 \simeq 137$. This result was in good agreement with the Monte Carlo calculations which gave $\Gamma_0 = 125 \pm 15$ [51].

It is clear that the mean Coulomb energy per electron is $U_C = e^2/r_0$, where r_0 is the average distance between electrons, which is related to the electron density as $n_s = 1/\pi r_0^2$. The mean kinetic energy per particle can be evaluated using the Fermi-Dirac distribution $f(\varepsilon_k) = (\exp[(\varepsilon_k - \mu_e)/k_B T] + 1)^{-1}$ as

$$\overline{K}_e = \frac{2}{n_s} \int \frac{\mathrm{d}^2\mathbf{k}}{(2\pi)^2} \varepsilon_k f(\varepsilon_k) = \frac{m_e k_B^2 T^2}{\pi n_s \hbar^2} F(z), \tag{1.9}$$

where $z = \exp(-\mu_e/k_B T)$, $F(z) = \int_0^\infty \frac{\mathrm{d}x}{1+z\mathrm{e}^x}$, and the chemical potential μ_e is related to the electron density as

$$n_s = 2 \int \frac{\mathrm{d}^2\mathbf{k}}{(2\pi)^2} f(\varepsilon_k) = \frac{m_e k_B T}{\hbar^2} \ln\left(1 + \frac{1}{z}\right). \tag{1.10}$$

By substituting these two equations into the expression for the plasma parameter Γ, one can obtain the parametric equations for the liquid-solid boundary

$$\frac{n_s(z)}{n_c} = \frac{[\ln(1+1/z)]^4}{4F^2(z)}, \tag{1.11}$$

$$\frac{T(z)}{T^*} = \frac{[\ln(1+1/z)]^3}{2F^2(z)}, \tag{1.12}$$

where $n_c = 4/(\pi a_B^2 \Gamma_0^2)$ and $T^* = 2e^4 m/(\hbar^2 k_B \Gamma_0^2)$. For $\Gamma_0 = 137$, we have $n_c \simeq 2.43 \times 10^{12}$ cm^{-2} and $T^* \simeq 33.6$ K. The melting curve normalized in terms of the critical density n_c and critical temperature $T_c = 0.39T^*$ is shown in Fig. 1.3(a).

It is instructive to consider the high-density limit first. In order to estimate the plasma

parameter, we assume the zero-temperature limit

$$\lim_{T \to 0} f(\varepsilon_k) = \begin{cases} 1 & \text{if} \quad \varepsilon_k \leq \mu_e = \varepsilon_F \\ 0 & \text{if} \quad \varepsilon_k > \mu_e = \varepsilon_F, \end{cases} \tag{1.13}$$

where $\varepsilon_F = \hbar^2/mr_0^2$ is the Fermi energy. The radius of the Fermi circle in k-space is given by $k_F = \sqrt{2\pi n_s}$. The mean kinetic energy per particle given by Eq. (1.9) then reduces to $K_e = \varepsilon_F/2$, thus the plasma parameter is given by

$$\Gamma = \frac{U_C}{K_e} = \frac{e^2}{r_0} \frac{2mr_0^2}{\hbar^2} = \frac{2r_0}{a_B} \equiv 2r_s, \tag{1.14}$$

where $a_B = \hbar^2/e^2 m$ is the Bohr radius for the hydrogen atom and r_s is the normalized inter-particle distance. Eq. (1.14) shows that in the high-density limit the plasma parameter is proportional to the inter-electron distance, which decreases with increasing electron density. In particular, for sufficiently high density, such as $r_s \ll \Gamma_0/2$, the kinetic energy $K_e \propto 1/r_s^2$ is much larger than the potential energy $U_c \propto 1/r_s$. So the system is in a degenerate Fermi liquid state.

To achieve the condition $r_s \simeq \Gamma_0/2$ at which the degenerate Fermi liquid crystallizes into a solid phase, one needs to have the density at least 10^{12} cm^{-2} of electrons. Contrarily, the typical density for electrons on helium is in the range $10^6 - 10^9$ cm^{-2}, given $r_s \sim 10^3 - 10^5$. Thus, an experimentally accessible regime is located in the low density region of the phase diagram, see Fig. 1.3(a). In this region and at finite temperature, the kinetic energy is determined by the thermal fluctuations, with $K_e = k_B T$, such that we can rewrite the the plasma parameter as $\Gamma(n_s, T) = U_C/k_B T = e^2 a_B/k_B T r_s$, which has the opposite dependence on r_s.

Fig. 1.3(b) shows the high-density asymptotic melting curve at finite temperature, which is indicated by the orange shaded area in Fig. 1.3(a), the low-temperature asymptote
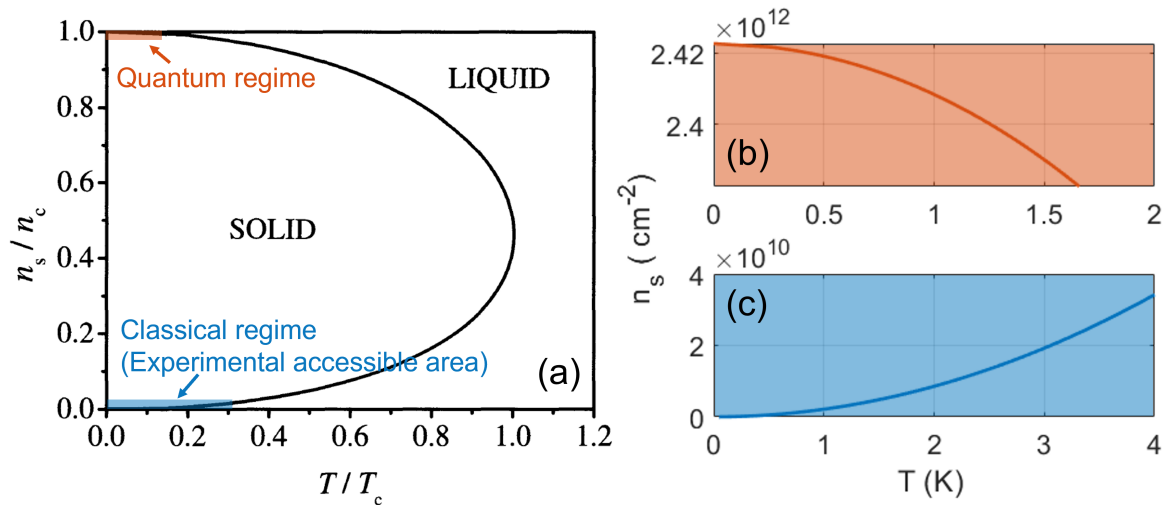
Figure 1.3: The phase diagram of SSE. (a) The normalized phase diagram obtained by Platzman *et al.*, with $n_c \simeq 2.4 \times 10^{12}$ cm^{-2} and $T_c \simeq 13.1$ K, as described in the text. The orange and blue shaded area represents the quantum and classical regimes, respectively. The figure is reproduced from Ref [44]. (b) Quantum melting curve obtained using the asymptotic solution of Eq. (1.15), as described in the text. (c): Classical melting curve given by the competition between thermal kinetic energy and Coulomb interaction, as described in the text.

of Eq. (1.11) is given by:

$$\frac{n_s}{n_c} \simeq 1 - \frac{2m_e^2}{3\hbar^4 n_s^2}(k_B T)^2.\tag{1.15}$$

In the low-density regime, the resulting melting curve is given by

$$n_s = T^2 \left(\frac{\Gamma_0 k_B}{\pi^{1/2} e^2}\right)^2,\tag{1.16}$$

and is shown in Fig. 1.3(c).

Note that the melting curve presented in Fig. 1.3(a) was obtained using an assumption that the plasma parameter is fixed to Γ_0 along the liquid-solid boundary. Other mechanisms, such as the dislocation melting (Kosterlitz-Thouless) mechanism, might affect the phase boundary [52, 53].

1.3.2 Excitations in 2DES

So far, we described the ground state of 2DES. In this section, we will outline the dispersion relation of 2DES excitations following an approache given by D. Pines [54]. Using the 2D Hamiltonian given by Eq. (1.8), together with the Hamilton's equations of motion $\dot{x}_i = \partial H/\partial p_i$ and $\dot{p}_i = -\partial H/\partial x_i$, we can obtain the corresponding equation of motion for the i-th electrons as

$$\ddot{\mathbf{r}}_i = -i\frac{2\pi e^2}{m_e}\sum_{\mathbf{k},j}\frac{\mathbf{k}}{k}\,\mathrm{e}^{i\mathbf{k}\cdot(\mathbf{r}_i-\mathbf{r}_j)}. \tag{1.17}$$

In general, the set of the above equations for $i = 1, \ldots, N$ is difficult to solve. One could simplify the problem by using the mean-field approximation and introducing the density function $\rho(\mathbf{r})$ and its Fourier transform according to

$$\rho(\mathbf{r}) = \sum_i \delta(\mathbf{r} - \mathbf{r}_i) = \sum_{\mathbf{k}} \rho_{\mathbf{k}}\mathrm{e}^{i\mathbf{k}\cdot\mathbf{r}}, \tag{1.18}$$

$$\rho_{\mathbf{k}} = \int \rho(\mathbf{r})\mathrm{e}^{-i\mathbf{k}\cdot\mathbf{r}}\mathrm{d}\mathbf{r} = \sum_i \mathrm{e}^{-i\mathbf{k}\cdot\mathbf{r}_i}. \tag{1.19}$$

Note that $\rho_{(\mathbf{k}=0)} = n_s$ represents the mean electron density, and $\rho_{\mathbf{k}}$ with $\mathbf{k} \neq 0$ describes fluctuations about the mean density n_s. Taking the time derivative

$$\frac{\mathrm{d}^2\rho_{\mathbf{k}}}{\mathrm{d}t^2} = -\sum_i[(\mathbf{k}\cdot\dot{\mathbf{r}}_i)^2 + i\mathbf{k}\cdot\ddot{\mathbf{r}}_i]\mathrm{e}^{-i\mathbf{k}\cdot\mathbf{r}_i}, \tag{1.20}$$

and substituting the equation of motion for $\ddot{\mathbf{r}}_i$, we obtain

$$\frac{\mathrm{d}^2\rho_{\mathbf{k}}}{\mathrm{d}t^2} = -\sum_i(\mathbf{k}\cdot\dot{\mathbf{r}}_i)^2\mathrm{e}^{-i\mathbf{k}\cdot\mathbf{r}_i} - \sum_{\mathbf{k}'}\frac{2\pi e^2}{m_e k'}\sum_i \mathrm{e}^{-i(\mathbf{k}-\mathbf{k}')\cdot\mathbf{r}_i}\mathbf{k}'\cdot\mathbf{k}\sum_j \mathrm{e}^{-i\mathbf{k}\cdot\mathbf{r}_j}. \tag{1.21}$$

Next, we split the second term into two parts, with $\mathbf{k}' = \mathbf{k}$ and $\mathbf{k}' \neq \mathbf{k}$. For $\mathbf{k}' \neq \mathbf{k}$, one can apply the random phase approximation with $r_0 \gg (\mathbf{k}' - \mathbf{k})^{-1}$. Then the oscillating term $\mathrm{e}^{i(\mathbf{k}'-\mathbf{k})\cdot\mathbf{r}_i}$ averages to zero by the summation over all particle coordinates. For $\mathbf{k}' = \mathbf{k}$, the summation $\sum_i \mathrm{e}^{-i(\mathbf{k}-\mathbf{k}')\cdot\mathbf{r}_i}\mathbf{k}'\cdot\mathbf{k}$ becomes $\sum_i k^2 = k^2 n_s$. Thus Eq. (1.21) can be rewritten

as

$$\frac{\mathrm{d}^2\rho_\mathbf{k}}{\mathrm{d}t^2} = -\sum_i (\mathbf{k}\cdot\dot{\mathbf{r}}_i)^2 \mathrm{e}^{-i\mathbf{k}\cdot\mathbf{r}_i} - \frac{2\pi e^2 n_s k}{m_e}\sum_i \mathrm{e}^{-i\mathbf{k}'\cdot\mathbf{r}_i}. \tag{1.22}$$

In the long-wavelength approximation with small $|\mathbf{k}| \ll r_0^{-1}$, the first term $(\mathbf{k}\cdot\dot{\mathbf{r}}_i)^2$ is negligible comparing to the second term. Thus we obtain

$$\frac{\mathrm{d}^2\rho_\mathbf{k}}{\mathrm{d}t^2} + \frac{2\pi e^2 n_s k}{m_e}\rho_\mathbf{k} = 0, \tag{1.23}$$

with the corresponding dispersion relation given by

$$\omega_k^{(l)} = \sqrt{\frac{2\pi n_s e^2 k}{m_e}}. \tag{1.24}$$

This is the well-known plasma frequency describing the collective behavior of the electrons in terms of the density oscillations. The superscript l stands for the longitudinal mode of the collective system, as we know that physically liquid can not support the transverse mode. Note that for the 3D electron system the Fourier transform of Coulomb potential is $e^2/|\mathbf{r}_i - \mathbf{r}_j| = \sum_\mathbf{k}(4\pi e^2/k^2)\mathrm{e}^{i\mathbf{k}\cdot(\mathbf{r}_i-\mathbf{r}_j)}$ and the differential equation under the long-wavelength approximation is given by $\mathrm{d}\rho_k^2/\mathrm{d}t^2 + (4\pi n_s e^2/m_e)\rho_\mathbf{k} = 0$, with the dispersion law $\omega_k^{3D} = \sqrt{4\pi n_s e^2/m_e}$.

Things become more complicated when the electron system crystallizes into solid phase. In particular, the transverse mode and longitudinal mode can coexist in WS. In the long-wavelength limit $(k \ll r_0^{-1})$, the transverse mode is acoustic, with the dispersion relation given by [55]

$$\omega_k^{(t)} = \left(0.138\frac{e^2}{m_e r_0}\right)^{1/2} k, \qquad c_t \equiv \left(0.138\frac{e^2}{m_e r_0}\right)^{1/2}. \tag{1.25}$$

In the short-wavelength limit, where the wavelength is comparable to the inter-electron distance, the dispersion relation deviates from the simple asymptotes (1.24) and (1.25). In particular, for different types of 2D Bravais lattices, the ground state phonon spectrum

of WS was calculated by Bonsall *et al.* in terms of Ewald's summation method [55].

1.4 Coupling of SSE to the environment

As any experimental system in the real world, SSE unavoidably interact with the local excitations of the environment leading to a finite electron mobility, finite life time and decoherence of the excited Rydberg states, etc. In the 2D electron system formed on the soft substrate of liquid helium, the major effect comes from the interaction of electrons with the helium vapor atoms, as well as elementary surface excitations, ripplons. Since the vapor density of helium is extremely low at the typical experimental temperatures $(T \leq 1\,\mathrm{K})$, see Fig. 1.4, we will omit the discussion of the interaction with the vapor atoms and concentrate on the interaction with ripplons.
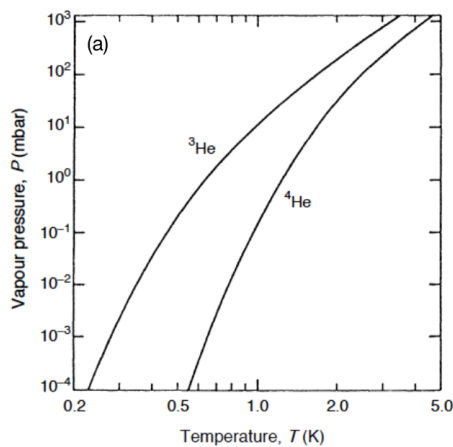
Figure 1.4: The saturated vapor pressure of ^{3}He and ^{4}He as a function of temperature.

1.4.1 Elementary surface excitations

The excitations of the surface of liquid helium, known as ripplons, can be introduced by a conventional hydrodynamical model [56–59]. In particular, they are described as the surface deformation $\xi(\mathbf{r})$ of an ideal incompressible fluid due to the gravitational force, surface tension and presence of a solid boundary at distance d below the surface.

The dynamics of fluids can be described by the well-known Euler equation, in the form $d\mathbf{v}/dt = -\nabla P/\rho$, where P is the pressure inside the liquid. Taking account the pressure due to the gravity $-\rho g \xi$ and surface tension $\alpha \nabla^2 \xi$, we can rewrite the Euler equation as

$$\rho \frac{d\mathbf{v}}{dt} = \alpha \nabla^2 \xi - \rho g \xi, \tag{1.26}$$

At the surface of the liquid helium, the velocity field of the fluid is given by the boundary condition

$$v_z = \frac{\partial \xi}{\partial t} = \frac{\partial \Phi}{\partial z}, \tag{1.27}$$

where $\Phi(\mathbf{r}, z)$ is the velocity potential of the fluid induced by the surface displacement, with $\mathbf{v} = \nabla \Phi$. Note that for the incompressible liquid the velocity potential also satisfies the Laplace equation $\nabla^2 \Phi = \nabla \cdot \mathbf{v} = 0$. By taking the time derivative of Eq. (1.26) and using the boundary condition given by Eq. (1.27), we obtain

$$\rho g \frac{\partial \Phi}{\partial z} + \rho \frac{\partial^2 \Phi}{\partial t^2} - \alpha \nabla^2 \left(\frac{\partial \Phi}{\partial z} \right) = 0. \tag{1.28}$$

Finally, using a trail solution $\Phi \sim e^{-i\Omega t} e^{qz} f(\mathbf{r})$, where $f(\mathbf{r})$ is a periodic function of $\mathbf{r}$ with period $2\pi/q$, we obtain the famous dispersion relation for surface capillary-gravity waves

$$\Omega_q^2 = \left(gq + \frac{\alpha}{\rho} q^3 \right) \tanh(qd). \tag{1.29}$$

In typical experiments using bulk helium, the liquid depth is relatively large, therefore $\tanh(qd) \to 1$. Moreover, for typical values of q the gravitational term is negligible comparing to the surface tension term. Thus, the above relation reduces to $\Omega_q = \sqrt{\alpha/\rho} q^{3/2}$. Fig. 1.5(a) plots the dispersion relation as a simplified $q^{3/2}$ law. Since the damping of ripplons is very weak in superfluid ^{4}He, the dispersion relation (1.29) can be checked experimentally in the long-wavelength limits. The first experimental observation of the break-down of the $q^{3/2}$ law due to the gravitational force at large wave vectors has been
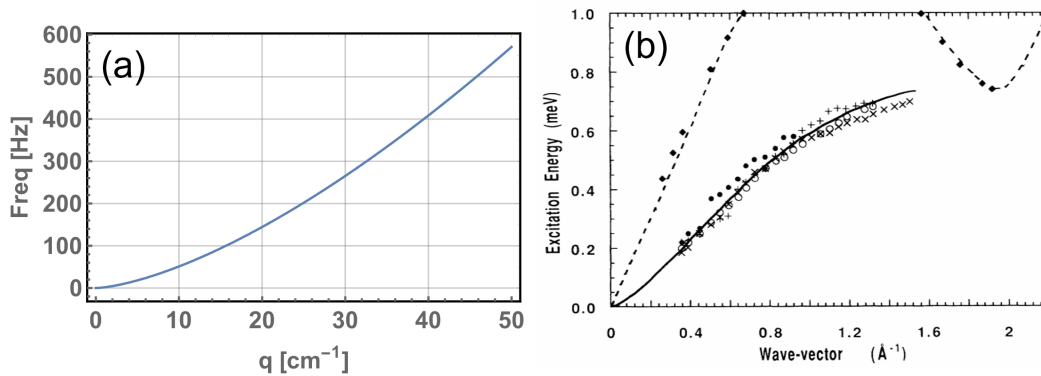
Figure 1.5: Dispersion relation of surface capillary-gravity waves. (a) $q^{3/2}$ dispersion relation in the long-wavelength limit, (b) dispersion relation in the short-wavelength limit measured by the neutron scattering techniques. Dashed line: Phonon-roton spectrum of superfluid helium at zero pressure. Solid line: ripplon spectrum predicted by Edwards's semiempirical theory of compressible liquid [58]. The figure is reproduced from Ref [60].

done by Lauter *et al.* [60]. Modifications of the dispersion relation for smaller wavelength have been done by taking into account the surface curvature and compressibility of liquid, which lowers the $q^{3/2}$ spectrum in the short-wavelength range [58, 61, 62]. Fig. 1.5(b) presents the measured data in in this regime.

In our system, most of the ripplons interacting with SSE belong to the long-wavelength region, which is known to be accurate in terms of the spectrum $\Omega_q = \sqrt{\alpha/\rho}q^{3/2}$ [44]. In the remaining parts of this chapter, we assume the $q^{3/2}$ law.

Second quantization description of ripplons

Next, we review the description of ripplons using the second quantization treatment of the quantum mechanics. Starting from the classical hydrodynamical model, the ripplon Hamiltonian is given by [63]:

$$H_r = \frac{\rho}{2} \int (\nabla \Phi)^2 \mathrm{d}^2\mathbf{r}\mathrm{d}z + \int \mathcal{F}(|\mathbf{r}' - \mathbf{r}|)\xi(\mathbf{r})\xi(\mathbf{r}')\mathrm{d}^2\mathbf{r}'\mathrm{d}\mathbf{r}, \tag{1.30}$$

where the first term denotes the kinetic energy of fluid and the second term represents the potential energy of fluid arising from the surface tension force. $\mathcal{F}(|\mathbf{r}' - \mathbf{r}|)$ is an unknown structure factor. Using periodic boundary condition, the Hamiltonian (1.30) can be expanded in terms of the wave vector $\mathbf{q}$ using $\xi(\mathbf{r}) = \frac{1}{\sqrt{S_A}} \sum_{\mathbf{q}} \xi_{\mathbf{q}} \, e^{i\mathbf{q}\cdot\mathbf{r}}$. Then, one can rewrite $\mathcal{F}$ in q-space by relating the Fourier transform $\mathcal{F}_{\mathbf{q}}$ to the ripplon spectrum Ω_q using $\Omega_q^2 = 2q\mathcal{F}_{\mathbf{q}}/\rho$.

The kinetic term can be solved by using the Green function method [63], which gives

$$
\begin{aligned}
K_e &= \frac{\rho}{4\pi S_A} \sum_{\mathbf{q},\mathbf{q}'} \dot{\xi}_{\mathbf{q}} \dot{\xi}_{\mathbf{q}'} \int \int \mathrm{d}S \mathrm{d}S' \frac{e^{i(\mathbf{q}\cdot\mathbf{r}+\mathbf{q}'\cdot\mathbf{r}')}}{|\mathbf{r} - \mathbf{r}'|}, \\
&= \frac{\rho}{2qS_A} \dot{\xi}_{\mathbf{q}} \dot{\xi}_{\text{-}\mathbf{q}} = \frac{1}{2m_q S_A} |\dot{\xi}_{\mathbf{q}}|^2.
\end{aligned}
\tag{1.31}
$$

Thus, the canonical Hamiltonian in q-space can be written as

$$
H_r = \frac{1}{S_A} \sum_{\mathbf{q}} \left(\frac{1}{2m_q} |\pi_{\mathbf{q}}|^2 + \frac{1}{2} m_q \Omega_q^2 |\xi_{\mathbf{q}}|^2 \right),
\tag{1.32}
$$

where $m_q = \rho/q$ and $\pi_{\mathbf{q}} = m_q \dot{\xi}_{\mathbf{q}}$ is the effective mass of ripplons and the generalized momentum, respectively. Note that the Hamiltonian (1.32) is identical to the expression for a harmonic oscillator. Following the standard quantization procedure of quantum mechanics, we replace $\xi_{\mathbf{q}}$ and $\pi_{\mathbf{q}}$ with operators. Note that $\hat{\xi}_{\mathbf{q}}$ and $\hat{\pi}_{\mathbf{q}}$ are Hermitian operators, which satisfy $\hat{\xi}_{\mathbf{q}}^{\dagger} = \hat{\xi}_{\text{-}\mathbf{q}}$ and $\hat{\pi}_{\mathbf{q}}^{\dagger} = \hat{\pi}_{\text{-}\mathbf{q}}$. Using orthogonality, we can verify the fundamental commutation relation $[\hat{\xi}_{\mathbf{q}}, \hat{\pi}_{\text{-}\mathbf{q}'}] = i\hbar\delta_{\mathbf{q},\mathbf{q}'}$.

One could further write the Hamiltonian $\hat{H}_r$ in the second-quantization notation by introducing the bosonic creation and annihilation operators $\hat{b}^{\dagger}$ and $\hat{b}$ according to

$$
\hat{\xi}_{\mathbf{q}} = \sqrt{\frac{\hbar}{2m_q \Omega_q}} \, (\hat{b}^{\dagger}_{-\mathbf{q}} + \hat{b}_{\mathbf{q}}),
\tag{1.33}
$$

$$
\hat{\pi}_{\mathbf{q}} = i\sqrt{\frac{\hbar m_q \Omega_q}{2}} \, (\hat{b}^{\dagger}_{-\mathbf{q}} - \hat{b}_{\mathbf{q}}),
\tag{1.34}
$$

which satisfy $[\hat{b}_{\mathbf{q}}, \hat{b}_{\mathbf{q}'}^{\dagger}] = \delta_{\mathbf{q},\mathbf{q}'}$. The Hamiltonian is therefore written as

$$\hat{H}_r = \sum_{\mathbf{q}} \hbar\Omega_q(\hat{b}_{\mathbf{-q}}^{\dagger}\hat{b}_{\mathbf{q}} + \frac{1}{2}) = \sum_{\mathbf{q}} \hbar\Omega_q(n_{\mathbf{q}} + \frac{1}{2}), \qquad (1.35)$$

where $n_{\mathbf{q}}$ denotes the occupation number of the ripplon state corresponding to the wave vector $\mathbf{q}$. This formalism permits a considerable simplification in the description of the ripplon system.

1.4.2   Coupling of ripplons to SSE

In this section, we introduce the coupling of electrons to ripplons and derive the general form of the corresponding interaction Hamiltonian. Note that the coupling of electrons to superfluid excitations is mathematically complex, leading to some lengthy calculations. For the sake of simplicity, we only focus on discussing the physical picture and derive the main results. Detailed calculations can be found in Ref. [44, 46, 63–66].

The Hamiltonian of ripplons interacting with a single electron can be written as

$$\begin{aligned}
\hat{H} &= \hat{H}_r^{(0)} + \hat{H}_e^{(0)} + \hat{H}_{\text{int}}, \\
&= \hat{H}_r^{(0)} + \frac{\hat{p}_{\|}^2}{2m} + \left[\frac{\hat{p}_{\perp}^2}{2m} + \hat{V}_e^{(0)}(z)\right] + \delta V_e,
\end{aligned} \qquad (1.36)$$

where $\hat{H}_r^{(0)}$ is the Hamiltonian of the ripplon system given by Eq. (1.35). The Hamiltonian of an electron $\hat{H}_e^{(0)}$ is treated as usual by separating it into in-plane and vertical parts, with $V_e^{(0)}(z)$ representing the potential energy of an electron on a flat helium surface

$$V_e^{(0)}(z) = V_{\text{rep}}(z) + V_{\text{att}}(z) + eE_{\perp}z. \qquad (1.37)$$

In addition in Eq. (1.36), we introduced the interaction Hamiltonian $\hat{H}_{\text{int}} \equiv \delta V_e$ as the electron energy arising from the deformation of the liquid surface $\xi(\mathbf{r})$, that is $\delta V_e = V_e^{(0)}(z + \xi(\mathbf{r})) - V_e^{(0)}(z)$. We will treat $\hat{H}_{\text{int}}$ as a perturbation and find the matrix elements

of $\hat{H}_{\text{int}}$ assuming that the unperturbed electron wave function coincides with the wave function of an electron over the flat surface. This is referred to as the Bloch approach [44].

From the general form of (1.37) we write the potential energy of an electron over the deformed surface as

$$V_e(z + \xi(\mathbf{r})) = V_{\text{rep}}(z + \xi(\mathbf{r})) + V_{\text{att}}(z + \xi(\mathbf{r})) + eE_\perp z. \qquad (1.38)$$

The polarization interaction term is obtained by considering the contribution from the helium atoms comprising the liquid with the deformed surface

$$\begin{aligned} V_{\text{att}}(z + \xi(\mathbf{r})) &= -\frac{\Lambda}{\pi} \int d^3\mathbf{R}' \frac{\theta(\xi(\mathbf{r}') - z')}{|\mathbf{R}' - \mathbf{R}|^4} \\ &= -\frac{\Lambda}{\pi} \int d^2\mathbf{r}' \int_{-\infty}^{\xi(\mathbf{r}')} \frac{dz'}{[(\mathbf{r}' - \mathbf{r})^2 + (z' - z)^2]^2}, \end{aligned} \qquad (1.39)$$

where θ is the step function, $\mathbf{R}'(\mathbf{r}', z')$ and $\mathbf{R}(\mathbf{r}, z)$ is the position vector of an element volume of liquid and an electron, respectively. Note that at $\xi = 0$, the potential $V_{\text{att}}(z + \xi(\mathbf{r})) \to V_{\text{att}}(z + 0)$ recovers the interaction potential for the flat surface, $V_{\text{att}} = -\frac{\Lambda e^2}{z}$.

The perturbative description of the repulsive term $V_{\text{rep}}(z + \xi(\mathbf{r}))$ is rather simple. For the flat surface, the repulsive barrier is simply a step function $V_0\theta(-z)$. Thus, we can write the perturbed repulsive potential as $V_{\text{rep}}(z + \xi(\mathbf{r})) = V_0\theta(\xi(\mathbf{r}) - z)$.

Finally, assuming that the unperturbed wave function of an electron coincides with the wave function over the flat surface, the potential energy provided by the external field $E_\perp$ remains the same as for the flat surface, that is $eE_\perp z$.

The interaction Hamiltonian $\hat{H}_{\text{int}} = \delta V_e$ is therefore given by

$$\begin{aligned} \delta V_e(z + \xi(\mathbf{r})) &= V_e(z + \xi(\mathbf{r})) - V_e^{(0)}(z) \\ &= V_{\text{rep}}(z + \xi(\mathbf{r})) - V_{\text{rep}}(z) + V_{\text{att}}(z + \xi(\mathbf{r})) - V_{\text{att}}(z) \\ &= \delta V_{\text{rep}} + \delta V_{\text{att}}. \end{aligned} \qquad (1.40)$$

We are interested to find the matrix elements of $\hat{H}_{\text{int}}$ over the unperturbed states, which are state products $|n\rangle\,|\mathbf{k}\rangle$, where $|n\rangle = \psi_n$ denotes the Rydberg states and $|\mathbf{k}\rangle = \frac{1}{\sqrt{S_A}}e^{i\mathbf{k}\cdot\mathbf{r}}$ represents the state of in-plane motion of an electron, and S_A is the area of liquid surface. We calculate the matrix elements of δV_{rep} and δV_{att} separately. In the following, we will use the following short notations for the matrix elements $\langle n|\cdots|n'\rangle \equiv (\cdots)_{nn'}$ and $\langle \mathbf{k}|\cdots|\mathbf{k}\rangle \equiv (\cdots)_{\mathbf{k}\mathbf{k}'}$.

Matrix element of repulsive term δV_{rep}

Using the explicit form of V_{rep} in terms of the step function, we immediately obtain

$$
\begin{aligned}
\langle n', \mathbf{k}'|\,\delta V_{\text{rep}}\,|n, \mathbf{k}\rangle &= \langle \mathbf{k}'|\,\langle n'|\,V_{\text{rep}}(z + \xi(\mathbf{r})) - V_{\text{rep}}(z)\,|n\rangle\,|\mathbf{k}\rangle \\
&= \langle \mathbf{k}'|\,V_0 \left[\int_{-\infty}^{\xi(\mathbf{r})} \psi_{n'}^*(z)\psi_n(z)\mathrm{d}z - \int_{-\infty}^{0} \psi_{n'}^*(z)\psi_n(z)\mathrm{d}z\right]|\mathbf{k}\rangle \\
&= \langle \mathbf{k}'|\,V_0 \int_{0}^{\xi(\mathbf{r})} \psi_{n'}^*(z)\psi_n(z)\mathrm{d}z\,|\mathbf{k}\rangle .
\end{aligned}
\tag{1.41}
$$

Next, we expand the wave function of the vertical motion in the Taylor series around $z = 0$

$$
\psi_n(z) = \psi_n(0) + \frac{\partial\psi_n(0)}{\partial z}z + \mathcal{O}(z^2) \simeq \psi_n(0) + \psi_n'(0)z.
\tag{1.42}
$$

Using this and keeping terms up to the second order in ξ, we obtained from Eq. (1.41)

$$
\langle n', \mathbf{k}'|\,\delta V_{\text{rep}}\,|n, \mathbf{k}\rangle \simeq V_0\psi_{n'}(0)\psi_n(0)\,\langle \mathbf{k}'|\,\xi\,|\mathbf{k}\rangle + \frac{V_0}{2}[\psi_{n'}(0)\psi_n'(0) + \psi_{n'}'(0)\psi_n(0)]\,\langle \mathbf{k}'|\,\xi^2\,|\mathbf{k}\rangle .
$$

Finally, using the continuity of the electron wave function at $z = 0$, that is $\psi_n'(0) = k_0\psi_n(0)$, where $k_0 = \sqrt{2mV_0}/\hbar$, we obtain

$$
\langle n', \mathbf{k}'|\,\delta V_{\text{rep}}\,|n, \mathbf{k}\rangle \simeq \frac{\hbar^2}{2m}\psi_{n'}'(0)\psi_n'(0)\,\langle \mathbf{k}'|\,\xi\,|\mathbf{k}\rangle + \sqrt{\frac{V_0\hbar^2}{2m}}\psi_{n'}'(0)\psi_n'(0)\,\langle \mathbf{k}'|\,\xi^2\,|\mathbf{k}\rangle .
\tag{1.43}
$$

For practical calculations, it is convenient to express the derivatives $\psi'(0)$ in terms of an integral over the interaction potential $V(z) = -\frac{\Lambda e^2}{z} + eE_\perp z$. Using the Ehrenfest theorem

$$- \langle n| \frac{\mathrm{d}V_e^{(0)}}{\mathrm{d}z} |n\rangle = \langle n| \frac{\mathrm{d}\mathbf{p}}{\mathrm{d}t} |n\rangle , \tag{1.44}$$

and the basic property of a bound state $\langle n| \mathbf{p} |n\rangle = 0$, where $\mathbf{p}$ is the operator of momentum, we have

$$\langle n| \frac{\mathrm{d}}{\mathrm{d}z} (V_0\theta(-z) + V) |n\rangle = 0 \Rightarrow -V_0\psi_n^2(0) + \left(\frac{\partial V}{\partial z}\right)_{nn} = 0. \tag{1.45}$$

Then, we immediately obtain

$$\psi_n(0) = \frac{1}{\sqrt{V_0}} \sqrt{\left(\frac{\partial V}{\partial z}\right)_{nn}} \quad \text{and} \quad \psi_n'(0) = k_0\psi_n(0) = \sqrt{\frac{2m}{\hbar^2}} \sqrt{\left(\frac{\partial V}{\partial z}\right)_{nn}}. \tag{1.46}$$

Finally, the matrix element of the repulsive part of the electron-ripplon interaction δV_{rep} up to the term quadratic in the surface deformation ξ can be represented as

$$\langle \mathbf{k}', n'| \delta V_{\mathrm{rep}} |\mathbf{k}, n\rangle = \sqrt{\left(\frac{\partial V}{\partial z}\right)_{nn} \left(\frac{\partial V}{\partial z}\right)_{n'n'}} \sum_{\mathbf{q}} Q_q'(\hat{b}_{-\mathbf{q}}^\dagger + \hat{b}_{\mathbf{q}}) \langle \mathbf{k}'| e^{i\mathbf{q}\cdot\mathbf{r}} |\mathbf{k}\rangle +$$

$$+ k_0\sqrt{\left(\frac{\partial V}{\partial z}\right)_{nn} \left(\frac{\partial V}{\partial z}\right)_{n'n'}} \sum_{\mathbf{q},\mathbf{q}'} Q_q'Q_{q'}'(\hat{b}_{-\mathbf{q}}^\dagger + \hat{b}_{\mathbf{q}})(\hat{b}_{-\mathbf{q}'}^\dagger + \hat{b}_{\mathbf{q}'}) \langle \mathbf{k}'| e^{i(\mathbf{q}+\mathbf{q}')\cdot\mathbf{r}} |\mathbf{k}\rangle. \tag{1.47}$$

Above, we used the representation of the amplitude of the surface deformation in the second-quantization form $\xi(\mathbf{r}) = S_A^{-1/2} \sum_{\mathbf{q}} \xi_{\mathbf{q}} e^{i\mathbf{q}\cdot\mathbf{r}} = \sum_{\mathbf{q}} Q_q'(\hat{b}_{-\mathbf{q}}^\dagger + \hat{b}_{\mathbf{q}})e^{i\mathbf{q}\cdot\mathbf{r}}$, where $Q_q' \equiv \sqrt{\frac{\hbar}{2m_q\Omega_q}}$, see Eq. (1.33).

Matrix element of attractive term δV_{att}

To derive the matrix element of $\langle \mathbf{k}', n' | \delta V_{\text{att}} | \mathbf{k}, n \rangle$, we recall the expression for attractive potential (1.39) and expand it in terms of z

$$\delta V_{\text{att}} = -\frac{\Lambda}{\pi} \int d^2\mathbf{r}' \left\{ \frac{\xi(\mathbf{r}')}{[(\mathbf{r}' - \mathbf{r})^2 + z^2]^2} + \frac{2z\xi^2(\mathbf{r}')}{[(\mathbf{r}' - \mathbf{r})^2 + z^2]^3} \right\}. \tag{1.48}$$

Using the table integrals

$$\int d^2\mathbf{r}' \frac{e^{i\mathbf{q}\cdot\mathbf{r}'}}{[\mathbf{r}'^2 + z^2]^2} = \frac{\pi q}{z} K_1(qz), \tag{1.49}$$

$$\int d^2\mathbf{r} \frac{e^{i(\mathbf{q}+\mathbf{q}')\cdot\mathbf{r}'}}{[\mathbf{r}'^2 + z^2]^3} = \frac{\pi |\mathbf{q}+\mathbf{q}'|^2}{4z^2} K_2(|\mathbf{q}+\mathbf{q}'|z), \tag{1.50}$$

where K_n ($n = 1, 2$) is the modified Bessel function of second kind [67]. The matrix elements of δV_{att} over the electron states can be represented as

$$\langle \mathbf{k}', n' | \delta V_{\text{att}} | \mathbf{k}, n \rangle = -\sum_{\mathbf{q}} Q'_q (\hat{b}^\dagger_{-\mathbf{q}} + \hat{b}_{\mathbf{q}}) \langle n' | \frac{\Lambda q}{z} K_1(qz) | n \rangle \langle \mathbf{k}' | e^{i\mathbf{q}\cdot\mathbf{r}} | \mathbf{k} \rangle -$$

$$-\sum_{\mathbf{q},\mathbf{q}'} Q'_q Q'_{q'} (\hat{b}^\dagger_{-\mathbf{q}} + \hat{b}_{\mathbf{q}})(\hat{b}^\dagger_{-\mathbf{q}'} + \hat{b}_{\mathbf{q}'}) \langle n' | \frac{\Lambda |\mathbf{q}+\mathbf{q}'|^2}{2z} K_2(|\mathbf{q}+\mathbf{q}'|z) | n \rangle \langle \mathbf{k}' | e^{i(\mathbf{q}+\mathbf{q}')\cdot\mathbf{r}} | \mathbf{k} \rangle. \tag{1.51}$$

Representation of matrix element of the δV_e

Finally, the matrix element of $\delta V_e = \delta V_{\text{rep}} + \delta V_{\text{att}}$ is given by the summation of Eq. (1.47) and (1.51). The term linear in the surface deformation ξ represents the one-ripplon scattering processes, while the term proportional to ξ^2 corresponds to the two-ripplon scattering processes. Again, for practical calculations it is convenient to rearrange the expression for the one-ripplon scattering elements. We add and subtract a term

$$\left(\frac{\partial V}{\partial z} \right)_{n'n} = \left(\frac{\Lambda e^2}{z^2} + eE_\perp \right)_{n'n} = \left(\frac{\Lambda e^2}{z^2} \right)_{n'n} + eE_\perp \delta_{n'n} \tag{1.52}$$

into the corresponding expression. Then, the summation of Eq. (1.47) and (1.51) can be represented as

$$
\langle \mathbf{k}', n' | \, \delta V_e \, | n, \mathbf{k} \rangle = \sum_{\mathbf{q}} Q'_q (\hat{b}^{\dagger}_{-\mathbf{q}} + \hat{b}_{\mathbf{q}}) \left(\mathrm{e}^{i\mathbf{q}\cdot\mathbf{r}} \right)_{\mathbf{k}'\mathbf{k}} \times
$$

$$
\left\{ \Lambda q^2 \left(\frac{1}{(qz)^2} - \frac{K_1(qz)}{qz} \right)_{nn'} + \left[\sqrt{\left(\frac{\partial V}{\partial z} \right)_{nn} \left(\frac{\partial V}{\partial z} \right)_{n'n'}} - \left(\frac{\partial V}{\partial z} \right)_{n'n} \right] + eE_{\perp}\delta_{n'n} \right\} +
$$

$$
\sum_{\mathbf{q},\mathbf{q}'} Q'_q Q'_{q'} (\hat{b}^{\dagger}_{-\mathbf{q}} + \hat{b}_{\mathbf{q}})(\hat{b}^{\dagger}_{-\mathbf{q}'} + \hat{b}_{\mathbf{q}'}) \left(\mathrm{e}^{i(\mathbf{q}+\mathbf{q}')\cdot\mathbf{r}} \right)_{\mathbf{k}'\mathbf{k}} \times
$$

$$
\left[k_0 \sqrt{\left(\frac{\partial V}{\partial z} \right)_{nn} \left(\frac{\partial V}{\partial z} \right)_{n'n'}} - \left(\frac{\Lambda|\mathbf{q}' + \mathbf{q}|^2}{2z} K_2(|\mathbf{q} + \mathbf{q}'|z) \right)_{nn'} \right] \qquad (1.53)
$$

It is convenient to represent this result in a more compact form

$$
(\delta V_e)_{\mathbf{k}\mathbf{k}',nn'} = \sum_{\mathbf{q}} \hat{\xi}_{\mathbf{q}} U_{\mathbf{q}}(z)(\mathrm{e}^{i\mathbf{q}\cdot\mathbf{r}})_{\mathbf{k}\mathbf{k}'} + \sum_{\mathbf{q}'\mathbf{q}} \hat{\xi}_{\mathbf{q}'} \hat{\xi}_{\mathbf{q}} U_{\mathbf{q}'\mathbf{q}}(z)[\mathrm{e}^{i(\mathbf{q}'+\mathbf{q})\cdot\mathbf{r}}]_{\mathbf{k}\mathbf{k}'} \qquad (1.54)
$$

$$
= (\hat{H}^{\mathrm{1r}}_{\mathrm{int}})_{\mathbf{k}\mathbf{k}',nn'} + (\hat{H}^{\mathrm{2r}}_{\mathrm{int}})_{\mathbf{k}\mathbf{k}',nn'}, \qquad (1.55)
$$

where $\xi_{\mathbf{q}} = Q'_q(\hat{b}^{\dagger}_{-\mathbf{q}} + \hat{b}_{\mathbf{q}})$, while $U_{\mathbf{q}}(z)$ and $U_{\mathbf{q}'\mathbf{q}}(z)$ are given by the expressions in curly and square brackets in Eq. (1.53), respectively.

In addition to the Bloch approach, there is another treatment of the electron-ripplon interaction called the adiabatic approximation. The motion of the surface deformation is considerably slower than the motion of an electron, providing the wave number of corresponding ripplons is sufficiently small. For such ripplons, the electron wave function is adjusted adiabatically to follow the slow motion of the surface displacement ξ. In other words, the electron wave function is assumed to be zero at the uneven helium surface. Contrarily, in the perturbative Bloch approach, the unperturbed wave function is assumed to coincide with that over a flat surface. Fig. 1.6 illustrates these two approach. It can be shown that for the long-wavelength ripplons, which are relevant for the elastic one-ripplon scattering of SSE, both approaches give the same result for the matrix elements. However, the adiabatic approximation fails for the short-wavelength ripplons, which are relevant for
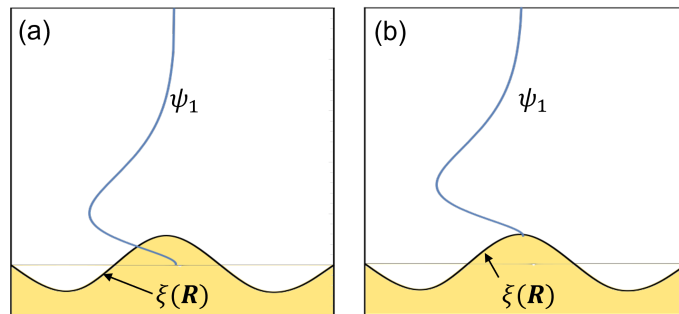
Figure 1.6: The difference between the Bloch (a) and adiabatic (b) approaches.
The blue curve represents the ground state probability density of a single electron, while
the black curve represents the uneven helium surface.

the inelastic two-ripplon emission processes. In particular, the adiabatic approach gives a
strong divergence of the corresponding matrix elements. Contrarily, the Bloch treatment
of the inelastic two-ripplon scattering gives an excellent agreement with the experiment [2].

1.4.3   Scattering rate of an electron

At sufficiently low temperatures below 1 K, all electrons occupy the ground Rydberg state
($n = 1$). In addition, the thermal excitation of ripplons with $k_B T \gg \hbar\Omega_q$ is not negligible.
Since ripplons are bosonic particles, we obtain

$$n_q = \frac{1}{\exp(\hbar\Omega_q/k_B T) - 1} \simeq k_B T/\hbar\Omega_q \gg 1, \qquad (1.56)$$

where n_q denotes the average occupation number of the ripplon state with the wave
number q. We denote $|N_r\rangle = |\{n_q\}\rangle$ the state of the thermally excited ripplon system.
Referring the ripplon Hamiltonian (1.35), we obtain

$$E_{N_r} = \sum_q \hbar\Omega_q \left(n_q + \frac{1}{2}\right) \simeq \sum_q \hbar\Omega_q n_q. \qquad (1.57)$$

Using the Fermi golden rule, the transition rate between the electron states $|\mathbf{k}'\rangle$ and
$|\mathbf{k}\rangle$ of in-plane motion accompanied by a single ripplon emission/absorption (one-ripplon

scattering) takes the form

$$w_{\mathbf{k'k},11} = \frac{2\pi}{\hbar} |\langle \mathbf{k}, 1, N_r| \hat{H}_{\text{int}}^{\text{1r}} |\mathbf{k'}, 1, N_r'\rangle|^2 \delta(\varepsilon_k + E_{N_r} - \varepsilon_{k'} - E_{N_r'}), \qquad (1.58)$$

where $\varepsilon_k = \hbar^2 k^2/2m$ represents the energy of electron in-plane motion and $|E_{N_r} - E_{N_r'}| = \hbar\Omega_q$ is the energy of a ripplon with the wave vector $\mathbf{q}$. Using Eq. (1.53), the explicit form of the matrix element $\hat{H}_{\text{int}}^{\text{1r}}$ is given by

$$\langle \mathbf{k}, 1, N_r| \hat{H}_{\text{int}}^{\text{1r}} |\mathbf{k'}, 1, N_r'\rangle = \sum_{\mathbf{q}} Q_q'[U_q(z)]_{11}(e^{i\mathbf{q}\cdot\mathbf{r}})_{\mathbf{k'k}} \langle N_r| \hat{b}_{-\mathbf{q}}^\dagger + \hat{b}_{\mathbf{q}} |N_r'\rangle$$

$$= \sum_{\mathbf{q}} Q_q'[U_q(z)]_{11}(e^{i\mathbf{q}\cdot\mathbf{r}})_{\mathbf{k'k}}(\sqrt{n_{\mathbf{q}}}\delta_{n_{\mathbf{q}},n_{\mathbf{q}}'-1} + \sqrt{n_{-\mathbf{q}}+1}\delta_{n_{-\mathbf{q}},n_{-\mathbf{q}}'+1}). \qquad (1.59)$$

The ripplon creation and annihilation operators act as follows:

$$\hat{b}_{\mathbf{q}}^\dagger |\cdots n_{\mathbf{q}} \cdots\rangle = \sqrt{n_{\mathbf{q}}+1} |\cdots n_{\mathbf{q}}+1\cdots\rangle, \qquad (1.60)$$

$$\hat{b}_{\mathbf{q}} |\cdots n_{\mathbf{q}} \cdots\rangle = \sqrt{n_{\mathbf{q}}} |\cdots n_{\mathbf{q}}-1\cdots\rangle. \qquad (1.61)$$

The transition rate (1.58) is therefore given by

$$w_{\mathbf{k'k},11} = \frac{2\pi}{\hbar} \sum_{\mathbf{q}} |Q_q'|^2[U_q(z)]_{11}^2[e^{i\mathbf{q}\cdot\mathbf{r}}]_{\mathbf{k'k}}^2[n_{\mathbf{q}}\delta_{n_{\mathbf{q}},n_{\mathbf{q}}'-1} + (n_{-\mathbf{q}}+1)\delta_{n_{-\mathbf{q}},n_{-\mathbf{q}}'+1}]\cdot$$

$$\cdot \delta(\varepsilon_k + \sum_q \hbar\Omega_q n_q - \varepsilon_{k'} - \sum_q \hbar\Omega_q n_q')$$

$$= \frac{2\pi}{\hbar} \sum_{\mathbf{q}} |Q_q'|^2[U_q(z)]_{11}^2[e^{i\mathbf{q}\cdot\mathbf{r}}]_{\mathbf{k'k}}^2[n_q\delta(\varepsilon_k - \varepsilon_{k'}) + (n_q+1)\delta(\varepsilon_k - \varepsilon_{k'})]$$

$$= \frac{2\pi}{\hbar} \sum_{\mathbf{q}} |Q_q'|^2[U_q(z)]_{11}^2[e^{i\mathbf{q}\cdot\mathbf{r}}]_{\mathbf{k'k}}^2(2n_q + 1)\delta(\varepsilon_k - \varepsilon_{k'}). \qquad (1.62)$$

Note that $\Omega_q = \Omega_{-q}$, $n_{\mathbf{q}} = n_{-\mathbf{q}} = n_q$. Owing to the dispersion relation of the ripplons, for $q \simeq k, k'$ we have $\hbar\Omega_q \ll \varepsilon_k, \varepsilon_{k'}$. Thus, the emission/absorption of a ripplon hardly changes the electron energy and the scattering of electron is **elastic**. For this reason, the ripplon energy $\hbar\Omega_q$ in the δ-function in Eq. (1.62) is usually neglected.

1.5 Mobility calculations for nondegenerate electrons (Semi-classical treatment)

For now, we restrict ourselves to the dilute gas transport behaviors for which the correlations between electrons are negligible. In this case we can use the single electron Hamiltonian (1.36). The single-electron mobility can be theoretically evaluated using the classical *Boltzmann kinetic equation* approach [46, 63, 66]. We start with a brief introduction to the Boltzmann kinetic theory.

1.5.1 Overview of the Boltzmann kinetic theory

The main goal of the kinetic theory is calculation of the transport coefficients. The equation of motion for each particle involved in the stochastic scattering processes is described by

$$m_e \frac{\mathrm{d}\mathbf{v}}{\mathrm{d}t} = \mathbf{F}_{\text{ext}} + \mathbf{F}_{\text{scatt}} \tag{1.63}$$

where $\mathbf{F}_{\text{ext}}$ is the external force exerted on the particles and $\mathbf{F}_{\text{scatt}}$ is the stochastic scattering force accounting for the collisions between particles and scatterers. As mentioned in Section 1.3.2, it is difficult to solve the equations of motion for a many-electron system. Alternatively, it is convenient to consider the distribution function of an electron ensemble. The distribution function $f(\mathbf{r}, \mathbf{p}, t)$ accounts for the momentum distribution of electrons in the phase space, while the scattering and the external driving continuously transfer an electron from one $\mathbf{k}$-state to another. Therefore, all the transport properties can be evaluated if the distribution function is known. At equilibrium, the distribution function is simply the Fermi-Dirac function. The time evolution of the distribution is described by the *Boltzmann transport equation* (BTE) having the general form

$$\frac{\mathrm{d}f}{\mathrm{d}t} = \left(\frac{\partial f}{\partial t}\right)_{\text{ext}} + \left(\frac{\partial f}{\partial t}\right)_{\text{diff}} + \left(\frac{\partial f}{\partial t}\right)_{\text{scatt}}, \tag{1.64}$$

where the "ext" term corresponds to the applied external force, the "diff" term represents the diffusion of particles, and "scatt" is the contribution due to the scattering. Expanding $\mathrm{d}f/\mathrm{d}t$ in terms of the partial derivative of $\mathbf{r}, \mathbf{p}$ and t, one can get the explicit form of BTE

$$\frac{\mathrm{d}f}{\mathrm{d}t} = \frac{\partial f}{\partial t} + \frac{\mathbf{p}}{m} \cdot \nabla f + \mathbf{F}_{\mathrm{ext}} \cdot \nabla_{\mathbf{p}} f. \tag{1.65}$$

The terms on the right hand side indicate, respectively, the explicit dependence of the distribution function on time, space, and momentum. Here, we denote $\mathbf{F}_{\mathrm{ext}} = \mathrm{d}\mathbf{p}/\mathrm{d}t$ the external force applied to the system. In most of our experiments, the force is provided by an electric field applied parallel to the surface, with $\mathbf{F}_{\mathrm{ext}} = -e\mathbf{E}_{\parallel}$. In addition, we assume that the electron system has a uniform density profile ($\nabla f = 0$), that is there is no diffusion terms due to the density gradient. Therefore, Eq. (1.65) reduces to

$$\frac{\partial f}{\partial t} - e\mathbf{E}_{\parallel} \cdot \frac{1}{\hbar}\frac{\partial f}{\partial \mathbf{k}} = \left(\frac{\partial f}{\partial t}\right)_{\mathrm{scatt}}, \quad \text{with} \quad \frac{\partial f}{\partial \mathbf{k}} = \nabla_{\mathbf{k}} f. \tag{1.66}$$

The *relaxation time approximation* is widely used to evaluate the scattering term. Let us take f_0 as the distribution function at equilibrium. In the relaxation time approximation, we represent the scattering term as

$$\left(\frac{\partial f}{\partial t}\right)_{\mathrm{scatt}} = \frac{f_0 - f}{\tau_k} = \nu_k \cdot (f_0 - f), \tag{1.67}$$

where, f_0 is the Fermi distribution and $\nu_k = 1/\tau_k$ is the momentum relaxation rate, which in general can depend on the momentum of electron $\hbar k$. We assume that the deviation of the distribution function $\delta f \equiv f - f_0$ is due to the external field. The significance of the momentum relaxation time τ_k can be understood if the electric field is switched off instantaneously. Then, the scattering term will bring the out-of-equilibrium system back to the equilibrium state with the distribution function f_0 during a characteristic time τ_k.

Using the above expression, the BTE (1.66) can be written as

$$\frac{\partial f}{\partial t} - e\mathbf{E}_{\parallel} \cdot \frac{1}{\hbar}\frac{\partial f}{\partial \mathbf{k}} = -\nu_k \cdot \delta f. \tag{1.68}$$

Exact solutions of this equation have been proven to exist in many cases, depending on the expressions for ν_k. Nevertheless, numerical methods are generally used to find an approximate solution. In the following section, we will derive an explicit expression for the ν_k for the electron-on-helium system.

For a slowly varying external field, which gives the rate of change much smaller than the relaxation rate ν_k, we can use the *steady-state condition*, $\frac{\partial f}{\partial t} \simeq 0$. In addition, for the state close to the equilibrium we have $\frac{\partial f}{\partial \varepsilon_k} \simeq \frac{\partial f_0}{\partial \varepsilon_k}$, with $\varepsilon_k = \frac{\hbar^2 k^2}{2m_e}$. Thus the BTE (1.68) can be simplified further

$$\nu_k(\varepsilon_k) \cdot \delta f \simeq (\hbar \mathbf{k} \cdot \mathbf{E}_{\parallel})\frac{e}{m_e}\frac{\partial f_0}{\partial \varepsilon_k} = (\mathbf{v} \cdot e\mathbf{E}_{\parallel})\frac{\partial f_0}{\partial \varepsilon_k}. \tag{1.69}$$

Next, we proceed to the calculations of the momentum relaxation rate $\nu_k(\varepsilon_k)$.

1.5.2 Momentum relaxation rate of a single electron

In Section 1.4.3, we derived the in-plane transition rate $w_{\mathbf{k'k}}$ from $\mathbf{k'}$ to $\mathbf{k}$ state, assuming that an electron occupies the ground Rydberg state and ignoring the transitions to the higher Rydberg states. In the following, we will demonstrate how to obtain the momentum relaxation rate ν_k for the state with the momentum $\hbar\mathbf{k}$ accounting for all possible scattering events. The scattering term in the BTE can be written as

$$\left(\frac{\partial f}{\partial t}\right)_{\text{scatt}} = -\nu_k \cdot \delta f = \sum_{\mathbf{k'}}\{f(\mathbf{k'})[1 - f(\mathbf{k})]w_{\mathbf{k'k}} - f(\mathbf{k})[1 - f(\mathbf{k'})]w_{\mathbf{kk'}}\}, \tag{1.70}$$

where $[1 - f(\mathbf{k})]$ represents the probability that the state $\mathbf{k'}$ is not occupied, owing to the Pauli exclusion principle for fermions. In general, performing summation in above

expression is rather difficult. However, it can be simplified by considering some special cases. One of the most commonly used assumption is the *elastic scattering*, in which the energy of the electrons remains unchanged after the collision. Using the fact that an elastic transition is reversible, that is $w_{\mathbf{kk'}} = w_{\mathbf{k'k}}$, Eq. (1.70) reduces to $-\nu_k \cdot \delta f = \sum_{\mathbf{k'}} w_{\mathbf{k'k}}[f(\mathbf{k'}) - f(\mathbf{k})]$.

We could further evaluate the above expression by finding the expression of the non-equilibrium distribution function f. In the presence of a driving field $E_{//}$, the electrons acquire an additional drift velocity $\mathbf{v}_{\mathrm{drif}}$. The total velocity of an electron is given by $\mathbf{v}_{\mathrm{tot}} = \mathbf{v} + \mathbf{v}_{\mathrm{drif}}$, where $\mathbf{v} = \frac{\hbar\mathbf{k}}{m}$ is the thermal velocity, which typically satisfies $|\mathbf{v}| \gg |\mathbf{v}_{\mathrm{drif}}|$. Thus, the total kinetic energy is $m_e \mathbf{v}_{\mathrm{tot}}^2/2 \simeq \varepsilon_k + \hbar\mathbf{k} \cdot \mathbf{v}_{\mathrm{drif}}$ and the distribution function f can be written as

$$f(\varepsilon_k) = \frac{1}{\exp[(\varepsilon_k - h\mathbf{k} \cdot \mathbf{v}_{\mathrm{drif}} - \mu_e)/k_B T] + 1} \simeq f_0 - h\mathbf{k} \cdot \mathbf{v}_{\mathrm{drif}}\frac{\partial f_0}{\partial \varepsilon_k}. \qquad (1.71)$$

Plugging this into Eq. (1.70) we obtain $\nu_k = -\sum_{\mathbf{k'}} w_{\mathbf{kk'}}(\mathbf{k'} - \mathbf{k}) \cdot \mathbf{k}/k^2 = \sum_{\mathbf{k'}} w_{\mathbf{kk'}}(1 - \cos\varphi)$, where φ is the angle between $\mathbf{k'}$ and $\mathbf{k}$. The weighting factor $(1 - \cos\varphi)$ indicates that the large-angle scattering events are more important in determining the transport properties. Using the explicit expression of $w_{\mathbf{kk'}}$ given by (1.62), we obtain

$$\begin{aligned}
\nu_k &= \frac{2\pi}{\hbar} \sum_{\mathbf{k'}} \sum_{\mathbf{q}} |Q_q'|^2 [U_q(z)]_{11}^2 \frac{(\mathbf{k} - \mathbf{k'}) \cdot \mathbf{k}}{k^2}(2n_q + 1)\delta_{\mathbf{k'},\mathbf{k-q}}\delta(\varepsilon_k - \varepsilon_{k'}) \\
&= \frac{2\pi}{\hbar} \sum_{\mathbf{q}} |Q_q'|^2 [U_q(z)]_{11}^2 (\mathbf{k} \cdot \mathbf{q})(2n_q + 1)\delta(\varepsilon_{\mathbf{k}} - \varepsilon_{\mathbf{k-q}}). \qquad (1.72)
\end{aligned}$$

Note that the angle θ between $\mathbf{k}$ and $\mathbf{q}$ is related to φ by $\theta = \varphi/2 + \pi/2$, see Fig. 1.7. Thus,
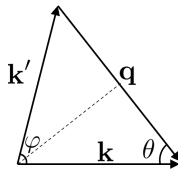
Figure 1.7: Schematics of the wave vectors in a scattering process.

we have $\cos\theta = \sin(\varphi/2)$. Replacing the summation by the integration over $\varepsilon_q = \frac{\hbar^2 q^2}{2m_e}$ and using $|\mathbf{q}| \simeq 2|\mathbf{k}|\sin(\varphi/2)$, we obtain

$$\nu_k(\varepsilon_k) = \frac{m_e}{2\pi\hbar^3} \int_0^{2\pi} \mathrm{d}\varphi(1 - \cos\varphi)\frac{\hbar V_q^2}{2m_q\Omega_q}(2n_q + 1), \qquad (1.73)$$

where we used $Q_q' = \sqrt{\frac{\hbar}{2m_q\Omega_q}}$ and replaced the coupling term $(U_q)_{11}$ by V_q, with

$$V_q \equiv \langle 1| U_q(z) |1\rangle = \Lambda q^2 \left(\frac{1}{q^2 z^2} - \frac{K_1(qz)}{qz}\right)_{11} + eE_\perp. \qquad (1.74)$$

The presence of the external field $E_\perp$ in the coupling term plays a vital role in explaining the holding field dependence of the measured mobility of SSE. In particular, for sufficiently strong holding fields we simply have $V_q \simeq eE_\perp$. Plugging $n_q \simeq \frac{k_B T}{\hbar\Omega_q} \gg 1$ into (1.73) and using $(1 - \cos\varphi) = q^2/2k^2$, we obtain

$$\nu_k(\varepsilon_k) \simeq \frac{k_B T}{8\hbar\alpha\varepsilon_k} \int_0^{2\pi} V_q^2 \mathrm{d}\varphi = \frac{\pi k_B T (eE_\perp)^2}{4\hbar\alpha\varepsilon_k}. \qquad (1.75)$$

1.5.3 Averaging over all electrons

We have so far assumed that the electron is in a well-defined state $\mathbf{k}$. In a realistic system, the measurable quantities, such as the current density, are the cumulative behavior of all electrons. Thus it is important to address the appropriate averaging procedure over all possible states. In particular, the current density can be found as $\mathbf{j} = en_s \sum_{\mathbf{k}} \mathbf{v} f(\mathbf{k}) = en_s \sum_{\mathbf{k}} \mathbf{v}\delta f$, where $\mathbf{v}$ is the velocity of electrons. Using the definition of electron conductivity $\sigma = \mathbf{j}/\mathbf{E}_{\|}$ and $\mathbf{v} \cdot \hbar\mathbf{k} = 2\varepsilon_k$, we have

$$\sigma = \frac{e^2 n_s}{m_e} \sum_{\mathbf{k}} (\mathbf{v} \cdot \hbar\mathbf{k})\frac{\partial f_0}{\partial\varepsilon_k}\frac{1}{\nu_k(\varepsilon_k)} = \frac{e^2 n_s}{m_e} \sum_{\mathbf{k}} 2\varepsilon_k \frac{\partial f_0}{\partial\varepsilon_k}\frac{1}{\nu_k(\varepsilon_k)}, \qquad (1.76)$$

Replacing $\sum_{\mathbf{k}}$ by the integration over $x = \varepsilon_k/k_B T$, we obtain the conductivity and mean scattering rate ν as

$$\sigma = \frac{e^2 n_s}{m_e \nu}, \quad \text{with} \quad \frac{1}{\nu} \equiv \int_0^\infty \frac{x \exp(-x)}{\nu_k(k_B T x)} \mathrm{d}x. \qquad (1.77)$$

Here we explicitly used the Boltzmann distribution $f_0 \sim \exp(-\varepsilon_k/k_B T)$ of SSE. The averaged relaxation time and mobility is therefore given by $\tau = 1/\nu$ and $\mu = e/m_e \nu$, respectively. For sufficiently strong holding field, $V_q \simeq e E_\perp$ we obtain a simple result

$$\nu \simeq \frac{(e E_\perp)^2}{8 \alpha \hbar}, \quad \mu = \frac{e}{m_e} \frac{8 \alpha \hbar}{(e E_\perp)^2}. \qquad (1.78)$$

The electron mobility is independent of temperature because the average number of ripplons decreases linearly with the temperature, with $n_q \simeq \frac{k_B T}{\hbar \Omega_q}$, whereas the momentum relaxation rate $\nu_k \propto 1/\varepsilon_k$ increases with decreasing T due to $\langle \varepsilon_k \rangle \propto k_B T$. These two terms compensate each other [44].

In the opposite limit of weak holding fields, $E_\perp \to 0$, the polarization term in Eq.(1.74) dominates. In this case, we need to evaluate the integral in (1.77) numerically. The result is shown by the dashed line (μ_R) in Fig. 1.8.
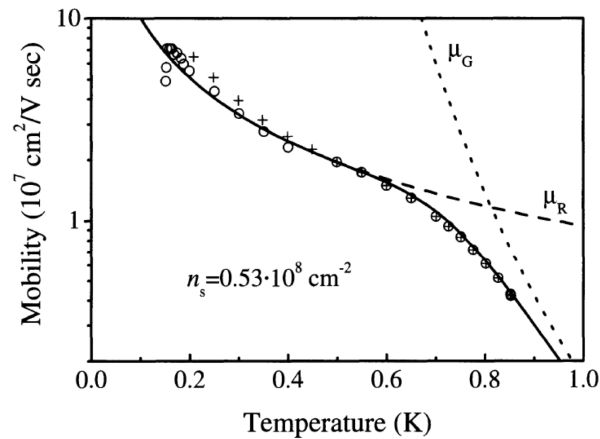
Figure 1.8: Mobility of electrons along the ^{4}He surface. μ_R and μ_G denotes the mobility due to the ripplon scattering and vapor-atom scattering, respectively. The total mobility satisfy $1/\mu_{\text{tot}} = 1/\mu_R + 1/\mu_G$. The figure is taken from [44].

If more than one scattering processes are participating in transport, the following approximate rule (Mathiesen's rule) may be used to combine their effects

$$\frac{1}{\tau_{\text{tot}}} = \sum_i \frac{1}{\tau_i}, \quad \frac{1}{\mu_{\text{tot}}} = \sum_i \frac{1}{\mu_i}, \tag{1.79}$$

where the sum is over all different scattering processes. As the temperature increases, the collision between electrons and helium vapor atoms becomes appreciable due to the increasing of vapor density. The scattering rate by vapor atoms is given by [46]

$$\nu_G = \frac{3\pi n_G A\hbar}{2m_e\gamma}, \quad \mu_G = \frac{2e\gamma}{3\pi n_G A\hbar}, \tag{1.80}$$

where $A = 4.98 \times 10^{-16} \text{cm}^2$ is the cross section of helium atom, γ is the variational ansatz given by Eq. (1.7) and $n_G = (Mk_BT/2\pi\hbar^2)^{3/2} \exp(-Q/k_BT)$ is the vapor density, with M being the mass of helium atom and $Q = 7.17$ K being the vaporization energy. The temperature dependence is shown by the dotted line (μ_G) in Fig. 1.8.

1.6   Mobility of the electron solid

The mobility of SSE is strongly modified when they crystallize into solid phase. This is due to the strongly enhanced coupling of WS to the liquid surface. In this section, we discuss the nonlinear mobility of WS in the framework of the *Bragg-Cherenkov (BC) scattering* effect. It is a generalized version of the conventional single particle Cherenkov-type emission of ripplons extended to an ordered many-particle system. This approach was first introduced by Dykman and Rubo [68]. The Cherenkov emission is the electromagnetic radiation emitted by a dielectric medium when a charged particle, such as an electron, travels through the medium with speed which exceeds the phase velocity of light in that medium. When electrons crystallize, the WS exerts pressure on the helium surface and creates a commensurate surface dimple lattice (DL), with lattice constant $a \propto \sqrt{n_s}$ coinciding with the lattice constant of the WS. Compared to the conventional single elec-

tron Cherenkov-type emission, in the presence of a lattice structure the surface waves irradiated by moving electrons can constructively interfere, giving a substantial increase in the depth of DL. The Bragg-Cherenkov scattering is just the result of this interference, where the strong enhancement of the effective mass of the coupled DL-WS system slows down its transport under a fixed driving force. Accordingly, the maximum velocity of the coupled system is limited by the phase velocity of ripplons with the first reciprocal lattice vector $G_1 = 2\pi/a$, that is $v_{\mathrm{ph}}^{\max} = \sqrt{\alpha/\rho}(2\pi/a)^{1/2}$. For the hexagonal lattice structure, we have $a = (2/\sqrt{3n_s^2})^{1/2}$, thus the maximum velocity is related to the electron density by $v_{\max} = \sqrt{\alpha/\rho}(8\pi^2 n_s/\sqrt{3})^{1/4}$.

Another interpretation to this phenomenon is based on the competition between the friction (restoring) force $\mathbf{F}_{\mathrm{res}}$ and the external driving force $\mathbf{F}_{\mathrm{ext}}$ acting on each particle. This *force balance analysis* is very convenient to describe the dynamic processes. The average friction force per electron can be evaluated as $\mathbf{F}_{\mathrm{res}} = n_s^{-1}\langle\nabla_{\mathbf{r}}\hat{H}_{\mathrm{int}}\rangle$, where $\hat{H}_{\mathrm{int}} = \sum_{\mathbf{q}} Q'_q U_q(z)\rho_{\mathbf{q}}(\hat{b}^\dagger_{-\mathbf{q}}+\hat{b}_{\mathbf{q}})$ is the Hamiltonian of interaction between ripplons and WS, with $\rho_{\mathbf{q}} = \sum_n \mathrm{e}^{i\mathbf{q}\cdot\mathbf{r}_n}$ being the electron density operator. The quantum-mechanical treatment of this friction force was given by Dykman and Rubo [68], who derived an expression

$$\mathbf{F}_{\mathrm{res}} = -\frac{n_s}{\hbar\Omega_m}\sum_{\mathbf{G}}\mathbf{G}\frac{\mathbf{G}\cdot\mathbf{v}}{\Omega(G)}|\tilde{V}_G|^2\xi(G)\left|\frac{\Omega_m}{\mathbf{G}\cdot\mathbf{v}-\Omega(G)}\right|^{1-\alpha(G)}, \text{ with} \tag{1.81}$$

$$\tilde{V}_q \equiv Q'_q|U_q|_{11}\exp\!\left(-\lambda^2 q^2/4\right) \text{ and} \tag{1.82}$$

$$\xi(G) = 2\sin[\pi\alpha(G)/2]\Gamma[1-\alpha(G)]. \tag{1.83}$$

Here, $\Omega_m = \min(\Omega_D, k_B T/\hbar)$, Ω_D is the Debye frequency of WS, λ^2 is the mean square electron displacement from the lattice site for zero temperature, and $\alpha(G) = \frac{k_B T G^2}{4\pi m c_t^2 n_s}$ accounts for the temperature dependency of the frictional force, with c_t the transverse sound velocity of the WS, see Eq. (1.25). Clearly, for very small drift velocities such that $\mathbf{G}\cdot\mathbf{v} \ll \Omega(G)$, the above equation provides a small friction force and the WS is weakly coupled to the surface dimples. The schematic drawing of the weakly coupled WS-DL sys-

tem is given by Fig. 1.9(a). As the drift velocity increases, the frictional force rises rapidly due to the decrease of the denominator in (1.81). When the system approaches the resonance condition $\mathbf{G} \cdot \mathbf{v} = \Omega(G)$, with a critical velocity $v_c = v_{\max} = \sqrt{\alpha/\rho}(8\pi^2 n_s/\sqrt{3})^{1/4}$, the friction force diverges. Accordingly, the dimple lattice is deepened and the velocity of the coupled system is locked at the terminal velocity v_c, with a zero differential mobility $dv/dF_{\text{ext}} = 0$. This schematics is shown in Fig. 1.9(b). In practice, the friction force can not be infinitely large. It always has a maximum threshold value $\mathbf{F}_{\text{res}}^{\text{th}}$, although it is difficult to define the microscopic mechanism of this threshold which depends on many experimental parameters. The decoupling of WS from DL will happen when the external force exceeds the threshold force $\mathbf{F}_{\text{ext}} > \mathbf{F}_{\text{res}}^{\text{th}}$, leading to a sudden increase of the electron velocity. This process is schematically shown in Fig. 1.9(c) and is refereed to as the sliding of the WS from DL.
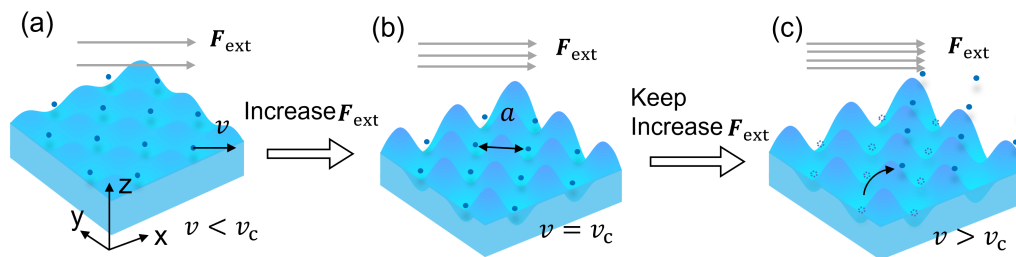
Figure 1.9: The dynamical regimes of the WS for different external driving field. (a) The WS is weakly coupled to the DL and $v < v_c$. (b) Strongly coupled WS-DL system with $v = v_c$. The deepening of DL corresponds to the rapid increase of the frictional force. (c) The WS is decoupled from the DL with $v > v_c$.

This approach to the electron mobility of WS has been experimentally tested by several groups [10, 12, 69]. In Section 3.3, we review the experimental results of the measured electron conductivity of SSE in a microchannel device. In particular, we will show a novel transport behavior in the nonequilibrium sliding regime.

1.7 Transition linewidth of the excited Rydberg states

In Section 1.4.3, we derived the in-plane transition rate $w_{\mathbf{k}'\mathbf{k},11}$ assuming that electron occupies the ground Rydberg state. As was shown, this is relevant for calculating the electron mobility. Another important property relevant for our experiments and caused by scattering of electrons is the life-time and dephasing of the excited Rydberg states. As was discussed in Section 1.2, an electron can be excited to higher-energy Rydberg states by resonant radiation. The decoherence of the n-th excited state is usually characterized by the transition linewidth Γ_{1n}. Following Ando's treatment [65], the ripplon-limited transition linewidth can be calculated including both the intra-subband and inter-subband scattering of an electron from ripplons, that is $\Gamma_{1n} = \Gamma_{\text{intra}} + \Gamma_{\text{inter}}$ according to

$$\Gamma_{1n} = \frac{\pi}{\hbar} \sum_{\mathbf{k}'} \left\langle |\langle \mathbf{k}, n| \hat{H}_{\text{int}} |\mathbf{k}', n\rangle - \langle \mathbf{k}, 1| \hat{H}_{\text{int}} |\mathbf{k}', 1\rangle |^2 \right\rangle_{\mathbf{q}} \delta(\varepsilon_k - \varepsilon_{k'}) +,$$
$$+ \frac{2\pi}{\hbar} \sum_{m \neq n} \sum_{\mathbf{k}'} \left\langle |\langle \mathbf{k}, n| \hat{H}_{\text{int}} |\mathbf{k}', m\rangle |^2 \right\rangle_{\mathbf{q}} \delta(\varepsilon_k - \varepsilon_{k'} + E_{mn}), \quad (1.84)$$

where E_{mn} is the energy separation between m-th and n-th Rydberg states and $\langle \cdots \rangle_{\mathbf{q}}$ represents the $\mathbf{q}$-summation and the thermal averaging over ripplon systems. In particular, we have $\langle \hat{\xi}_{\mathbf{q}} \hat{\xi}_{-\mathbf{q}} \rangle_{\mathbf{q}} = \sum_q \frac{\hbar q}{2\rho\Omega_q}(2n_q + 1) \simeq \sum_q \frac{qk_BT}{\rho\Omega_q}$. The term Γ_{intra} describes the in-plane elastic scattering of an electron which leads to the dephasing of a superposition state. For sufficiently strong holding fields, the polarization term in the interacting Hamiltonian is negligible, that is $\langle \mathbf{k}, n| \hat{H}_{\text{int}} |\mathbf{k}', n\rangle \simeq \langle \mathbf{k}, 1| \hat{H}_{\text{int}} |\mathbf{k}', 1\rangle$, and Γ_{intra} nearly vanishes. The second term Γ_{inter} describes the relaxation rate of the n-th Rydberg state due to scattering into Rydberg states with $m \neq n$. Comparing this with the nuclear magnetic resonance (NMR) system, Γ_{intra} corresponds to the NMR dephasing rate $(1/T_2^*)$, while Γ_{inter} corresponds to the NMR relaxation rate $(1/T_1)$.

In practice, the relaxation rate can be extracted from the spectroscopic measurements. As discussed above, the major contribution to the transition linewidth comes form the relaxation. Using spectroscopic notations, the relaxation time T_1 is related to the intrinsic

spectra linewidth by $\gamma = T_1^{-1}$. The spectroscopic measurements by Collins *et.al.* covered both vapor scattering and ripplon scattering regimes and showed a clear difference between these two regimes. At temperatures below 1 K, the ripplon scattering dominates and the spectral linewidth was measured to be on the order of 1 MHz, see Fig. 1.10. As will be shown later, in our experiments the measured linewidth is orders of magnitude larger, which is due to the inhomogeneous broadening of the transition linewidth in a nonuniform holding electric field $E_\perp$.
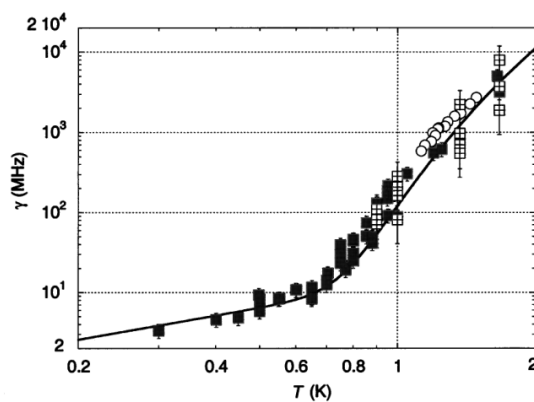
Figure 1.10: The intrinsic linewidth of SSE on ^{4}He. The closed squares and the crossed squares show the linewidth obtained experimentally in [70] and the open circles are the data obtained from [36]. The solid line is obtained from Ando's theory [65]. The figure is taken from [70].

1.8 Brief overview of qubit proposals

In this chapter, we briefly reviewed the fundamental properties of the electrons on helium system. It was shown that many properties of this system have been explored experimentally and theoretically, and by now are well-understood. In particular, the weak interaction between SSE and environment results in a relatively long decoherence time of electron motional states, which makes electrons on helium a promising candidate for quantum computing. In this section, we briefly discuss the proposals and achievements towards quantum information processing using the electron-on-helium system.

1.8.1   Charge qubits with electrons on liquid helium

The potential for quantum computing with electrons on helium has been pointed out by Platzman and Dykman [1], who proposed using the two lowest Rydberg states of a trapped electron on liquid helium as a qubit. As discussed in the previous section, the intrinsic linewidth of the resonant absorption line is in the order of 1 MHz, which promises a relatively long relaxation time on the order of $1\,\mu$s. However, the manipulation of qubit states requires an input MW radiation with the frequency in the range of hundreds of GHz, which makes it inconvenient to integrate the input MW radiation with the conventional coaxial transmission lines and the on-chip stripline technology. In addition, the lack of sensitive readout mechanism for the Rydberg states also prevented to have much progress in this direction so far.

Another promising proposal is to use the lateral quantized states of the electron motion parallel to the helium surface as qubit states [5, 7]. These lateral states can be robustly controlled using the well-developed circuit quantum electrodynamics architecture. The *circuit quantum electrodynamics* (circuit QED) studies the light-matter interaction using microwave photons, which can be regarded as an all-electrical realization of cavity QED in the microwave regime. In this platform, the single electron trap is integrated to an on-chip transmission line structure. The lateral motional state of a trapped electron can be engineered to have transition frequency of a few GHz, thus can interact with the MW photons of the transmission line resonators. Such a hybrid system has significant advantage because many parameters, such as photon lifetime, transition frequency and electron-photon coupling strengths, can be fully controlled using conventional nanofabrication and telecommunication techniques.

The coupling between a single electron on superfluid helium and a transmission line resonator has been first demonstrated by Koolstra *et al.* [7], with the measured coupling strength about 4.8 MHz. A similar experiment has been done recently with SSE on the surface of solid neon by Zhou *et al.* [6], who reported the lifetime of the excited lateral
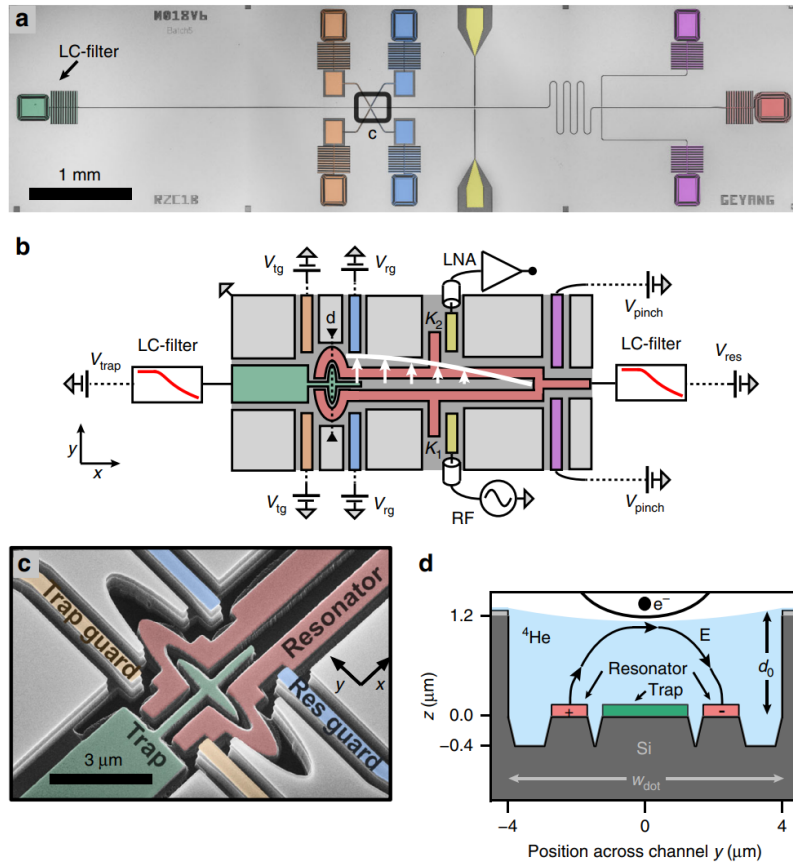
Figure 1.11: On-chip circuit QED implementation with a single electron trap
(a) Optical micrograph, (b) schematic of the device and (c) false-colored SEM picture.
(d) Schematic cross-sectional view of the electron trap with MW field distribution. The
figure is taken from [7].

states and the decoherence time to be $T_1 = 15\,\mu s$ and $T_2 \gtrsim 200$ ns, respectively. The
circuit QED setup for these two experiments is shown in Fig. 1.11, where the electron
is trapped in the green shaded trap and coupled to the MW photon provided by the
superconducting quarter wave resonator (red shaded area).

1.8.2   Spin qubits

In addition to the motional degrees of freedom, the electron carries a spin degree of
freedom. Spin coherence is generally limited by the interaction with nuclear spins in the
substrate material. Since the total nuclear spin of the ^{4}He atom is zero, the decoherence
rate of SSE on liquid ^{4}He is many orders of magnitude smaller than in most traditional

semiconductor 2DEG systems and is expected to exceed seconds [5]. The first proposal for spin-based qubits using electrons on helium was given by Lyon [3]. In this work, it was proposed to readout the individual electron spins by comparing the unknown spin with a known one, as was demonstrated in a double quantum well [71]. When two electrons are confined in a small volume, their wave function can overlap, and the exchange interaction leads to a singlet-triplet splitting, which allows a complete spin measurement. However, owing to the strong Coulomb repulsion between SSE on liquid helium, the average distance between electrons is too large to have the exchange interaction between them. Therefore, the above method is not applicable.
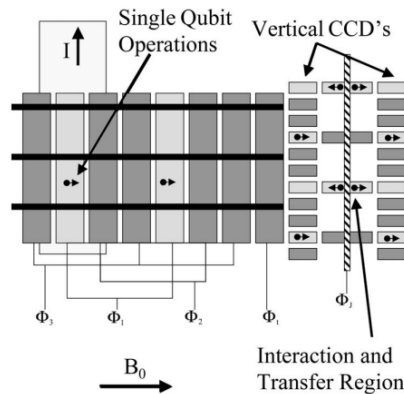
Figure 1.12: A schematic diagram of a possible gate electrode arrangement for a quantum computer. The light and dark gray regions are conducting gates held at different potentials arranged as a three phase CCD, as described in the text. The figure is taken from [3].

In addition to the readout, a charge-coupled device (CCD) configuration was also proposed in Ref. [3] to accomplish fast transport of electrons between the interaction and storage regions. As shown schematically in Fig. 1.12, the light and dark gray areas are the pixel gates that are arranged like those of a conventional three-phase CCD, and electrons can be rapidly transferred between these gates. The black horizontal lines are negatively biased to avoid cross-talk between horizontal channels. It is clear that a highly parallel and scalable architecture for a many-qubit system is possible with this configuration.

Spin-orbit coupling

In addition to the direct singlet-triplet splitting proposed by Lyon, the spin state readout can also be mediated by the orbital states. Schuster *et al.* suggested that the coupling between spin states and orbital states allows manipulation and readout of the individual spins [5]. As shown in Fig. 1.13(b), a spin-quantization axis is established using a magnetic field along the x-axis. In the presence of a nonuniform magnetic field B_z, the in-plane motional state is coupled to the spin state by a magnetic field gradient along x-axis ($\partial B_z/\partial x$), and the coupling Hamiltonian is given by $H_s = -2\mu_B s_z x \partial B_z/\partial x$, where μ_B represents the Bohr magneton. This spin-orbit interaction can significantly enhance the coupling between the MW photons and spins, whereas the bare coupling of MW photons to the electron spin is very weak.
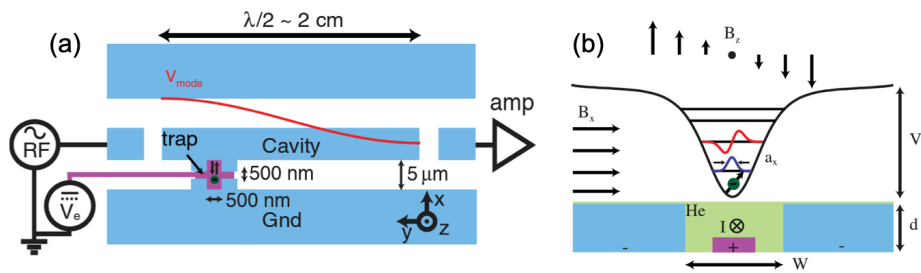
Figure 1.13: Circuit QED architecture with single electron trap for spin qubit (a) The top view of the transmission line resonator (blue areas) and the single electron trap (purple area). (b) Cross-sectional view of the electron trap with energy levels and wave functions of electron motional states. The figure is taken from [5].

Similarly, the spin state can also be coupled to the Rydberg states in a controllable way with the help of a magnetic field gradient along the vertical direction ($\partial B_z/\partial z$) [4]. As shown in Fig. 1.14, the transition of spin-up state from $|n = 1, \uparrow\rangle$ to $|n = 2, \uparrow\rangle$ can be excited by microwaves with frequency ω_+, meanwhile the transition of spin-down state from $|n = 1, \downarrow\rangle$ to $|n = 2, \downarrow\rangle$ corresponding to a different frequency ω_-. The separation of the Rydberg transition frequency between two spin states is proportional to the field gradient, with $\omega_- - \omega_+ = 2\mu_B[B_z(z_2) - B_z(z_1)]/\hbar \simeq \frac{2\mu_B}{h}\frac{\partial B_z}{\partial z}(z_2 - z_1)$. Thus, detection of

the excitation of the Rydberg state allows us to detect the spin state.
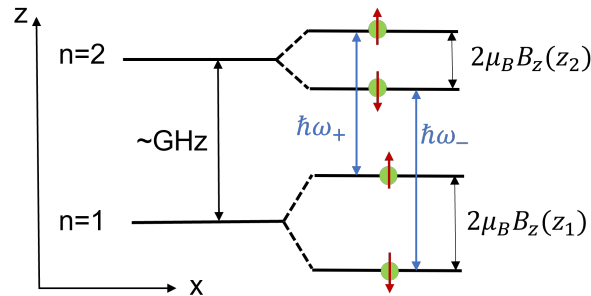
Figure 1.14: Energy spectrum of the spin-orbit coupled states of electrons bound to the surface of liquid helium.

In order to distinguish the spin state, the difference in Zeeman splitting must be larger than the transition linewidth (see Section 1.7). Thus, the magnetic field gradient must be sufficiently strong. Fig. 1.15 shows the distribution of the stray magnetic field across an electron trap calculated using COMSOL Multiphysics. Here, the central cylinder represents a 400-nm-long Cobalt micromagnet with radius $r = 50$ nm, which provides a stray magnetic field with the vertical component B_z and radial component B_r. Owing to the axial symmetry, we have $|B_x| = |B_y| = B_r$. The electrodes (blue shaded area) on both side of the micro-magnet provide the in-plane potential $\phi(x)$ for electron confinement. The average positions of the ground state and the first excited Rydberg state are indicated by red dots. Typically, the gradient of the magnetic field near the helium surface is $\partial B_z/\partial z \approx -0.43 \, \text{T}/\mu\text{m}$ and distance between the ground state and first excited Rydberg state is $\Delta z \approx 35$ nm. This provides the separation of the Rydberg transition frequency between spin-up and spin-down states around $(\omega_- - \omega_+)/2\pi = 300$ MHz, which is significantly larger than the intrinsic linewidth of the Rydberg states at low temperatures, see Fig. 1.10. These coupled spin-orbit states represent a potentially new way for probing the spin degree of freedom of electrons on liquid helium.

In summary, we have discussed various proposals for quantum information processing using both motional states and spin states of electrons bound to the surface of liquid helium. This PhD project is motivated by the possibility to realize the spin-orbit coupling
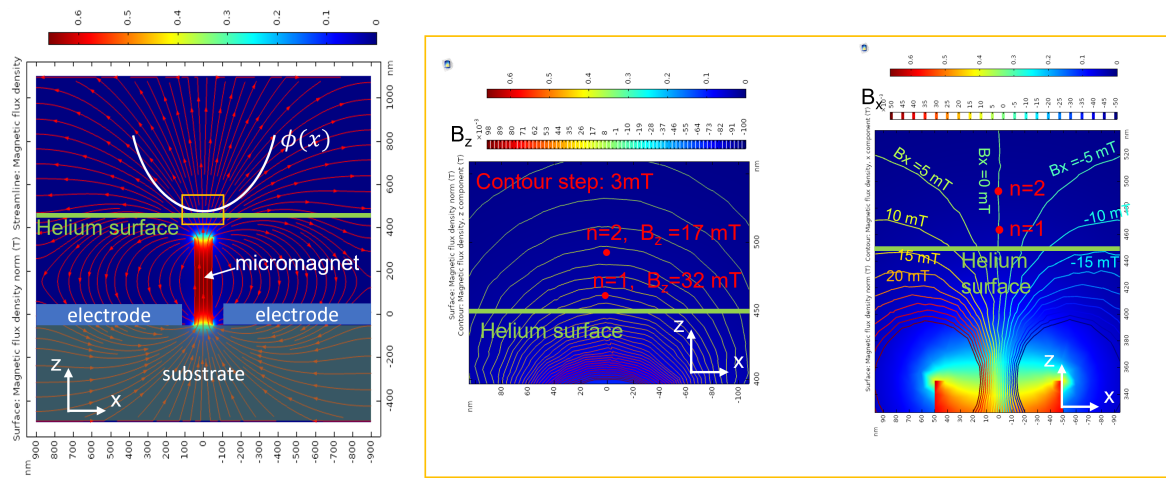
Figure 1.15: COMSOL simulation of the magnetic field distribution in a single electron trap. Left panel: Annotated cross-sectional view of a single electron trap with magnetic field distribution. Right panel: Zoomed-in images with the contour plots of the magnetic field distribution around the micromagnet, B_z (left) and B_x (right) components are shown. The average positions of the ground and first excited Rydberg states are denoted by red dots.

between the spin states of SSE and their Rydberg states. Starting from the next chapter, we discuss the realization of Rydberg state detection of SSE confined in a microchannel device, which might provide useful platform for such realization.

Chapter 2

Experimental methods

The implementation of electrons-on-helium experiments requires a careful design of the experimental setup. This chapter will describe the devices employed in our experiments, followed by an analysis of the electric field distribution in the devices and the resulting density distribution of electrons. This will be of a great importance for understanding the results of the transport measurements and Rydberg states detection presented in later chapters. In addition to the device geometry, the properties of the liquid helium substrate are also essential for operation of the devices. Therefore, we will discuss the properties of superfluid helium film and its effect on the electric field and electron density distribution in our devices.

This chapter is organized as follows: In Section 2.1, we introduce a capacitively coupled setup known as the *Sommer-Tanner method*. We discuss the underlying physics and the lumped circuit model for this method. In Section 2.2, we discuss two basic geometries of our experimental devices. Additionally, a basic procedure of the fabrication of the microchannel devices is presented. Analytical estimations of the density profile of SSE and holding electric field are given using a parallel-plate capacitor approximation which assumes a flat helium surface. This is followed by Section 2.3, where we discuss the properties of superfluid helium film. Finally, Section 2.4 provides description of the electrostatic simulations of the experimental device using the finite-element method (FEM),

and taking into account the properties of superfluid helium substrate.

2.1   The Sommer-Tanner (ST) methods

The *Sommer-Tanner detection method* has been wildly used for measuring the transport properties of electrons on liquid helium system since the early 1970s. This method was developed by W. Sommer and D. Tanner for the first electron mobility measurements [22]. The basic parallel configuration is shown schematically in Fig. 2.1. This method is based on the phase-sensitive detection of SSE capacitively coupled to the electrodes submerged under the liquid helium surface. Usually, the ST electrodes are surrounded by a guard ring electrode biased at ground or negative potential relative to other electrodes, which helps to confine the electrons in the measurement region. One of the ST electrodes (drive) is driven by an AC voltage with the amplitude of a few mV and frequency in the audio-frequency range (1-100 kHz). This leads to redistribution of SSE and creates a transport current. This current I is measured in a contactless way by detecting image current induced in the second ST electrode (sense) using a standard lock-in amplifier.
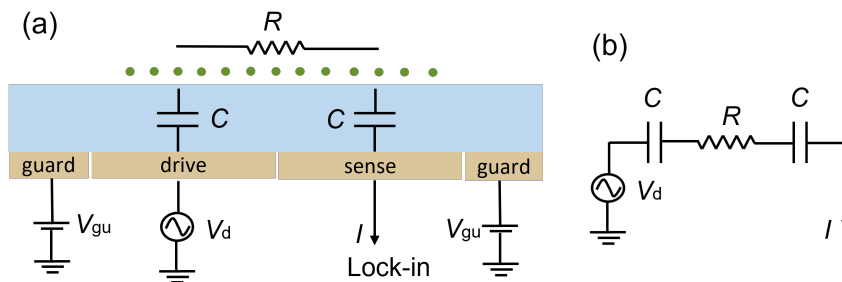
Figure 2.1: The Sommer-Tanner configuration. (a) SSE (green dots) capacitively-coupled to drive and sense electrodes modeled as a combination of two capacitors and a resistor connected in series. The capacitance is purely geometric and the resistor models the finite mobility of SSE, as described in the text. (b) The equivalent lumped element circuit of the setup in (a).

The equivalent lumped circuit model of this ST method is shown in Fig. 2.1(b). The capacitance C represents the coupling between SSE and ST electrodes, while the charged

surface resistance R mostly comes from the finite mobility of the SSE. According to this lumped circuit model, the total series impedance is given by $Z = R + \frac{2}{j\omega C}$. The response current I can be written as

$$I = \frac{V_{\mathrm{d}}}{Z} = \frac{V_{\mathrm{d}}}{R + 2/j\omega C} = \frac{R\omega^2 C^2 V_{\mathrm{d}}}{4 + R^2\omega^2 C^2} + j\frac{2\omega C V_{\mathrm{d}}}{4 + R^2\omega^2 C^2}, \tag{2.1}$$

where the first term corresponds to the in-phase component I_x of current with respect to the driving voltage V_{d} and the second term is the quadrature component I_y. In the limit of a perfect conductor, with $R = 0$, the coupling between two ST electrodes is purely capacitive and the current has a 90° phase delay relative to V_{d}. For finite resistance, the phase shift between I and V_{d} is given by $\tan\varphi = I_y/I_x = 2/\omega RC$. Accordingly, we obtain a semi-circle trajectory on the complex I_x vs. I_y plane by varying the resistance R form zero to infinity, see Fig. 2.2. The solid lines are obtained by varying R at different fixed values of $C = 0.4$, 1 and 1.6 pF, respectively.
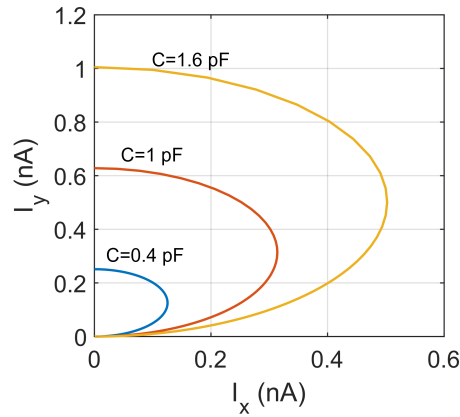
Figure 2.2: The trajectories of I in the complex plane. Here, we fixed $V_{\mathrm{d}} = 10\,\mathrm{mV}$ and $\omega/2\pi = 20\,\mathrm{kHz}$. Color lines: Varying R form zero to infinity, with $C = 0.4\,\mathrm{pF}$, 1 pF and 1.6 pF.

Eq. (2.1) provides the simplest version of the lumped circuit model. In practice, this model can be modified depending on the device geometry. In Section 3.2.1, we will revise this circuit model to take into account the geometry of our microchannel devices.

2.2 Device geometry and electrostatics

This section discusses two conventional setups to study the transport properties, as well as the Rydberg state transitions, namely, (1) the Corbino disk and (2) the microchannel device. It is instructive to describe the Corbino setup first because this geometry represents a simple parallel-plate capacitor.

2.2.1 Corbino disk device

The traditional Corbino disk device is formed by a set of concentric electrodes submerged under the liquid helium, see Fig. 2.3, which are used for the ST measurements. In practice, we apply driving voltage on the central electrode and detect the radial current of SSE at the outer ring, while the outermost electrode is negatively biased as a guard ring. This geometry has some advantages for the conductivity measurements in the presence of magnetic field applied perpendicular to the helium surface. In the conventional rectangular (Hall bar) geometry, the Hall effect produces a transverse electric field. While in the Corbino disk device, owing to the axial symmetry of a circular geometry, the transverse field is zero and the driving electric field has only the radial component E_r, which relates to the measured radial current density j_r, with $j_r = \sigma_{xx} E_r$, where σ_{xx} is the diagonal conductivity.

For the purpose of the Rydberg states detection, another set of electrodes with the same configuration is placed symmetrically on the top forming a parallel-plate capacitor with the bottom structure, see Fig. 2.3. The liquid level is placed between the top and bottom electrodes approximately parallel to the capacitor plates. The separation D between the top and bottom plates is chosen no less than 2 mm in order to avoid the capillary filling of the whole space between the plates by the liquid helium.

In what follows, we will ignore the distortion of the electric field near the capacitor edges and define $E_\mathrm{b} = E_\perp + |E^\mathrm{sse}|$ and $E_\mathrm{t} = E_\perp - |E^\mathrm{sse}|$ to be the electric field below and above the liquid surface, respectively. Here $E_\perp$ is the electric field exerted on SSE and
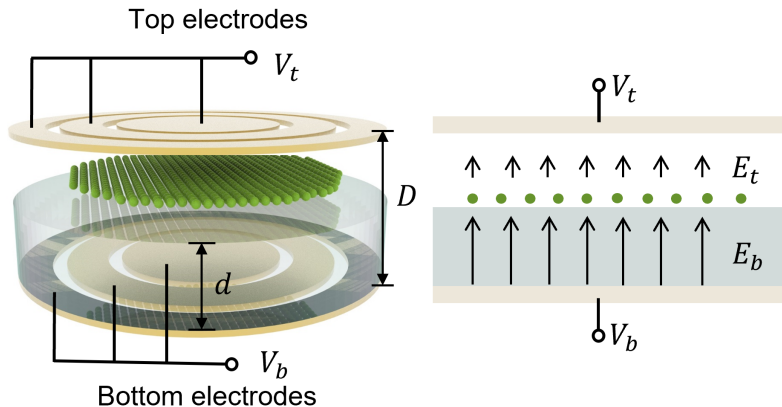
Figure 2.3: A schematic drawing of the Corbino disk device. The top and bottom electrodes are separated by a distance D, while d is the liquid level above the bottom plate. E_b and E_t represent the electric field below and above the charged layer, respectively.

$|E^\mathrm{sse}| = 2\pi e n_s$ is the electric field due to SSE. The voltages applied to the plates and the electric field between the plates are related by $V_\mathrm{b} - V_\mathrm{t} = E_\mathrm{b} d + E_\mathrm{t}(D - d)$, where d is the depth of the liquid helium, see Fig. 2.3. The holding electric field $E_\perp$ exerted on the SSE is therefore given by

$$E_\perp = \frac{E_\mathrm{b} + E_\mathrm{t}}{2} = \frac{V_\mathrm{b} - V_\mathrm{t}}{D} + 2\pi e n_s \frac{D - 2d}{D}. \tag{2.2}$$

Thus, the holding electric field $E_\perp$ is the sum of the external field $E_\perp^\mathrm{ext} = (V_\mathrm{b} - V_\mathrm{t})/D$ due to the applied voltages and the field $E_\perp^\mathrm{ima} = 2\pi e n_s(1 - 2d/D)$ due to the image charges induced on both capacitor plates by SSE. Note that when the parallel-plate capacitor is half-filled with helium ($d = D/2$), the amount of image changes induced in the top and bottom plates are equal, thus $E_\perp^\mathrm{ima} = 0$. In this case, the holding field becomes independent of the electron density and is completely determined by the applied voltages, that is $E_\perp = (V_\mathrm{b} - V_\mathrm{t})/D$. This is very convenient when performing experiments to observe the transition between the Rydberg states of SSE. In such experiments, the microwave frequency is usually fixed, while the transition frequency of the Rydberg states is tuned in

resonance by using the Stark shift of the Rydberg levels. Thus, in a half-filled setup the Stark shift is determined only by the applied voltages and independents of the electron density.

2.2.2 Microchannel device

The microchannel device offers a very high level of control of SSE, in particular their density and in-plane transport properties. The fabrication of such devices is compatible with modern lithography technologies and considerable efforts were made in developing such structured channel devices [8–10, 12, 69, 72–75].
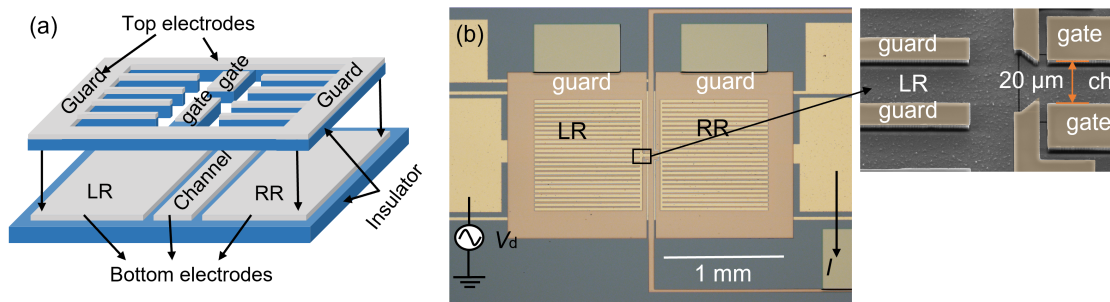
Figure 2.4: (a) Schematic drawing of the microchannel device used in our experiments. By applying proper biasing voltages to the top and bottom electrodes, the electrons are confined in a set of $4\,\mu$m-deep parallel troughs. (b) The annotated optical microscope and SEM images (inset) of the microchannel device. In the SEM image on the right, the top electrodes are shaded in the same dark orange color as they were in the optical microscope image, while the bottom electrode is kept in gray scale.

The optical microscope and the scanning electron microscope (SEM) images of the microchannel device employed in most of our experiments are shown in Fig. 2.4. Our typical device consists of two identical arrays of 20-μm wide and 700-μm long microchannels connected in parallel, which serve as the left and right electron reservoirs (LR and RR, respectively). The two reservoirs are connected by a single 20-μm wide and 100-μm long central channel. The whole structure is composed of two thin patterned gold layers separated by an insulating layer of hard-baked photoresist with a thickness of $d = 4\ \mu$m,

which defines the depth of the microchannels. The bottom gold layer (light orange in the optical microscope image) consists of three electrodes which define the bottoms of the two reservoirs and the central channel. These electrodes are separated by 1 μm wide gaps, as can be seen in the inset of Fig. 2.4 which shows the SEM image of a magnified portion at the central channel adjacent to the left reservoir. The corresponding electrical potentials applied to the bottom electrodes are denoted as V_{LR}, V_{RR} and V_{ch}. The top gold layer (dark orange in the optical microscope image) consists of two electrodes, the split-gate and guard electrodes. The split-gate electrode is aligned along the sides of the central channel. Together with the bottom electrode of the central channel it serves to control the density of SSE in the central channel by adjusting the electrostatic potential at the surface of liquid in the channel. Similarly, the guard electrode is aligned along the microchannels of each reservoir and serves to confine electrons inside the microchannels. The corresponding electrical potentials applied to the electrodes of the top gold layer are denoted as V_{ga} and V_{gu}.

Charging of device with electrons

The fabricated device is mounted on a printed circuit board (PCB) placed inside a leak-tight copper cell (see Fig. 2.5) and then cooled down to 150 mK at the mixing chamber of a dilution refrigerator. Liquid helium-4 is condensed into the sample cell and fills microchannels by the capillary action. After all channels are adequately filled with liquid helium, we apply a positive bias voltage $V_{LR/RR} > 0$ to the bottom reservoir electrodes, while the guard electrode is kept at the potential of the grounded sample cell, that is $V_{gu} = 0$.

Free electrons are produced inside the cell by the thermal emission from a tungsten filament and charge the surface of liquid filling the microchannels. Here, we can apply the same analysis as for the parallel-plate capacitor model shown in Section 2.2.1. For notation consistency, we will keep V_b and V_t notations for the bottom reservoir $V_{LR/RR}$ and top guard V_{gu}, respectively. One naturally expects that the SSE attain the maximum
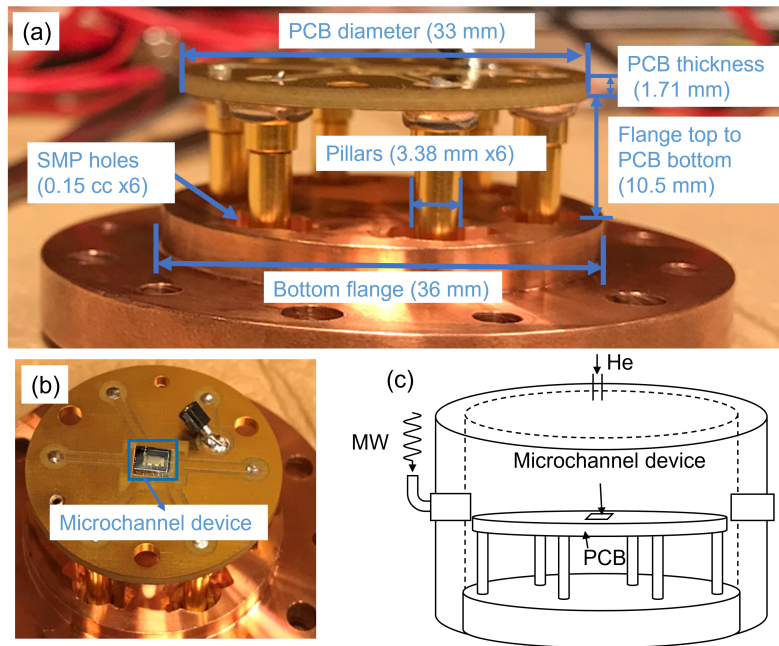
Figure 2.5: (a) Side view of the sample cell, with the dimensions of each components. (b) Top view of the microchannel device mounted on the PCB. (c) Schematic drawing of the sample cell.

density n_s^{sat} when the potential of charged surface V_e equals to that of the top electrodes, that is $V_e = V_t = 0$. The vertical electric field below and above the helium surface is therefore given by $E_b = V_b/d = 4\pi e n_s^{\text{sat}}$ and $E_t = 0$, respectively. In practice, the experimentally measured SSE potential V_e always shows a positive offset from zero, which reveals that the vertical component of the electric field above the liquid surface is not fully screened by SSE and the effective width of the electron layer W_{eff} is always smaller than the channel width W, see Fig. 2.6. In addition, we note that the potential of the charged surface V_e can vary for different experiments even though the electrode voltages are fixed.

After the reservoirs are charged with SSE, the electrons can be introduced into the central channel connecting the two reservoirs by varying the voltages applied to the channel and gate electrodes. When the potential at the uncharged liquid surface in the central channel equals to V_e, electrons start to fill the surface of liquid in the central channel. We can find the relation between the uncharged surface potential V_u, the top gate voltage V_{ga}
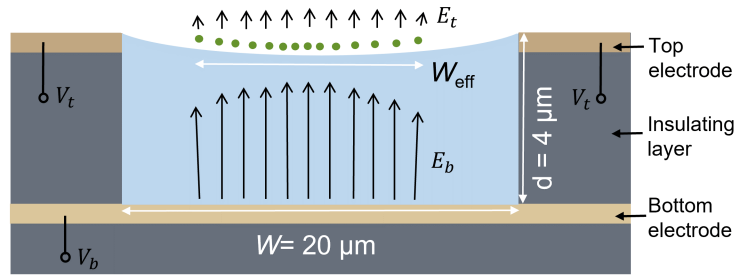
Figure 2.6: A schematic drawing of the microchannel device filled with SSE, as described in the text.

and the bottom channel voltage V_{ch} from a general capacitance model, see Fig. 2.7(a). By the general definition, the capacitance of a conductor is equal to $C = q/\Delta V$, there ΔV is the change of the electrical potential of the conductor when a charge q is brought to it from infinity. Thus, we have

$$C_{ga}(V_u - V_{ga}) = +q, \quad \text{and}, \quad C_{ch}(V_u - V_{ch}) = -q,$$
$$\Rightarrow V_u = \frac{C_{ch}}{C_{tot}}V_{ch} + \frac{C_{ga}}{C_{tot}}V_{ga} \equiv c_1 V_{ch} + c_2 V_{ga}. \tag{2.3}$$

Here, we define $C_{tot} = C_{ch} + C_{ga}$, $c_1 = C_{ch}/C_{tot}$ and $c_2 = C_{ga}/C_{tot}$. Thus, we have $c_1 + c_2 = 1$. When the surface is charged by electrons with the total charge Q and the SSE potential is fixed at V_e, by the definition of capacitance we have $|Q| = e n_s S = C_{tot}(V_u - V_e)$, where S is the surface area of central channel (see Fig. 2.7(b)). Note that the total number of positive image charges q' and q'' induced in the bottom and top electrodes should be equal to the total charge of electrons, that is $|q' + q''| = |Q|$. If we assume that the C_{ch} is given by the parallel-plate capacitance model, that is $C_{ch} = S/4\pi d$, it is straightforward to obtain the electron density in the center channel

$$n_s = \frac{1}{4\pi e c_1 d}(c_1 V_{ch} + c_2 V_{ga} - V_e). \tag{2.4}$$

Note that for $V_{ga} = V_e = 0$ this expression recovers the previously considered case of the saturated electron density, $n_s = n_s^{sat}$.
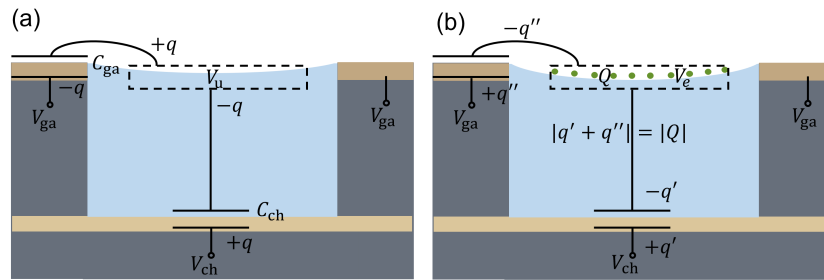
Figure 2.7: General capacitance model of the microchannel device without (a) and with a charged layer (b), as described in the text.

In order to establish an approximate relationship between the pressing (holding) electric field $E_\perp$ acting on SSE and the applied biasing voltages, we apply the simple relation $E_b = E_\perp + |E^{sse}|$ and assume a uniform electron density distribution, with $|E^{sse}| = 2\pi e n_s$. Similar to the parallel-plate capacitor setup considered in Section 2.2.1, we have $E_\perp = (V_{ch} - V_e)/d - 2\pi e n_s$. Using Eq. (2.4), we obtain an approximate analytical relation between $E_\perp$ and applied voltages

$$E_\perp = \frac{V_{ch}}{2d} - \frac{V_e}{d}\left(1 - \frac{1}{2c_1}\right) - \frac{c_2}{2c_1 d}V_{ga}. \tag{2.5}$$

Note that the parallel-plate capacitance approximation used above does not allow us to work out the actual distribution of the electrical potential and the electron density across the channel. The electrical potential distribution below and above the helium surface can be found numerically by the finite element modeling (FEM) using COMSOL Multiphysics, see Section 2.4 for details.

2.3 Properties of superfluid helium film

The physics of superfluid helium is of great importance for understanding the system's stability and its electrostatic properties. Therefore, this section provides a brief review of some relevant properties of the superfluid helium. Starting with a discussion of the thin film dynamics, the profile of the helium film formed in the microchannels are discussed in

Section 2.3.1. This is particularly important for the Rydberg states detection presented in later chapters. In Section 2.3.2, the occurrence of the hydrodynamical instabilities is discussed, as well as a number of methods which have been developed to partially suppress this instability.

2.3.1   Film profile

It is well-known that the ^{4}He liquid undergoes a phase transition to the superfluid state at the critical temperature $T_\lambda \simeq 2.18$ K. In our experiments, the bulk superfluid ^{4}He is condensed into the cell and the liquid surface level is placed slightly below the surface of PCB. Owing to its superfluity, the liquid climbs the pillars and covers the PCB with a thin film due to the Van der Waals attraction between helium atoms and the solid substrate, which balances the gravitational force. The coating film thickness h_0 at height h above the bulk level can be estimated from an expression for the chemical potential of the thin film μ_f [76]

$$\mu_f = \mu_0 + \rho g h - \frac{\alpha_v}{h_0^3}, \tag{2.6}$$

where μ_0 is the chemical potential of the bulk helium, $\rho g h$ is the gravitational energy ($\rho = 0.145\,\text{g/cm}^3$ is the mass density of liquid helium), and the third term comes from the van der Waals interaction, with α_v being the van der Waals constant of the substrate. In thermal equilibrium we have $\mu_f = \mu_0$, therefore the film thickness is given by $h_0 = (\alpha_v/\rho g h)^{1/3}$. For example, for a superfluid film on a silicon substrate at $h = 10$ mm we obtain $h_0 = 30$ nm [77].

In the case of superfluid helium filling the microchannels, the liquid depth does not follow the above expression for h_0. Instead, the channels are filled by liquid owing to the capillary force, provided that the capillary curvature radius is larger than channel width W. In the absence of the SSE, the capillary radius R_c is determined by surface tension and gravity, which is analogous to the rising of liquid in a capillary tube (Jurin's law), with $R_c(h) = \alpha/\rho g h$, where $\alpha = 0.378\,\text{erg/cm}^2$ is the surface tension of the superfluid helium

at the interface with vacuum. The schematic picture in the left panel of Fig. 2.8 shows the typical device geometry used in our experiments. Here, the depression of liquid surface d_0 is the distance between the lowest point of the deformed surface and the surface of the thin film above the guard (with the depth h_0) and is given by $d_0 = R_c - \sqrt{R_c^2 - (W/2)^2}$. The calculated capillary radius of curvature and the liquid surface depression for this device geometry are given in the right panel of Fig. 2.8.
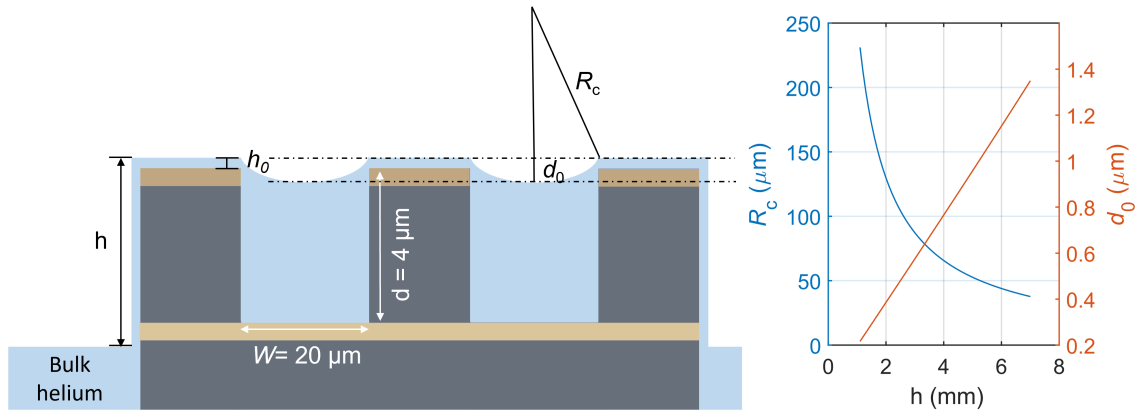
Figure 2.8: Left panel: Profile of the helium film in the microchannel device for uncharged surface of liquid. Right panel: Capillary radius of curvature R_c as a function of the bulk helium level relative to the device surface (blue line). R_c diverges as the bulk helium level fills up. Surface depression d_0 at the center of the channel versus bulk helium level is given by the orange line.

For a surface of liquid charged with SSE at density n_s, an additional term due to the electrostatic force is introduced into the curvature radius, according to

$$R_c(h) = \frac{\alpha}{\rho g h + e n_s E_\perp},\tag{2.7}$$

where the second term in the denominator represents the pressure due to the charge layer interacting with the holding filed $E_\perp$. For simplicity, let us consider a uniform saturated electron density n_s^{sat}, then $E_\perp = 2\pi e n_s^{\text{sat}}$. Typically in our experiments the saturated electron density is the order of 10^8 cm^2 and the bulk liquid level h is up to a few millimeters below PCB. The calculated radius of curvature R_c as a function of h for

different electron densities n_s^{sat} under the saturation condition is shown Fig. 2.9.
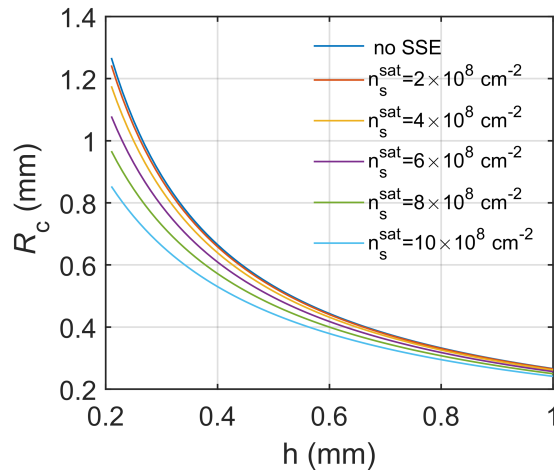
Figure 2.9: Capillary radius of curvature R_c as a function of the bulk helium level relative to the device surface h for saturated electron densities n_s^{sat}.

2.3.2 Hydrodynamical instability

In relation to our experiments, it is also instructive to discuss the stability of the charged liquid helium surface in the limit of high densities of SSE [28, 39, 40, 77, 78]. The high density limit is interesting in relation to a possibility to reach the regime of the degenerate 2DES on the surface of liquid helium, as was discussed in Section 1.3.1.

Now, let us consider a charged liquid film having the thickness d which is much greater than the inter-electron distance. In Section 1.4.1, we already discussed the hydrodynamical properties of the liquid helium without SSE and the dynamics of surface deformation ξ given by the Euler equation (1.26). When the surface of liquid helium is charged with SSE, there is an additional pressure $4\pi n_s^2 e^2 \nabla \xi$ added to the liquid surface, arising from the mutual repulsion between electrons. Accordingly, the Euler equation in the presence of SSE can be written as $\rho \frac{d\mathbf{v}}{dt} = -\rho g \xi + \alpha \nabla^2 \xi - 4\pi n_s^2 e^2 \nabla \xi$. Similarly to Section 1.4.1, taking the time derivative of the Euler equation and replacing the time derivative of ξ

with $\partial\Phi/\partial z$, we obtain

$$\rho g\frac{\partial\Phi}{\partial z} + \rho\frac{\partial^2\Phi}{\partial t^2} + 4\pi n_s^2 e^2\nabla\left(\frac{\partial\Phi}{\partial z}\right) - \alpha\nabla^2\left(\frac{\partial\Phi}{\partial z}\right) = 0, \qquad (2.8)$$

and using the same trial solution $\Phi \sim \mathrm{e}^{-i\Omega t}\mathrm{e}^{qz}f(\mathbf{r})$, we obtain $\Omega^2 = gq + \alpha q^3/\rho - 4\pi n_s^2 e^2 q^2$.

The condition for the surface to be stable is given by $\Omega^2 > 0$, which has to be valid for any value of q. This is equivalent to the condition $(2\pi n_s^2 e^2)^2 - \rho g\alpha \le 0$ which gives a critical density $n_s^{\max} = (\rho g\alpha)^{1/4}/(2\pi e^2)^{1/2} = 2.25 \times 10^9\,\mathrm{cm}^{-2}$ for liquid ^{4}He below 1.4 K. This expression is in good agreement with the experimental results on bulk helium [79]. Note that the predicted quantum melting and the formation of degenerate Fermi liquid happens at the electron density ranging from 10^{12} to $10^{13}\,\mathrm{cm}^{-2}$. Therefore, the regime of degenerate Fermi liquid can not be reached with SSE on the bulk liquid helium.

The simplest way to enhance stability is to decrease the film thickness. For a sufficiently thin film, there is a strong contribution from the van der Waals interaction between the thin film and substrate. The corresponding pressure term is given by $(3\alpha_v/d^4)\xi$, which varies as the inverse fourth power of the film thickness. Thus the conditions for a stable surface becomes $(2\pi n_s^2 e^2)^2 - 3\alpha_v/d^4 \le 0$. This significantly increases the stability of the charged film. However, the experimentally measured maximum charge density was distinctly larger than the anticipated value [77]. This is due to the additional pressure on the film, where the surface charge significantly modifies the film thickness according to $h_0' = h_0(1 + \frac{en_s E_\perp}{\rho g h})^{-1/3}$. Eventually, SSE tunnel into the solid substrate through the helium thin films, which prevents to reach the divergence regime.

Another method to suppress the instability is to utilize a fractionated geometry as was suggested by William [80], for example, using a microchannel device. The channel confinement introduces a low cutoff of the allowed wave vectors of the capillary waves with a minimum value of $q^{\min} = \pi/W$. For a 10 μm-wide channel, the hydrodynamic instability will occur at a critical electron density $n_s = 2.1 \times 10^{10}\,\mathrm{cm}^{-2}$, which is significantly larger than the critical density on the bulk liquid. The advantage of this method is that the

electron mobility remains relatively high, while it is significantly decreased for SSE on thin helium films due to the solid substrate roughness.

Finally, to achieve higher electron density, solid Hydrogen and solid Neon have also been considered as a substrate for SSE. To achieve high electron density, the solid-state substrates have been investigated by several groups and the electron density up to 10^{12} cm^{-2} had been reported [81–85].

2.4 Electrostatic simulations

In the previous section, we provided a simple estimation of the electron density using the parallel-plate capacitance approximation, see Eq. (2.4). However, for the detection of the Rydberg states of SSE in a microchannel device it is important to precisely determine the holding electric field $E_\perp$ acting on SSE, as well as the electron density distribution in the channel. This can be done by a numerical solution of the Poisson equation using FEM. This section presents some results of such numerical solutions obtained using the COMSOL multiphysics software.

Below, we present such solutions for two cases. The first case is that of a flat surface of liquid in the channel, where we ignore the surface curvature due to the surface tension. The second case extends the numerical solution to a curved surface.

2.4.1 Flat helium surface

If the bulk helium level is sufficiently high, corresponding to a large capillary radius, one could use the flat surface approximation. We start from the electrical potential profile across the microchannel device without a charged layer. A cross-sectional view of the channel geometry is presented in Fig. 2.10(a). The black lines outline the channel edge and the liquid level. The bottom electrode (bold orange lines) extends over the x-axis. Two $10\,\mu$m-wide and $4\,\mu$m-high insulating channel walls (with the dielectric constant $\epsilon_r = 7.5$) are placed symmetrically about $x = 0$, while the space between channel walls is

assumed to be filled with superfluid helium. The helium level coincides with the channel height and the helium surface is assumed to be flat. Two top electrodes (bold orange lines) are placed on top of the channel walls. The space above the helium surface is vacuum.
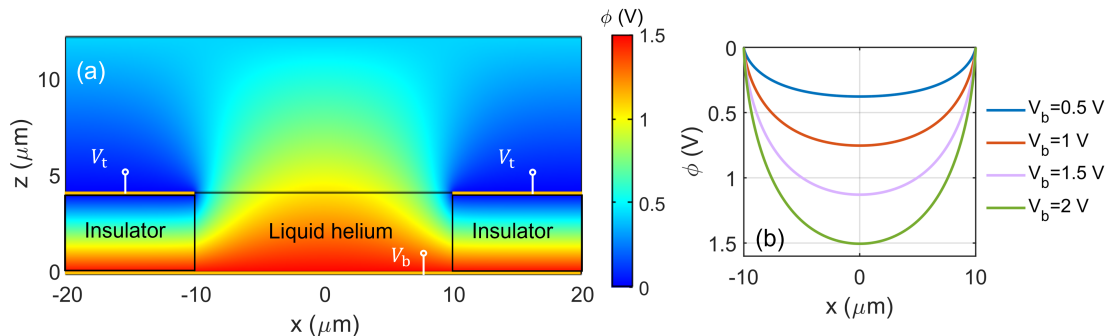
Figure 2.10: (a) Cross-sectional potential profile. The black lines outline the edges of the device. The helium level is located at $z = 4\,\mu$m. Bold orange lines represents the top and bottom electrodes. (b) Potential profile along the helium surface for different bottom biasing voltage V_{b}, with V_{t} set to 0. Assuming the lowest point of the potential profile $\phi(x = 0)$ is equal to V_u, one gets $c_1 \simeq 0.75$ and $c_2 \simeq 0.25$ from equation $V_u = c_1 V_{\mathrm{b}} + c_2 V_{\mathrm{t}}$.

Potential profile without SSE

First, we check the potential profile without electrons. We assume that the bottom electrode is at the potential $V_{\mathrm{b}} > 0$, while the top electrodes are grounded ($V_{\mathrm{t}} = 0$). The potential of the top boundary of the computation box was set to be floating, corresponding to a big distance between the device and top cell walls. The resulting potential distribution across the device and along the helium surface is presented in Fig. 2.10(a) and (b), respectively. It is clear that the applied voltages V_{b} and V_{t} provide a trapping potential for electrons at the surface. The trapping potential profile strongly depends on the applied voltages and channel dimensions. According to the potential profile $\phi(x)$ one expects that the electron density n_s is maximum at the center of the channel ($x = 0$) and decreases towards the channel edges. As discussed in Section 2.2.2, the potential of the uncharged liquid surface can be estimated using the parallel-plate capacitor approximation by the weighted-average of the top and bottom voltages $V_u = c_1 V_{\mathrm{b}} + c_2 V_{\mathrm{t}}$, where $c_1 + c_2 = 1$.

In our numerical simulations, the effective capacitive coupling between the SSE and the electrodes mainly comes from the electrons located near the channel center. Estimating V_u as the value of $\phi(x)$ at $x = 0$ we can obtain $c_1 \simeq 0.75$ and $c_2 \simeq 0.25$. In chapter 3, we will compare these values with our experimentally obtained values for c_1 and c_2.

Potential profile in the presence of SSE

In the presence of a charged layer on the helium surface, the potential profile across the device changes. A layer of free electrons forms an equipotential surface with a fixed potential V_e and an effective width W_{eff} across the channel. The width of the charged layer can be determined from the condition that the electric field along the charged layer vanishes, that is $\partial\phi/\partial x|_{W_{\mathrm{eff}}} = 0$. The dependence of the effective channel width W_{eff} on the external bias V_b applied to the bottom electrode is shown in Fig. 2.11(a). Fig. 2.11(b)
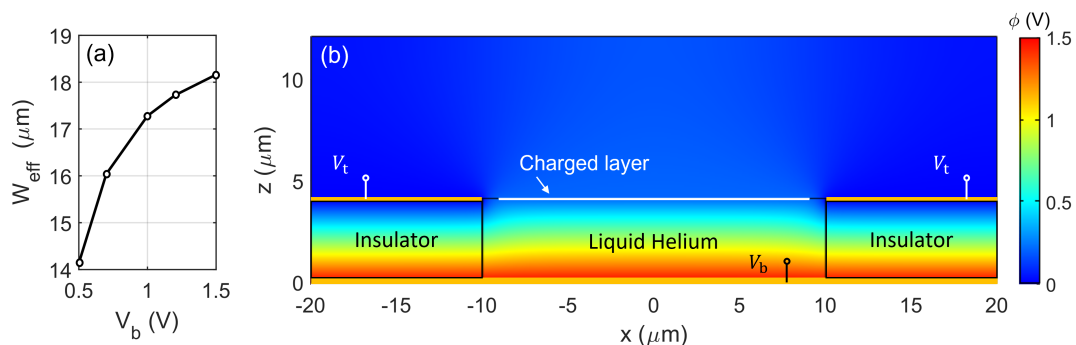
Figure 2.11: (a) The effective width of a charged layer versus the voltage applied to the bottom electrode V_b, while V_t is kept at 0 V. (b) Cross-sectional potential profile with a charged layer (white line) at the SSE potential $V_e = 0.2$ V. The bias voltage at top and bottom electrodes are $V_t = 0$ V and $V_b = 1.5$ V, respectively. The width of the charged layer $W_{\mathrm{eff}} = 18.6\,\mu$m is found from the boundary condition $\partial\phi/\partial x|_{W_{\mathrm{eff}}} = 0$.

presents the potential profile across the channel in the presence of a charged layer with effective width $W_{\mathrm{eff}} = 18.6\,\mu$m. The charged layer is represented by the white line in Fig. 2.11(b). Here, the SSE potential of the charged layer V_e is set to be 0.2 V, which is one of the typical value we have in our experiments. In this case, the electric filed above the helium surface is significantly screened by the SSE, that is $\partial\phi/\partial z|_{z>4\,\mu\mathrm{m}} \approx 0$.

The numerical solution for the electron density and holding field distribution is obtained from the boundary condition for the vertical electric field at the charged layer, according to

$$\left.\frac{\partial\phi(x)}{\partial z}\right|_{\text{above}} - \left.\frac{\partial\phi(x)}{\partial z}\right|_{\text{below}} = -4\pi e n_s(x) \quad \text{and} \tag{2.9}$$

$$\frac{1}{2}\left(\left.\frac{\partial\phi(x)}{\partial z}\right|_{\text{above}} + \left.\frac{\partial\phi(x)}{\partial z}\right|_{\text{below}}\right) = E_\perp(x). \tag{2.10}$$

The corresponding density profile and holding field distribution are shown in Fig. 2.12(a) and (b), respectively. The dashed lines show the results of the analytical approach given by Eq. (2.4) and (2.5).
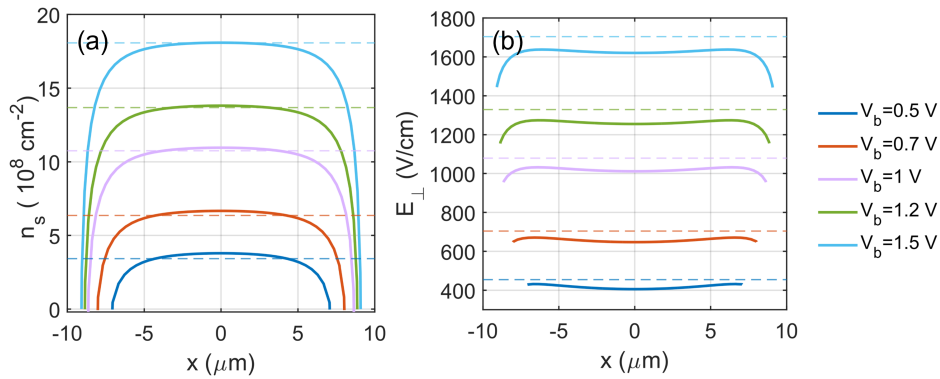
Figure 2.12: Cross-sectional profile of electron density (a) and holding field (b) obtained numerically assuming the flat helium surface for different values of V_{b}. In calculations, we assume $V_e = 0.2$ V and $V_{\text{t}} = 0$ V. The dashed lines are the analytical results obtained from Eq. (2.4) and (2.5).

2.4.2 Curved helium surface

This section investigates the effect of a curved helium surface on the results of our numerical simulations. As before, we represent the charged layer on a curved surface as an equipotential surface (at potential V_e) described by the parametrized coordinates $(x, z) = (s, -\Delta z(s))$, where the parameter $s \in [-W_{\text{eff}}/2, W_{\text{eff}}/2]$, $z = d_0 - (R_c - \sqrt{R_c^2 - s^2})$, and d_0 is the level of depression introduced in Section 2.3.2. As before, the width of the

charged layer W_{eff} is determined by the condition of zero electric field tangential to the charged liquid surface. The boundary condition for the electric field perpendicular to the charged surface are now rewritten as

$$\left(\nabla_{\vec{n}}\phi(x,z)\big|_{\text{above}} - \nabla_{\vec{n}}\phi(x,z)\big|_{\text{below}}\right) = -4\pi e n_s(x,z) \quad \text{and} \tag{2.11}$$

$$\frac{1}{2}\left(\nabla_{\vec{n}}\phi(x,z)\big|_{\text{above}} + \nabla_{\vec{n}}\phi(x,z)\big|_{\text{below}}\right) = E_{\perp}(x,z), \tag{2.12}$$

where $\vec{n}$ is normal to the surface. The results of the calculations using COMSOL for the electron density (a) and holding field (b) for a curved surface with $R_c = 100\,\mu\text{m}$ are shown in Fig. 2.13. Comparison with the results shown in Fig. 2.12 for a flat surface shows that,
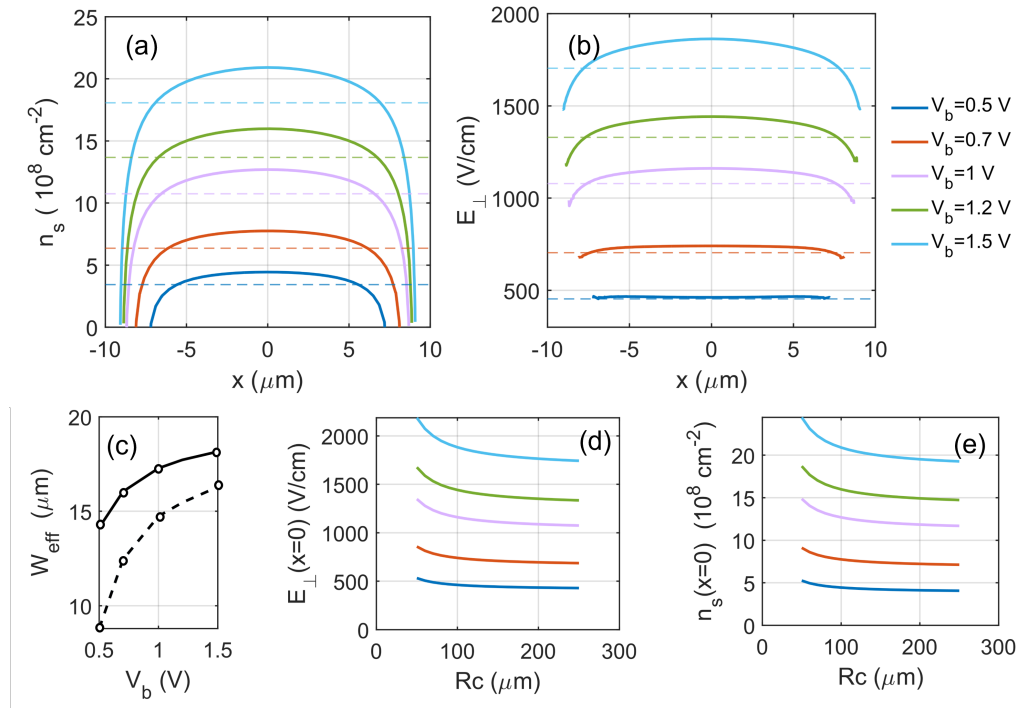
Figure 2.13: Cross-sectional profile of electron density (a) and holding field (b) for the curved helium surface, with $R_c = 100\,\mu\text{m}$ and different values of V_{b}. The other conditions are the same for Fig. 2.12. The dashed lines are the results obtained from the analytical approximation as was described for Fig. 2.12. (c) Effective width versus V_{b} under different R_c for a flat surface (solid line with open circles) and curved surface with $R_c = 100\,\mu\text{m}$ (dashed line with open circles). (d,e) The holding field (d) and electron density (e) versus the capillary radius curvature R_c for different values of V_{b}.

both n_s and $E_\perp$ are somewhat larger for a curved surface. This is because the helium level in the channel is depressed, which brings SSE closer to the bottom electrode. The smaller distance from the bottom electrode also modifies the potential profile provided by the electrodes, which in turn changes the effective channel width. Fig. 2.13(c) compares the effective width of charged layer for curved and flat surface profiles under different biasing. In addition, the calculated n_s and $E_\perp$ for different values of R_c are shown in Fig. 2.13(d) and (e). As expected, the density and holding field increases with decreasing R_c.

A direct comparison of the numerical results for n_s and $E_\perp$ with the experiment is complicated by the fact that the radius of curvature R_c of the liquid surface is expected to be different for different values of $V_{\rm b}$. Indeed, according to Eq. (2.7) the radius of curvature depends both on the bulk helium level with respect to the device (see Fig. 2.9) and the pressing field. Therefore, in a typical experiment where the liquid level is usually fixed, the radius of curvature will vary for different $V_{\rm b}$. To find the variation of R_c with $V_{\rm b}$ from our numerical calculations by taking into account Eq. (2.7), we performed the following procedure.

First, we assume a certain value of R_c for a particular value of $V_{\rm b}$ and calculate the bulk helium level $h^{(0)}$ from Eq. (2.7). Here, we take the values of n_s and $E_\perp$ at the center of the channel ($x = 0$) from our numerical calculations, see Fig. 2.13(a, b). With a fixed value of $h = h^{(0)}$ and using Eq. (2.7) we can recalculate the radius of curvature R_c' as a function of n_s, $E_\perp$, and therefore R_c, using the calculated dependence $n_s(R_c)$ and $E_\perp(R_c)$ for each given value of $V_{\rm b}$, see Fig. 2.13(d, e). The result is shown in Fig. 2.14. Intersection of this graph with $R_c' = R_c$ (black line) gives the curvature radius for a fixed value of $h = h^{(0)}$.

As an example, Table 2.1 shows the calculated values of R_c, $n_s(x = 0)$ and $E_\perp(x = 0)$ for several values of $V_{\rm b}$ used in the calculations presented in Fig. 2.13. Here, we assumed the radius of curvature $R_c = 100\,\mu$m at $V_{\rm b} = 0.5$ V, which corresponds to $h^{(0)} = 2.64$ mm. As expected, the radius of curvature significantly decreases with increasing n_s and $E_\perp$ due to the pressure exerted on the surface by the surface charge. Note that this limits
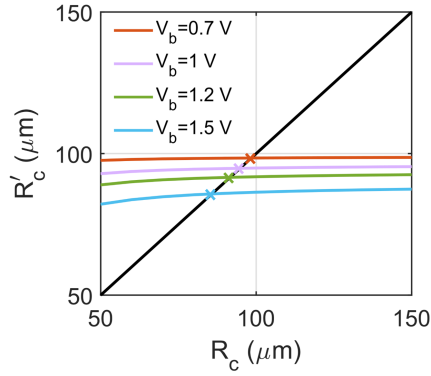
Figure 2.14: Black line: $R'_c = R_c$. Colored lines: Calculated R'_c at the middle of the channel using the data in Figure 2.13 (d,e), the crosses denotes the points $R'_c = R_c$, as described in the text.

the maximum density which can be accumulated in the surface of liquid in a channel. In particular, SSE will be lost when the corresponding depression of the surface will exceed the channel depth. This prevents to reach the quantum degeneracy regime discussed in Chapter 1.

V_{b} (V)	R_c (μm)	$n_s(x=0)$ (cm^{-2})	$E_\perp(x=0)$ (V/cm)
0.5	100	4.5×10^8	462.1
0.7	98.5	7.75×10^8	740.9
1.0	94.8	13.1×10^8	1178.7
1.2	91.6	16.8×10^8	1464.4
1.5	85.7	22.45×10^8	1930.2

Table 2.1: Calibrated surface curvature for a fixed bulk helium level $h = 2.64\,\mathrm{mm}$.

Chapter 3

Transport measurements of SSE on superfluid helium in the microchannel device

In Chapter 1, we reviewed the Boltzmann transport theory based on a microscopic model of the electron-ripplon interaction. It was shown that the electron mobility strongly depends on several external parameters, such as the temperature T, holding electric field $E_\perp$, and the external driving field V_d. In this chapter, we discuss the results of our transport measurements of SSE using a microchannel device similar to those described in Chapter 2. In particular, we will focus on the dependence of the transport behavior of SSE on the above mentioned parameters and make comparison with the experiments reported earlier.

This chapter is organized as follows. In Section 3.1, we give a brief overview of some early experimental achievements. From Section 3.2, we focus on our experiments using microchannel devices and discuss the dependence of the measured electron current on T, $E_\perp$ and V_d. In particular, in Section 3.3.2 we discuss the measured time-averaged I-V characteristics of SSE and show that they are similar to the transport behavior reported in some earlier experiments, where this behavior was attributed to the formation of an

exotic stripe phase of WS. Finally, in Section 3.4 we provide a correct explanation of the observed behavior based on the results of our time-resolved transport measurements.

3.1 Overview of the earlier transport experiments with SSE on helium

The first direct mobility measurements of electrons on helium have been reported in 1971 by Sommer and Tanner using a capacitively coupled method discussed in Chapter 2 [22]. Since then, the capacitively coupled method served as a main instrument for the transport measurement in a variety of electrons-on-helium experiments [33, 34, 86–88]. Using this method, Sommer and Tanner measured the dependency of the electron mobility on the ambient temperature. It was found that in the temperature range 0.8-1.5 K, the mobility increased with decreasing temperature. Theoretical calculations of the mobility of SSE were performed by Saitoh [46], who showed that the results obtained by Sommer and Tanner can be explained by the scattering of SSE from the vapor atoms, see Eq. (1.80). As the temperature decreases, the vapor density become extremely small and the primary scatters are ripplons. In the ripplon scattering regime, the mobility has weak temperature dependence and SSE have very high mobility approaching $\mu \sim 10^8$ cm^2/V·s. More accurate mobility measurements were performed by Mehrotra *et al.* [33], who showed that the measured mobility had a strong dependence on the holding electric field $E_\perp$, therefore the electron densities n_s, which is proportional to $E_\perp$. In the low density region, the measured mobility was found to be in good agreement with the theoretical calculations using the semi-classical treatment discussed in Section 1.5. For relatively high electron densities, the conventional semi-classical treatment was unable to completely account for the observed mobility. Moreover, at sufficiently low temperatures the mobility dropped due to the WSlization, as described in Section 1.6.

The earlier experiments discussed above were performed with SSE on the bulk helium using a set of macroscopic electrodes for capacitive coupling measurements. Since the

size of these devices is typically in a millimeter range, a precise control of SSE on a microscopic scale is rather difficult. With the development of the lithography techniques one can easily fabricate the electrode structures on a much smaller scale, which can provide a more precise control of SSE down to a few thousand of electrons, or even a single electron [89]. In addition to this, one can also achieve much higher electron densities in the micro-fabricated devices comparing to the bulk helium setups because the hydrodynamical instability of the liquid helium surface can be significantly suppressed by the confining geometry, as discussed in Section 2.3.2.

The microchannel device is a very convenient setup for the transport measurements in SSE on superfluid helium. Employment of such devices opened possibilities to observe some novel features associated with the transport and phase transitions in SSE at high densities. Examples include the structural transition of a quasi-1D electron crystal [13, 90], the damping effect of a finite-size WS [69], and the stick-slip motion of WS [10, 91, 92]. The first microchannel device has been reported by Glasson *et al.* in 2001 [8], the schematics of this device is shown in Fig. 3.1(a). In this device all reservoir channels were arranged perpendicular to the central channel. Note that there is another frequently used configuration, in which all channels are aligned in parallel. Such a parallel geometry is used in the experiment described in this thesis, see Fig. 2.4. The electrical properties of SSE measured by Glasson *et al.* in the microchannel setup (see Fig. 3.1(a)) are shown in Fig. 3.1(b, c). A lumped circuit analysis discussed in Section 3.2.1 was used to retrieve the resistance R and driving electric field E from the measured current of SSE. As shown in Fig. 3.1(b), a sharp increase of the resistance at temperatures below the melting temperature T_{m} signifies the Wigner crystallization. In Fig. 3.1(c), the measured field-velocity characteristics of WS are shown. The abrupt increase of the driving filed corresponds to the strong coupling between WS and DL due to the BC effect, as is expected from the Dykman-Rubo theory (see Section 1.6), while the subsequently driving field oscillations versus electron velocity v were attributed by Glasson *et al.* to a nonequilibrium transition of the SSE to a novel dynamically ordered phase of current filaments aligned along the

channels [8]. This unusual transport behavior will be the subject of our experimental work and is discussed in more details in Section 3.3 and 3.4.
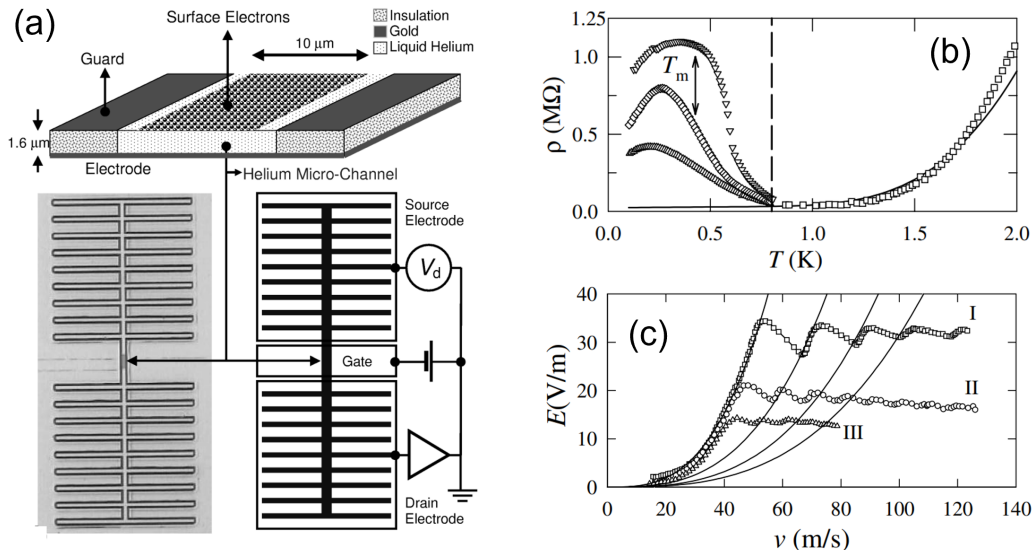
Figure 3.1: The first experiment using microchannel device. (a) A schematic view of the device. The channels have $1.5\,\mu$m in height and $10\,\mu$m in width. Here, the reservoir channels are arranged perpendicular to the central channel. (b) The electron resistance as a function of temperature for different electron densities. ($\square$) corresponds to the resistance at $n_s = 5.1 \times 10^8$ cm^{-2} and $T > 0.8$ K. The resistance below 0.8 K for 16 ($\triangle$), 31 ($\diamond$), and 64 ($\triangledown$) m/s, for $n_s = 3.5 \times 10^8$ cm^{-2} ($T_m = 0.42$ K). The solid line shows the theoretical calculation. (c) The force-velocity characteristics of the device for biasing voltages of 1.8 (data I), 1.2 (II), and 0.8 V (III). The figure is taken from Ref. [8].

3.2 Transport measurements of SSE confined in the microchannel device with the parallel channel configuration

Starting from this section, we present the results of our transport measurements with SSE confined in the microchannel device described in Chapter 2.

3.2.1 Equivalent circuit analysis of the microchannel device

First, we review the basic ST measurement and the equivalent circuit model in the parallel microchannel configuration. Similar analysis can also be applied to the perpendicular geometry used in the experiment by Glasson *et al.* [8]. As shown in Fig. 3.2(a), the majority of SSE are confined in two sets of parallel reservoir microchannels, and are capacitively coupled to both bottom reservoir electrodes and the top guard electrode, with the corresponding coupling capacitance denoted by C_1 and C_2, respectively. The charged surface resistance R_{ch} mostly comes from SSE in the central channel, because the surface area of the reservoirs is several orders of magnitude higher than that of the central channel. Accordingly, the equivalent lumped element circuit model is shown in Fig. 3.2(b).
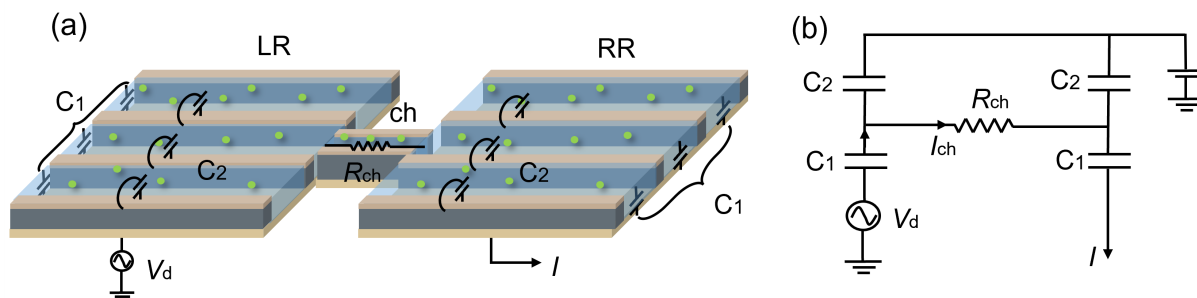
Figure 3.2: (a) A schematic drawing of the microchannel device. The coupling between the SSE and LR/RR electrodes are denoted by C_1, whereas C_2 represents the coupling to guard electrode. (b) The corresponding lumped circuit model.

Using the standard lumped-circuit analysis discussed in Section 2.1, the response current I can be rewritten as

$$I = I_{\mathrm{ch}} \frac{C_1}{C_0} = \frac{R_{\mathrm{ch}}\omega^2 C_1^2}{4 + R_{\mathrm{ch}}^2 \omega^2 C_0^2} V_{\mathrm{d}} + j \frac{2\omega C_1^2}{4C_0 + R_{\mathrm{ch}}^2 \omega^2 C_0^3} V_{\mathrm{d}}. \tag{3.1}$$

where, ω and V_{d} is the frequency and amplitude of the applied driving voltage, respectively. Here, we denote $C_0 = C_1 + C_2$, $C_1/C_0 = c_1$ and $C_2/C_0 = c_2$, see Fig. 2.7(b) and Eq. (2.3). Note that, for $c_2 \ll c_1$ this model recovers the simplest version given by Eq. (2.1). Accordingly, one can rewrite the R_{ch} in terms of the in-phase I_x and quadrature

components I_y of the measured current I, that is

$$R_{\text{ch}} = \frac{2I_x}{\omega C_0 I_y} \quad \text{with} \quad C_0 = \frac{2I_y^{\text{max}}}{c_1^2 \omega V_{\text{d}}}. \tag{3.2}$$

Here, I_y^{max} represents the maximum current obtained from Eq. (3.1), at $R_{\text{ch}} = 0$, which represents the pure capacitive coupling. On the other hand, we can express the driving electric field acting along the central channel as $E = R_{\text{ch}}I/L$, where $R_{\text{ch}}I$ is the voltage drop across the resistor R_{ch} and L is the length of the central channel. According to Eq. (3.2), it is clear that

$$E = \frac{R_{\text{ch}}I}{L} = \frac{c_1^2 V_{\text{d}}}{L} \frac{I_x I}{I_y I_y^{\text{max}}} = \frac{c_1^2 V_{\text{d}} \cos \theta}{L}, \tag{3.3}$$

where θ is the phase difference between the measured current I and driving voltage V_{d}.

3.2.2 Temperature dependence of the electron transport

Next, we discuss the temperature dependence of the measured transport current I. As discussed in Section 1.5, the resistivity of SSE in the central channel is inversely proportional to the electron mobility μ according to

$$R_{\text{ch}} = \frac{L}{W_{\text{eff}}} \frac{1}{e n_s \mu(T)}, \tag{3.4}$$

Thus, I_x and I_y, which depends parametrically on R_{ch}, can be varied in experiment by changing the temperature T. Two examples of the I_y versus I_x plots obtained by decreasing the temperature are shown in Fig. 3.3(a, b). The data were obtained using (a) $V_{\text{d}} = 5\,\text{mV}$, $\omega/2\pi = 99\,\text{kHz}$ and $V_{\text{ch}} = 0.5\,\text{V}$, (b) $V_{\text{d}} = 10\,\text{mV}$, $\omega/2\pi = 20\,\text{kHz}$ and $V_{\text{ch}} = 1\,\text{V}$. Note that all AC parameters are given in rms unit. The black dashed lines represent the fitting using Eq. (3.1), while the jet color dots represent the current components measured by a lock-in amplifier. In addition, the resistivity of SSE in the central channel and the electron mobility μ are extracted from the measured current I

according to the relation (3.2) and (3.4), and the corresponding plots for the current traces
given in Fig. 3.3(a) and (b) are shown in Fig. 3.4.

Note that with decreasing T electrons crystallize into the solid phase, which can result
in a rather complicated current response. An example is shown in Fig. 3.3(b), where the
current trajectory abruptly reverses direction (indicated by arrow) during the cooling of
the SSE at $T = 0.7$ K. From the COMSOL simulation, the electron density in the central
channel is estimated to be about 11×10^8 cm^{-2} giving the transition temperature about
0.7 K. It is clear that the abrupt change in current trajectory is due to the phase transition
of SSE to the crystalline phase. Similarly, an abrupt decrease of the electron mobility
is also observed in Fig. 3.4(d) at the transition temperature around 0.7 K. On the other
hand, in Fig. 3.3(a), the estimated electron density is 4×10^8 cm^{-2}, corresponding to the
transition temperature about $T = 0.4$ K. However, we cannot observe any striking change
in the current below 0.4 K.
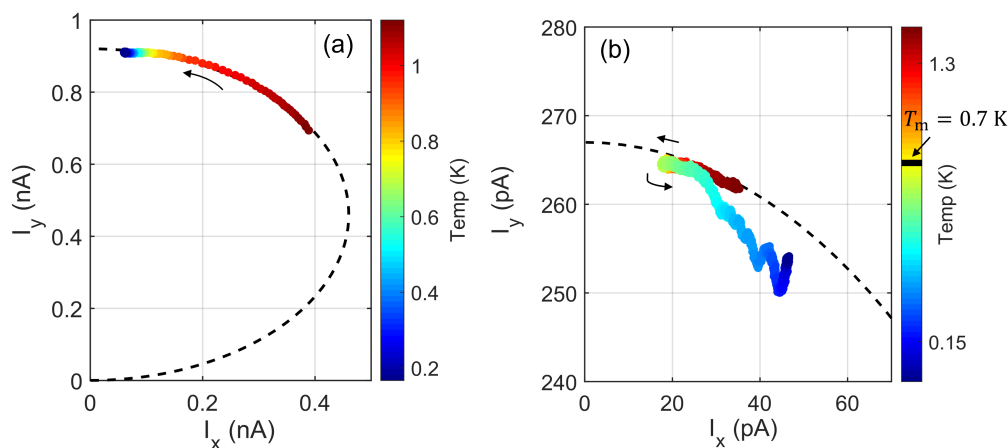
**Figure 3.3: The resistive component (I_x) and capacitive (I_y) components of
the measured current I obtained upon cooling SSE.** The data are obtained at
$V_d = 5$ mV, $\omega/2\pi = 99$ kHz and $V_{ch} = 0.5$ V for (a) and $V_d = 10$ mV, $\omega/2\pi = 20$ kHz
and $V_{ch} = 1$ V for (b). The arrows indicate the change of current components during the
cooling of SSE and the dashed line represents the fitting using the lumped-circuit model.

The difference between these two results comes from the nonlinear dynamics of WS
transport, which is sensitive to the external driving voltage. As it will be shown in
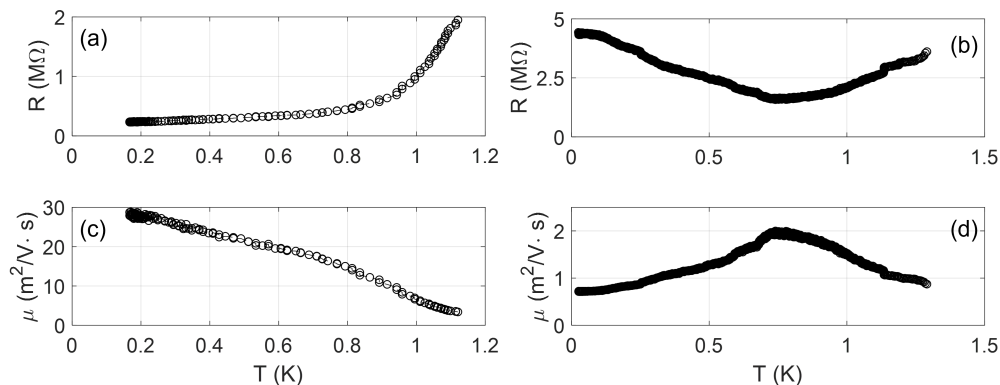
Figure 3.4: The resistance and the mobility extracted from the measured current I obtained upon cooling SSE. (a, b) The resistance extracted from the measured current I showed in Fig. 3.3(a) and (b), using the relation (3.2). (c, d) The corresponding electron mobility obtained from the resistance (a, b), using a simplified relation (3.4).

Fig. 3.6(a), we can separate the transport process of WS into three distinct regimes, that is, the linear regime, the BC plateau and the sliding regime. For the low channel voltage $V_{\text{ch}} = 0.5$ V in Fig. 3.3(a), which corresponds to the pressing electric field $E_{\perp} = 450$ V/cm, the transport of WS is in the linear regime. Accordingly, there is no significant difference in the transport of SSE in the liquid and solid phases, the mobility of such a system is then dominated by the ripplon scattering process. One can see in Fig. 3.4(c), the mobility extracted from the simple relation (3.4) shows similar trend with the theory, see Fig. 1.8. Note that in practice, our calculated mobility is several times lower than expected, this mismatch may due to the fact that the holding filed profile are not uniform across the channel, which leads to a change of electron mobility in different position of the channel. For this reason, the relation (3.4) used to extract the mobility is over simplified, nevertheless, it provide us a qualitatively estimation of the mobility within the same order of magnitude of the theory.

Contrarily, for high channel voltage $V_{\text{ch}} = 1$ V in Fig. 3.3(b), which corresponds to the pressing electric field $E_{\perp} = 1100$ V/cm, the transport of WS is strongly nonlinear, which leads to a significant difference in the electron transport for the liquid and solid

phases. In particular, in the BC scattering regime of the WS transport, the mobility of WS decrease with decreasing T because the damping of resonantly emitted ripplons comprising DL also decreases with T. As a result, WS is coupled more strongly to DL. This qualitatively explains the reversal of the current in the WS phase in Fig. 3.3(b) and the abrupt decrease of the mobility in Fig. 3.4(d).

3.2.3 Dependence of the transport of SSE in the central channel on the confining potential

In order to characterize the performance of the microchannel device, we typically measure the dependence of the transport current through the central channel on the applied voltages V_{ch} and V_{ga}, which determine the confinement of SSE in the central channel, thus affect the electron density n_s and effective width W_{eff} of the electron system. Fig. 3.5 shows the magnitude (a) and phase (b) of the current I measured for different values of V_{ch} and V_{ga} at $T = 150$ mK. The data were obtained using the amplitude of the driving voltage $V_d = 5$ mV and the driving frequency $\omega/2\pi = 20$ kHz. As discussed in Section 2.2.2, the surface area of the two reservoirs is thousand times larger than that of the center channel, thus one can assume that the potential of the charged surface V_e is fixed and our device acts essentially as a field-effect transistor, where conductance between the two reservoirs is controlled by n_s and W_{eff} of SSE in the central channel, see Eq. (3.4), therefore by the voltages V_{ch} and V_{ga}. The conductance threshold is determined by the condition $c_1 V_{ch} + c_2 V_{ga} = V_e$. Using this equation, it is straightforward to obtain $c_1 \simeq 0.8$, $c_2 \simeq 0.2$ and $V_e = 0.24$ V from the red line in Fig. 3.5(a). This result agrees well with the values $c_1 \simeq 0.75$ and $c_2 \simeq 0.25$ obtained from the COMSOL simulations. For an opened central channel ($\alpha V_{ch} + \beta V_{ga} > V_e$), the central channel resistance varies with both V_{ch} and V_{ga}. As an example, the magenta solid line in Fig. 3.5(a) shows the variation of the current measured for different values of V_{ch} at a fixed value of $V_{ga} = 0$. Above the conductance threshold, the current magnitude rapidly increases with increasing V_{ch} as electrons start
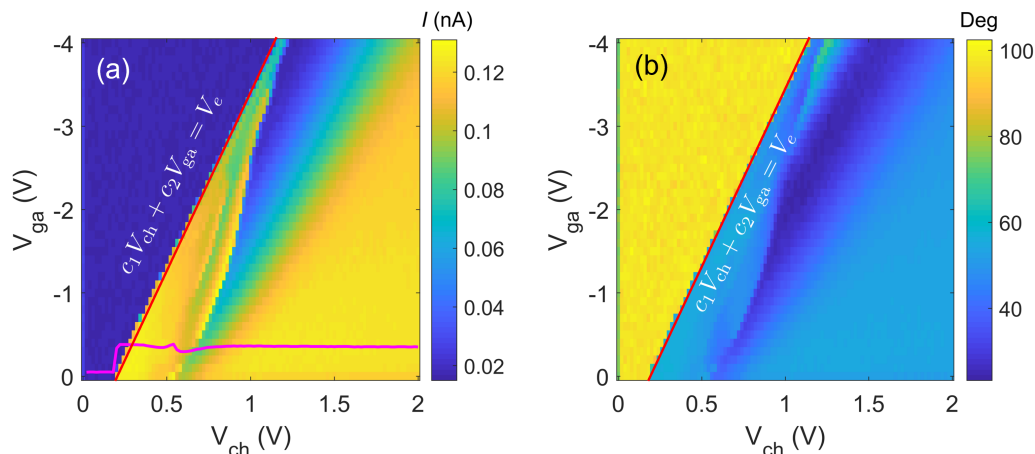
Figure 3.5: 2D scan of the current magnitude I (a) and phase (b) versus V_{ch} and V_{ga} Data were taken at $T = 150$ mK in a $4\,\mu$m deep and $20\,\mu$m wide channel device, with $V_d = 5\,$mV and $\omega/2\pi = 20\,$kHz. Magenta line: the variation of the current measured for different values of V_{ch} at a fixed value of $V_{ga} = 0$. Red line: conductance threshold determined by the condition $c_1 V_{ch} + c_2 V_{ga} = V_e$, one can get $c_1 \simeq 0.8$, $c_2 \simeq 0.2$ and $V_e = 0.24$ V.

filling the central channel. For higher values of $V_{ch} \gtrsim 0.5$ V, the current magnitude decreases due to formation of WS and its dynamical pinning to DL, as described in Section 1.6. However, in contrast to the conductance threshold, it is difficult to determine the phase boundary between electron liquid and WS precisely from such measurements. As will be shown in Section 3.4, the decoupling of WS from DL can occur at different times during the driving cycle, depending on a number of parameters including the bias voltages and driving voltage amplitude. This gives rise to the complicated current response to variations in V_{ch} and V_{ga} close to the phase boundary.

3.3 Unusual transport behavior of WS in response to the driving voltage V_d

This section provides a detailed discussion of the transport behavior of WS in the central channel in response to the driving voltage V_d. As discussed earlier, by varying the driving voltage amplitude V_d several nonlinear phenomena related to different dynamical regimes

of WS can be observed, such as the BC plateau and the sliding of WS. Moreover, an unusual transport behavior was observed in the earlier experiments by Glasson *et al.*, see Fig. 3.1, which was interpreted as a dynamical phase transition of WS into an exotic stripe phase. It will be shown that a similar phenomenon is observed in our experiments. Before presenting these experimental results, we first present the nonlinear *I-V* characteristics of WS measured using our microchannel devices with parallel channel configuration.

3.3.1   *I-V* characteristics of WS

One of the most remarkable difference between the transport behavior of SSE in liquid and solid phases is the saturation of current with the increasing driving voltage, which is associated with the BC plateau in *I-V* curves. Fig. 3.6 shows a typical measured current *I* as a function of the driving voltage V_d for electrons in liquid (red symbols) and solid (blue symbols) phases. For SSE in liquid phase, the coupling between the electrons and ripplons is independent of the external driving field, leading to a linear dependence on the driving voltage V_d. Contrarily, for SSE in solid phase, the coupling between the electron crystal and dimple lattice formed by the resonantly emitted ripplons increases with the driving field, as described in Section 1.6. The three distinct regimes of the nonlinear WS transport, the linear regime, the BC plateau and the sliding regime are highlighted by three shaded areas in Fig. 3.6(a). Note that the current plateau in the BC scattering regime is given by

$$I_\mathrm{BC} = e n_s v_\mathrm{max} W_\mathrm{eff} = e W_\mathrm{eff} \left(\frac{\alpha}{\rho}\right)^{1/2} \left(\frac{8\pi^2}{\sqrt{3}}\right)^{1/4} n_s^{5/4}, \tag{3.5}$$

which is independent of the driving frequency. This is demonstrated in Fig. 3.6(b), which shows the *I-V* curves taken for three different driving frequencies. On the other hand, the threshold voltage for sliding of WS from DL is very sensitive to the driving frequency. In Ref. [93], the threshold sliding voltages were measured using a Corbino disk device in the presence of magnetic filed perpendicular to the helium surface and an empirical formula
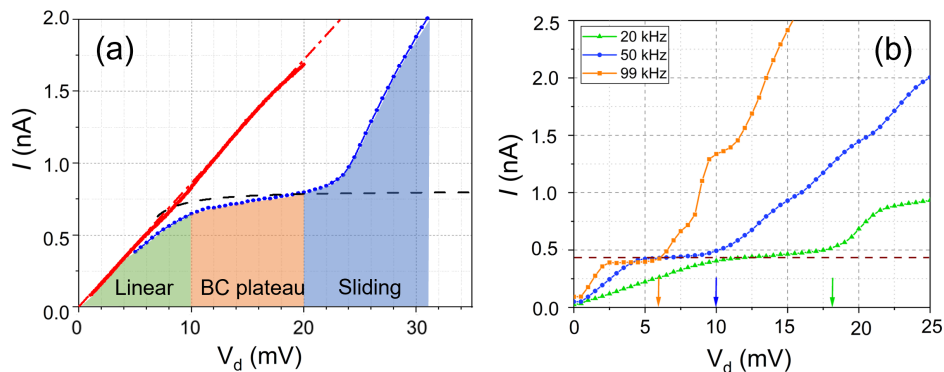
Figure 3.6: Measured *I-V* characteristics of SSE. (a) Red symbols: linear *I-V* dependence for electron liquid. Blue symbols: Nonlinear *I-V* curve for electron solid. The black dashed line indicates the BC plateau and the shaded areas represent the WS in different dynamical regimes. (b) *I-V* characteristics of SSE under three different driving frequencies. The brown dashed line indicates the BC plateau. The color arrows indicate the threshold voltage of sliding, which depends on the driving frequency.

for the sliding voltage V_{th} was given as

$$V_{\text{th}} \propto \frac{n_s^{3/2} E_\perp}{\omega B^{0.8}}, \tag{3.6}$$

which shows an inverse linear dependence on the driving frequency. This roughly agrees with our data taken for SSE in a microchannel device. However, we note that a theoretical model of sliding which could be capable to describe the empirical dependence of V_{th} on various parameters given by Eq. (3.6) is not developed yet. In Section 3.4, using the time-resolved measurements we will show that the measured frequency dependence of V_{th} may be related to the rate of change of the applied sinusoidal driving force within each AC cycle.

3.3.2 Multi-step structure of *I-V* curves

In most of the experiments reported earlier, the *I-V* characteristics for WS showed a single plateau. However, the *I-V* curves measured in our device exhibited a more complicated multi-step structure, as shown in Fig. 3.7(a). This figure shows the *I-V* curves for different

values of the channel voltage V_{ch}, which determines the density of SSE in the central channel. Fig. 3.7(b) shows the corresponding phase differences between the measured current I and driving voltage V_d. It is instructive to discuss the observed variation of phase in the framework of the lumped circuit model given by Fig. 3.2(b). As expected, SSE in the liquid phase ($V_{ch} = 0.6$ V) exhibit the linear transport with a constant phase ($\theta \approx 90°$), which indicates that SSE is moving out of phase with the driving voltage. This corresponds to a nearly pure capacitive coupling corresponding to negligible R_{ch}. Contrarily, for higher biasing voltages the current is nonlinear and exhibits a series of flat plateaus and abrupt rises in the I-V curves, which might suggest a different dynamical state of the sliding electron system. Such a step-like structure becomes more pronounced with increasing V_{ch} and exhibits longer plateaus with varying V_d. The colored dashed lines indicate the first-plateaus, which can be identified with the conventional BC plateaus described by Eq. (3.5). From this expression, one can obtain electron densities $n_s = 5.4$, 8.2 and $13 \times 10^8 \, \text{cm}^{-2}$, which are in good agreement with the densities obtained from the COMSOL simulations. It should also be noted that the BC plateau in (a) corresponds to the drop of phase in (b), which means the coupled system tends to move in phase as the driving voltage increases. This is also well-understand in terms of the lumped circuit model. Since the coupling between the WS and DL is enhanced, R_{ch} also rises leading to a resistive coupling with $\theta < 90°$. Finally, for sufficiently strong V_d, the strongly coupled system eventually decouples, the WS then move out of phase with the driving voltage, leading to a increase of θ.

It is instructive to represent these data in the form of the field-velocity characteristics, similar to the ones shown in Fig. 3.1(c). Using the expression $E = c_1^2 V_d \cos\theta / L$ (see Eq. (3.3)), where the value of θ is given by Fig. 3.7(b) and $L = 100 \, \mu\text{m}$ is the length of the central channel, the resulting field-current characteristics for different values of V_{ch} are shown in Fig. 3.8. Clearly, the sharp increase corresponds to the BC plateau, where the coupled WS-DL system tends to move with a constant velocity. It is also clear that the multi-step structure of the I-V curves shown in Fig. 3.7(a) results from the oscillating
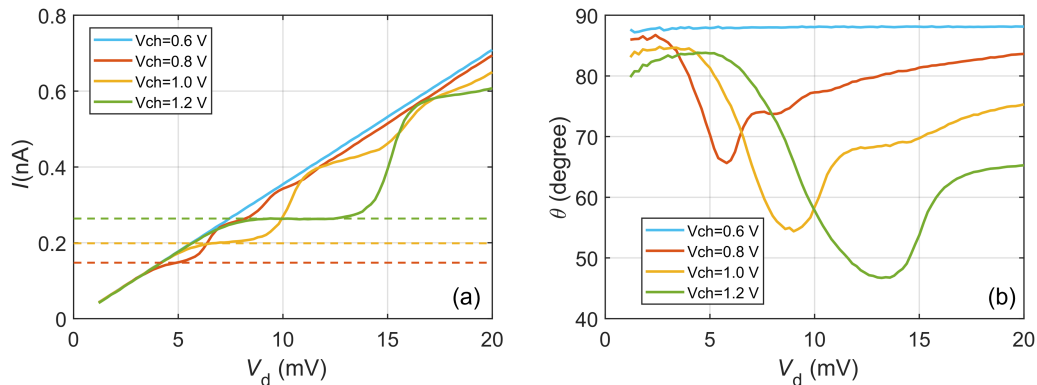
Figure 3.7: The multi-plateau behavior under different biasing voltages.
(a) Current magnitude I versus driving voltage V_d obtained at $T = 150$ mK, and several values of the channel voltage $V_{ch} = 0.6$, 0, 0.8 , 1.0 , and 1.2 V. The dashed lines indicate the BC plateaus corresponding to electron densities $n_s = 5.4$, 8.2 and $13 \times 10^8 \, \text{cm}^{-2}$, as described in the text. (b) The corresponding phase differences between the measured current I and driving voltage V_d.

behavior of the corresponding field-current characteristics.

Remarkably, our result is very similar to the field-velocity dependence reported by Glasson *et al.*, see Fig. 3.1(b), who interpreted the periodic oscillations as an evidence of a dynamical phase transition in a quasi-1D system with discrete rows of electrons (current filaments) [8]. According to this interpretation, the total number of electron rows N_y across the channel is fixed since the confining potential does not change. Instead, the dynamical order of each row is changed by increasing the driving field. Each row can be either *dynamically pinned* to the ripplons at a velocity v_1 of the DL or *decoupled* from the DL and move at a velocity v_2, with $v_2 \gg v_1$. It was suggested that the pinned phase appears in the center of the channel, whereas the sliding phase is near the edge of the channel. The measured velocity in the central channel is the sum of the velocities of each discrete row. The average velocity $\overline{v}$ is then given by $\overline{v} = \alpha v_1 + (1 - \alpha)v_2$, where $\alpha \equiv N_y^{\text{pin}}/N_y$ represents the fractions of rows that are pinned to DL across the channel. The driving field E as a function of $\overline{v}$ is also affected by the formation of the discrete sliding rows. As the average electron velocity (measured current) increases by adding a
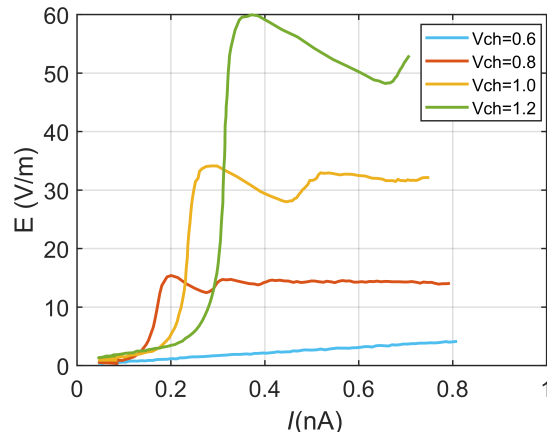
Figure 3.8: Corresponding plots of the field-current characteristics for each value of the channel voltage used in Fig. 3.7. The in-plane driving electric field E acting on the electrons is extracted from the data shown in Fig. 3.7, as described in the text.

sliding row, the $E(\overline{v})$ curve "switches" between discrete values as suggested by the solid lines in Fig. 3.1(b). As a result, Glasson *et al.* concluded that the appearance of discrete sliding rows results in the oscillations of the driving field, which are equally spaced in electron velocity.

It is worth to mention the difference between the geometries of our device and the device used by Glasson *et al.* [8]. In our device, the microchannel arrays which comprise the two reservoirs are aligned parallel to the central channel, whereas in the device used by Glasson *et al.* the microchannels of the two reservoirs were aligned perpendicular to the central channel. Both of the parallel and perpendicular configurations were tested in the experiments reported by Ikegami *et al.* (see Fig. 3.9), who observed step-like *I-V* curves only for the perpendicular configuration similar to that of Ref. [8], while no such behavior was observed for the parallel channel geometry similar to ours [9]. Thus, the authors concluded that, since the observed effect depended on the device geometry, it was not associated with electron motion in the central channel. Instead, Ikegami *et al.* attribute the effect to the transport behavior of electrons in the reservoirs. Nevertheless, in our device we observe exactly the same behavior of the field-velocity characteristics as reported in Ref. [8], which demonstrates that the effect is geometry-independent.
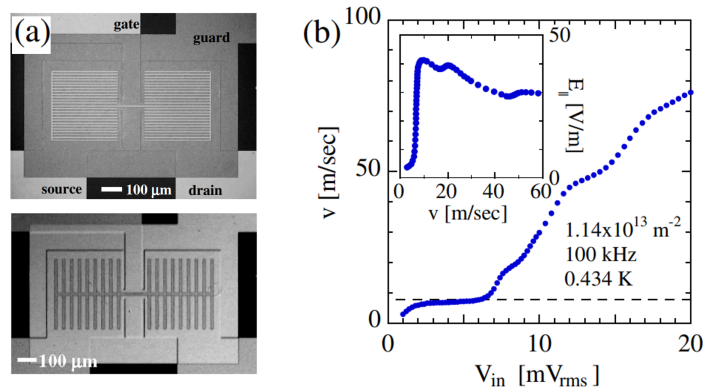
Figure 3.9: (a) The SEM picture of the devices used in Ikegami's experiments. Top: parallel configuration. Bottom: perpendicular configuration. (b) The obtained drift velocity v as a function of driving voltage V_{in} using the bottom device in (a). The dashed line represents the calculated drift velocity limited by the BC effect. Inset: The driving field $E_{||}$ versus v. The figure is reproduced from Ref. [9].

Contrarily to the explanation given by Glasson *et al.*, we provide another explanation for the observed field-velocity characteristics and confirm it in experiment. In particular, we show that the oscillating field-current characteristics originate from a repeated dynamical decoupling (slipping) and recoupling (sticking) of the whole WS from/to DL. Our experiment and explanation are presented in the next section.

3.4   Time-resolved transport measurements

In the previous sections, we demonstrated the transport measurements based on the time-averaged lock-in response. Since the sinusoidal driving electric field acting on the surface electrons alternates with the frequency of tens of kHz, while the intrinsic frequency of the electron-dimple system is typically on the order of tens to hundreds of MHz (the frequency of resonant ripplons), the exact details of the system dynamics are hidden in the current response measured with a lock-in amplifier. Therefore, it is desirable to investigate the time-resolved response of the system during one cycle. In this section, we describe the time-resolved transport measurements to track the real-time dynamics of electrons at each point of the nonlinear I-V curve obtained from the time-averaged lock-in response.

Based on these results, we demonstrate that the unusual multiple plateaus observed in I-V curves is a consequence of the stick-slip motion of a uniform WS.

The first time-resolved transport measurements of surface electrons in a microchannel device were reported by Rees *et al.*, where electrons were driven by a linear voltage ramp [10]. Motivated by this work, we performed similar time-resolved transport measurements for electrons in the same microchannel device as discussed in the previous section under an AC sinusoidal driving. A time-resolved current response over several cycles of the AC driving was measured using a room-temperature fast current preamplifier (Femto DHPACA-100) connected to the RR electrode by a semi-rigid Nb/stainless-steel coaxial cable with the total capacitance of approximately 300 pF. This parasitic capacitance together with the input impedance of the preamplifier formed a low-pass filter which limited the bandwidth of the measurement circuit to about 1 MHz. The time-resolved current traces were recorded by a digital storage oscilloscope (LeCroy 625Zi) and averaged over several thousand cycles to improve the signal-to-noise ratio. A small current component due to the crosstalk between the bottom electrodes was separately measured and subtracted from the averaged traces. Fig. 3.10 schematically show the difference between the time-averaged and time-resolved setups.
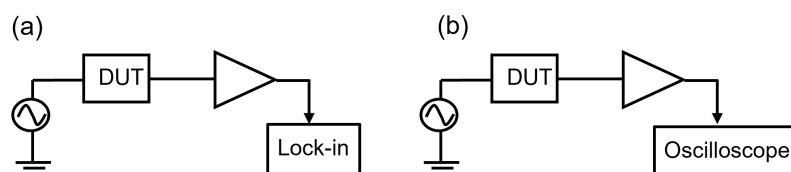
Figure 3.10: The measurement setup for the conventional time-averaged (lock-in) method (a) and the time-resolved method (b).

3.4.1 Time-resolved current response in different regimes of WS transport

We first compare the time-resolved response for different regimes on the *I-V* curve, as shown in Fig. 3.7(a). For small driving voltage $V_d = 5$ mV, WS is in the linear transport regime. Correspondingly, the output current is sinusoidal (blue line in Fig. 3.11(b)). For higher driving voltages $V_d = 10$ mV the transport of WS is in the BC scattering regime corresponding to a plateau in the time-averaged *I-V* curve, see Fig. 3.11(a). Correspondingly, the current saturates at a maximum value given by I_{BC} during each driving cycle, which results in a nearly rectangular shape of the time-resolved current response (orange line in Fig. 3.11(b)). Finally, at sufficiently high driving voltage $V_d = 15$ and 20 mV, WS decouples from DL, which results in a significant increase of the current magnitude shown in Fig. 3.11(a). In the corresponding time-resolved current trace (yellow and green line in Fig. 3.11(b)), we observe an abrupt rise of current which occurs around the peak value of the AC driving electric field, representing a sudden increase of the drift velocity of WS. Soon after this rise the current decreases back to the plateau value I_{BC}, thus producing a narrow spike of current in the time-resolved response. Clearly, this spike cannot be resolved by the conventional time-averaged measurements. Similar behavior was observed in Ref. [10] for electrons driven by a linear voltage ramp. This has a simple phenomenological explanation. As the WS slides from the dimples and the current through the central channel increases, the electrons are transferred rapidly between the two reservoirs, thus decreasing the potential difference between the two opposite ends of the microchannel. As a result, the driving electric field acting on the electrons in the central channel rapidly decreases. It is reasonable to suggest that electrons in the sliding state retain their long-range crystalline order due to the very strong Coulomb interaction, although some heating effects might occur immediately after the sliding onset [91]. Therefore, when the driving field falls below the sliding threshold, WS re-enters the BC scattering regime. Accordingly, the electron system is pinned again by the commensurate

DL and the current magnitude returns to the plateau value I_{BC}. The WS undergoes a *stick-slip motion* due to dynamical decoupling from, and recoupling to, the commensurate DL [10].

Figure 3.11: (a) Time-averaged I-V curve. (b) Typical time-resolved current response to a sinusoidal driving. The color arrows on the I-V curve for $V_{\mathrm{ch}} = 1.2$ V indicates four different values of V_{d} for which real-time traces are presented in (b).

3.4.2   Repetitive stick-slip process

Upon establishing the correspondence between the time-averaged and time-resolved measurement results, we now examine the time-resolved current traces corresponding to the multi-step I-V curves shown in Fig. 3.12(a). Fig. 3.12(b) show examples of such current traces obtained at $T = 150$ mK and the channel voltage $V_{\mathrm{ch}} = 0.8$ V for four different driving voltage amplitudes $V_{\mathrm{d}} = 5$, 10, 15 and 20 mV. Note that under this channel voltage, the electron density, holding electric field and effective channel width are all reduced compared to those at $V_{\mathrm{ch}} = 1.2$ V. Thus, the BC plateau, as well as the WS-DL decoupling threshold force, are significantly reduced. The stick-slip process can happen earlier during the first quarter-cycle and there is sufficient time to repeat the same process until $V_{\mathrm{d}}(t)$ enters the second quarter-cycle. For $V_{\mathrm{d}} = 5$ mV, the system already enters the BC scattering regime, correspondingly the current is saturated at a plateau value I_{BC} and the time-resolved current response has a rectangular shape as described above. For $V_{\mathrm{d}} = 10$ mV, which corresponds to the third step in the time-averaged curve

(see Fig. 3.12(b)), the time-resolved current trace reveals two stick-slip peaks of current due to a repeated decoupling-recoupling process. For still larger values of $V_d = 15$ and 20 mV, the time-averaged I-V curve is almost linear. Remarkably, the corresponding time-resolved current traces clearly show repetitive stick-slip motion of WS, which undergoes three and four cycles of the decoupling-recoupling process during one AC driving cycle. We can intuitively assume that the peak amplitude is proportional to the rate of change of the driving field (dV_d/dt). It should also be noted that in previous section (see Fig. 3.6(b)), we presented a frequency dependence of the voltage threshold, that is the sliding threshold decreases as the driving frequency increases. This phenomenon may also relate to the rate of change of the driving field. Since higher frequency corresponds to the larger value of dV_d/dt, the driving voltage can attain the critical value within a very short time and lead to the decoupling of the WS and DL.
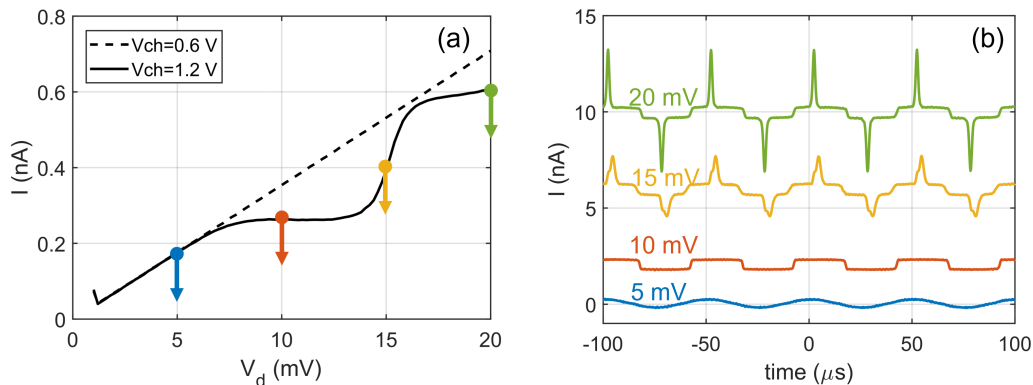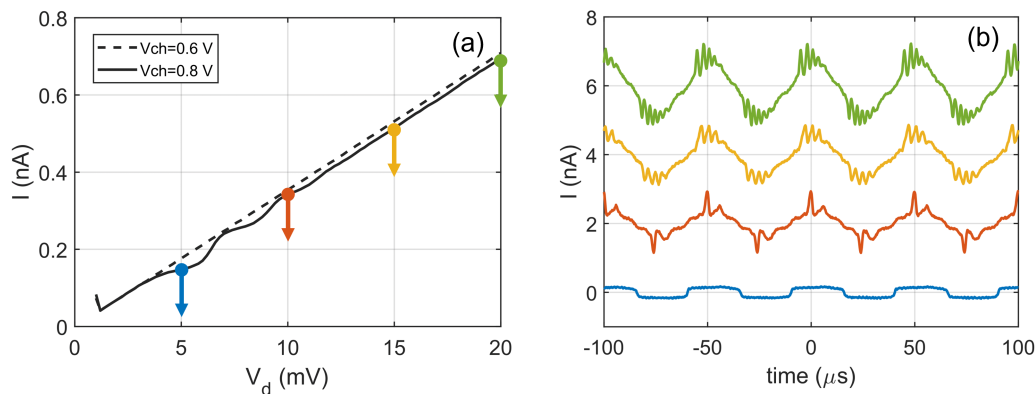

Figure 3.12: (a) Time-averaged I-V curve. (b) Typical time-resolved current response to a sinusoidal driving. The color arrows on the I-V curve for $V_{ch} = 0.8$ V indicates four different values of V_d for which real-time traces are presented in (b).

3.4.3 Discussion

Our time-resolved current measurements provide compelling evidence that the unusual transport behavior of the WS reported by Glasson *et al.* and interpreted as evidence for a nonequilibrium phase transition in a driven electron system in fact arises from

the dynamical interaction of the electron lattice with the surface dimples on the liquid substrate. For higher values of V_{ch}, which correspond to both higher electron densities and larger pressing electric fields, we expect stronger coupling between the electrons and dimples. In turn, we expect that the sliding of WS from DL should occur at higher driving field thresholds, see Eq. (3.6). The density can be estimated from the value of the plateau current I_{BC} using the expression given by Eq. (3.5). As an example, three values of I_{BC} corresponding to plateaus on the I-V curves for $V_{\text{ch}} = 0.8$, 1.0 and 1.2 V are indicated in Fig. 3.7(a) by dashed lines, from which we estimate the corresponding density $n_s = 5.4$, 8.2 and $13 \times 10^8 \, \text{cm}^{-2}$, respectively. Note that these values agree reasonably well with estimated values of n_s using Eq. (2.4) and COMSOL simulation. For the largest value of $V_{\text{ch}} = 1.2$ V used in our experiment, we observe a plateau and a rise in current similar to the conventional results [12, 93, 94]. Nevertheless, there is an indication of a second plateau at sufficiently large driving voltages $V_{\text{d}} \gtrsim 20$ mV (see Fig. 3.11(a)), and it is therefore possible that the second sliding event would occur at still higher V_{d}. The repetitive pinning-sliding becomes clearly evident at lower values of V_{ch} where the coupling between the electrons and dimples is weaker. We note that multiple decoupling was also observed in Ref. [10] by increasing temperature T towards the value $T_m = e^2 \sqrt{\pi n_s}/(k_B \Gamma)$ (here $\Gamma \approx 137$ is the plasma parameter discussed in Section 1.3.1) corresponding to the melting temperature of the WS. This agrees with our result because the coupling strength and decoupling threshold will also decrease with increasing T [93]. Interestingly, the melting temperature of 150 mK would correspond to an electron density $n_s = 0.5 \times 10^8 \, \text{cm}^{-2}$, which is significantly lower than the estimated density for $V_{\text{ch}} \gtrsim 0.6$ V. This suggests that the electron system is already in the solid phase at $V_{\text{ch}} = 0.6$ V, despite its linear response across the range of driving voltages used in the experiment. This could be due to a continuous and rapidly repeated coupling-decoupling process, in the limit of which the WS is essentially decoupled from the heavy DL and thus exhibits a high mobility comparable to that of electrons in the liquid phase.

We note that the step-like structure of the I-V curves has not been clearly observed

in a similar experiments using microchannel device with channel depth of $1.6\,\mu$m [69]. Contrarily, all our microchannel devices with depth of $4\,\mu$m exhibited this effect very clearly. This is in agreement with our earlier discussion of the effect of the pressing electric field acting on the electrons. Indeed, in the channel of smaller depth electrons experience a significantly stronger pressing electric field, which enhances the coupling of electrons to the dimples and suppresses their repetitive stick-slip motion. This argument might also explain why this effect was not observed by Ikegami *et al.* who used a microchannel device with the channel depth of $1.7\,\mu$m, see Fig. 3.9. Also note that, besides the pressing electric field, the appearance of multiple stick-slip motion is susceptible to other experimental parameters, such as proximity to the Wigner solid transition, as discussed earlier.

Finally, it is instructive to discuss the timescale of the observed stick-slip transitions, which is relevant to the timescale of the field redistribution, as well as the characteristic frequency of the DL formation. As described above, the redistribution of electrons between the two reservoirs can affect the driving electric field acting on the electrons in the central channel. The typical rate of this process is given by $(R_{\mathrm{ch}}C)^{-1}$, where $C = 0.6$ pF is the capacitance between electrons and reservoir electrodes. For a typical resistance $R_{\mathrm{ch}} = 700$ kΩ of the WS in the sliding state, we estimate the corresponding frequency to be 2.4 MHz. Another relevant process is the characteristic inverse time of the DL formation, which is close to the frequency of the resonant ripplons $\sim \sqrt{\sigma/\rho}n_s^{3/4}$. For the typical electron densities achieved in our experiment, this frequency is in a range 10 to 100 MHz. Both of these time scales is significantly smaller than the bandwidth of our experimental setup (about 1 MHz), which is mainly due to the bandwidth of our current preamplifier and the low-pass filter formed by its input impedance and the connecting cable, as discussed earlier. Thus we conclude that the observed stick-slip peaks in our time-resolved current traces are broadened by our experimental setup. As a future improvement of our method, we can consider employment of a cryogenic fast current preamplifier which would allow the length of the connecting cable to be decreased significantly, thus improving the response time of our detection circuit.

3.5 Summary

In this chapter, we described our experimental studies of the transport of SSE confined in the microchannel device. In particular, we found an unusual plateau effect when the system is driven out equilibrium. This unusual transport effect was investigated using different methods. First, we confirmed that the effect is intrinsic and independent of the device geometry. Second, by employing time-resolved measurements we showed that the observed effect is due to the dynamical interaction of the electron crystal with the surface excitations of the liquid substrate.

Chapter 4

Rydberg resonance detection for SSE confined in microchannel devices

In this chapter, we present a new method of the Rydberg resonance detection in SSE confined in microchannel devices. The conventional method to detect the Rydberg resonance in a bulk SSE sample containing a large number of electrons ($10^7 - 10^9$) is to observe the corresponding change in the transmitted power of the resonant microwave (MW) radiation due to its absorption by the excited electrons [35]. For the typical density of electrons $n_s \sim 10^8$ cm^{-2}, a single microchannel employed in our experiment would contain on the order of 10^3 electrons, which makes the microwave absorption detection impossible. A new method of the Rydberg resonance detection was developed recently, which is based on the measurement of the image-current induced by the excited SSE in a conducting electrode capacitively coupled to the electrons [4]. While it was argued that this method can be potentially scaled down to the detection of the Rydberg excitation of a single electron, the currently achieved sensitivity of this method is not sufficient to detect the resonance of SSE in a single microchannel. As an alternative, we used the conductive detection of the Rydberg resonance by observing a change in the current of SSE driven along the microchannel, which is induced by the heating of electrons due to the resonant MW absorption [95]. In particular, in order to increase sensitivity of the

conductive detection we employed SSE in a solid state to exploit a large change in the conductivity of SSE upon their transition from the solid to the liquid phase.

This chapter describes the first measurements of the Rydberg resonance in SSE confined in the microchannel device. In particular, we use the conductive detection for SSE in a single channel and the image-charge detection method for SSE confined in an array of microchannels. This chapter starts with a short review of the traditional absorption measurements of SSE on a bulk liquid helium.

4.1   Review of the MW absorption measurement

The first observation of the Rydberg transition by measuring the microwave absorption was done by Grimes *et al.* in 1974 [35]. Since then, the spectroscopic properties have been extensively studied by several groups [70, 95–97]. A schematic drawing of the typical absorption measurement setup used in OIST is shown in Fig. 4.1(a). The MW radiation is generated by a room temperature MW source with a tunable frequency in the range $\omega_{\mathrm{mw}}/2\pi = 110\text{-}170$ GHz. The MW power is controlled by an attenuator from a few μW to a few mW and is introduced from the cryostat's top to the sample cell via a MW guiding system. The main part of the guiding system is an overmoded (WR-28) stainless-steel waveguide, while its short portion entering the cell is a single-mode WR-6 copper waveguide sealed with a piece of 50-μm thick Kapton film. The benefit of an overmoded waveguide is that it has lower power losses due to a larger cross-section. The power loss in passing the waveguide was estimated to be -10 dB. The MW radiation passes through the cell and is detected by an indium antimonide (InSb) bolometer mounted on the opposite side of the cell. The MW power transmitted to the bolometer is obtained by measuring the voltage drop across the bolometer, which is externally biased by a constant current I_{dc}, as shown in the inset of Fig. 4.1(a). Typically, the bolometer has the sensitivity of 10 kV/W and the time constant for the detection circuit is about 1 μs.

Inside the sample cell, a parallel-plate capacitor is used to providing a uniform pressing

fields acting on SSE, see Fig. 4.1(b). The pressing field $E_\perp$ is controlled by changing
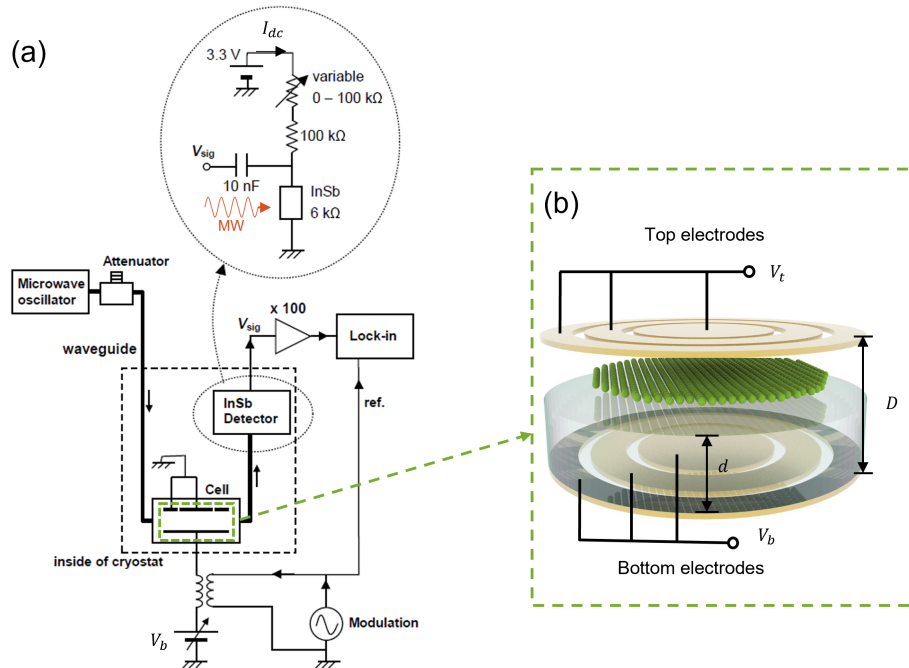
Figure 4.1: (a) Block diagram of the experimental setup. Inset: Circuit diagram of the InSb detector. The figure is reproduced from [97]. (b) The geometry of the parallel-plate capacitor. The top and bottom electrodes are separated by a distance D. And d is the liquid level.

the voltage applied to the capacitor plates, according to the parallel-capacitor model, see Eq. (2.2). In particular, when the parallel capacitor is half-filled with helium ($d = D/2$), the pressing field becomes independent of the electron density n_s and is completely determined by the applied voltages, that is $E_\perp = (V_\mathrm{b} - V_\mathrm{t})/D$. To observe the transitions of SSE between the Rydberg states, the microwave frequency is usually fixed, while the transition frequency of the Rydberg states is Stark-tuned in resonance by sweeping V_b. To measure the absorption signal V_sig, the applied voltage V_b is amplitude-modulated with a frequency ω_mod, that is $V_\mathrm{b}' = V_\mathrm{b} + A\sin(\omega_\mathrm{mod}t)$, where A is a small modulation amplitude. The output voltage is measured by a lock-in amplifier at the modulation frequency during the sweep of V_b, and the measured voltage is proportional to the first derivative of the absorption signal V_sig with respect to V_b at sufficiently small modulation amplitude A, see Fig. 4.2(a). Fig. 4.2(b) shows a representative trace of the derivative of

the absorption signal measured for about 10^7 electrons. It was found that the sensitivity of the transitional absorption measurement is not sufficient to detect the Rydberg transition in a system which contains less than 10^6 electrons [97].
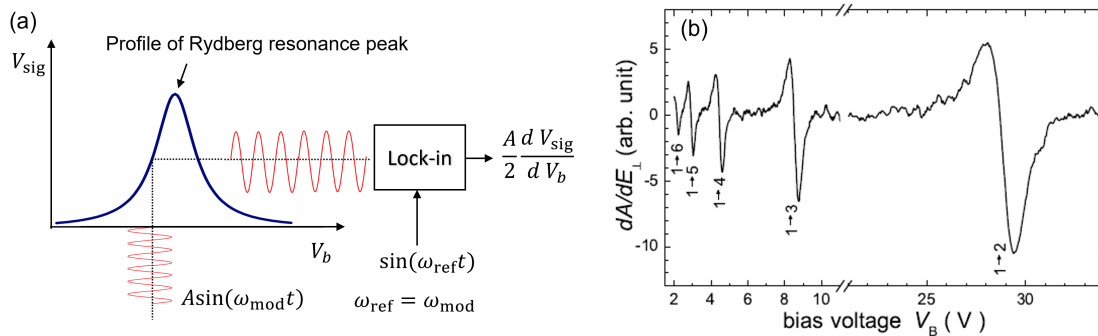
Figure 4.2: (a) Schematic diagram of the MW absorption measurements using the amplitude modulation technique. (b) An experimental trace of the derivative of the absorption signal. The figure is taking from Ref. [97].

4.2   Conductive detection of the Rydberg resonance in SSE confined in a single microchannel

In this section, we report the first observation of the microwave-induced Rydberg resonance in the SSE confined in a single 20-μm wide and 100-μm long channel. The resonance signal from a few thousand of surface electrons is detected by observing WS melting due to the microwave absorption. Compared with the conventional MW absorption measurement described in the previous section, this method can provide higher sensitivity and does not require expensive devices such as the InSb bolometer.

4.2.1   Method and setup

The experimental setup consists of two main parts, the MW setup and the conductivity measurement setup. The MW setup is very similar to the conventional setup used in

the MW absorption measurements, as described in the previous section, although the operating frequency is in the range $\omega_{\mathrm{mw}}/2\pi = 400\text{-}500$ GHz. The higher MW frequency is required because SSE in a microchannel experience significantly larger pressing electric field $E_\perp$ than on the bulk, thus shifting the transition frequency of SSE to much higher values. In our experiment, we kept the frequency of MW radiation fixed and tuned the Rydberg transition frequency ω_{21} of SSE in the central channel via the Stark effect by adjusting the pressing electric field $E_\perp$ acting on SSE. Practically, this was done by varying the voltage V_{ch} applied to the bottom electrode of the central channel. Note that, in addition to V_{ch}, a strong contribution to the pressing electric field $E_\perp$ acting on SSE comes from the image charges induced by SSE in the conducting electrode at the bottom of the channel, as will be described in Section 4.3. The conductivity measurements are done by the ST method similar to that described in Chapter 3.

The nonlinear transport features of WS described in Section 3.3 suggest the possibility to detect the microwave-induced Rydberg resonance of SSE confined in the central channel. It is well known that the resonant MW excitation of the Rydberg transition can result in a strong overheating of the electron system due to the microwave absorption and elastic decay of the excited electrons [95]. Suppose that at a given driving voltage V_{d} the current of WS in the central channel is set at the BC plateau, see Fig. 4.3(a). The resonant excitation of SSE will cause the heating of SSE and, at sufficiently large MW power, melting of WS. As a result, the current of SSE through the central channel must experience an abrupt increase by ΔI to its value corresponding to the linear transport of SSE in the liquid phase, as indicated in Fig. 4.3(a). Alternatively, even if the applied MW power is not sufficient to melt WS there must be an appreciable change in the transport of WS induced by the excitation, as was previously demonstrated [98]. Such a method of the Rydberg resonance detection by observing an abrupt change in the WS transport is used in the experiment described here.

Due to the upper-frequency limit of our MW source, the typical values of V_{ch} required to tune SSE into resonance ($\omega_{21} = \omega_{\mathrm{mw}}$) were significantly lower than 1.2 V, the value
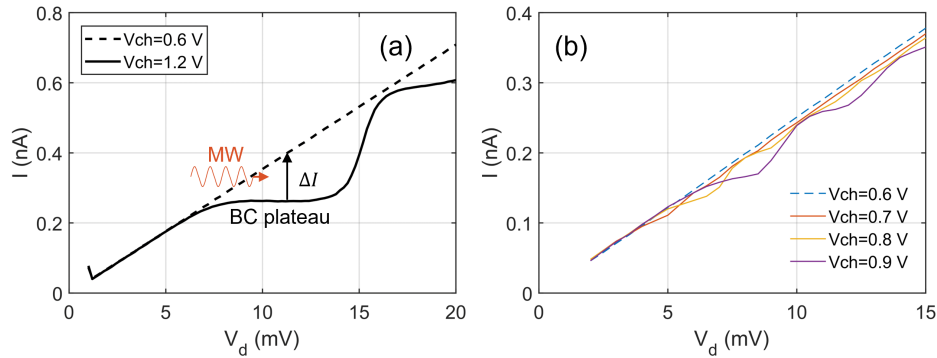
Figure 4.3: (a,b) *I-V* dependence of SSE in the central channel measured without MW radiation at $T = 150$ mK for different values of the channel voltage V_{ch} and fixed gate voltage $V_{ga} = 0$.

used to obtain the nonlinear transport curve shown in Fig. 4.3(a) (the solid black line). The useful range of V_{ch} for the given bandwidth of our source was found to be in the range 0.7-0.9 V. Fig. 4.3(b) shows the *I-V* curves of SSE in our device taken without MW excitation for a fixed gate voltage $V_{ga} = 0$ and several different values of V_{ch} in the above range. At $V_{ch} = 0.6$ V the electron system shows the linear *I-V* dependence corresponding to SSE in the liquid phase. With increasing V_{ch}, therefore with increasing density n_s, the *I-V* curves start exhibiting nonlinear features, in particular a series of plateaus followed by the abrupt rises in current. As described in the previous chapter, this behavior is identified with the repetitive coupling and decoupling of WS to and from the liquid surface deformations [92], which is sort of an intermediate regime between the linear transport and strong pinning of WS in the resonant BC-emission regime. The observed nonlinear transport of WS still makes it suitable for the proposed detection of the Rydberg resonance by the electron heating, although with a reduced sensitivity compared with the case discussed in relation to Fig. 4.3(b). The experimental procedure was to apply the MW radiation at a fixed frequency ω_{mw} and measure the abrupt change of SSE in the central channel while sweeping the channel voltage V_{ch}. The results of such measurements are discussed in the next section.

4.2.2 Results

Figures 4.4(a) and 4.4(b) show variation of the changes in the current magnitude ΔI and phase $\Delta\theta$, respectively, with the channel voltage V_{ch} at a fixed gate voltage $V_{\text{ga}} = 0$ for SSE exposed to radiation at different values of MW frequency. In order to obtain the changes ΔI and $\Delta\theta$ upon irradiation, the corresponding data obtained without radiation were subtracted. The current was measured for a range of driving voltages V_{d} determined by the position of BC plateau. Due to slight overheating of the experimental cell by the MW radiation, the temperature T varied in a range from 170 to 190 mK for different traces. An abrupt change in current I with respect to its value without radiation indicates overheating of the electron system by the microwave absorption due to the resonant transitions between the Rydberg states. As shown in the following section, this corresponds to the transition of SSE in the central channel from the ground state to the first excited Rydberg state. As expected, the position of the resonance shifts towards the higher values of V_{ch} with increasing MW frequency due to the Stark effect.
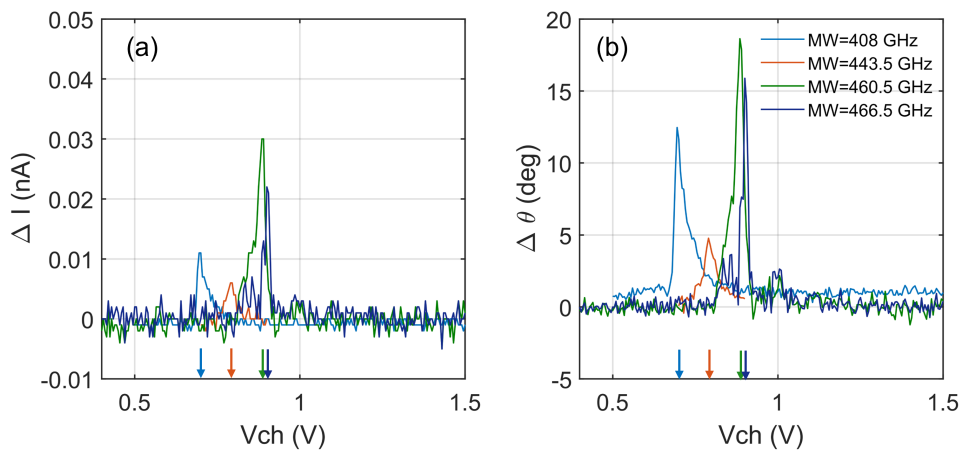
Figure 4.4: Variation of the change in current magnitude ΔI (a) and phase $\Delta\theta$ (b) with the channel voltage for SSE under irradiation for several values of the MW frequency. The values of ΔI were obtained from the measured current by subtracting the values of current measured without the radiation. An abrupt change in current indicates the resonant MW-induced transitions of SSE from the ground state to the first excited Rydberg state. Arrows indicate resonant values of $V_{\text{ch}} = 0.7$, 0.78, 0.88 and 0.9 V corresponding to the peak values of ΔI for each MW frequency.

The measured resonance signal exhibits large broadening and a rather complicated line shape. The observed signal broadening, on the order of 10 GHz, is many orders of magnitude larger than the intrinsic linewidth of the Rydberg transition [70], see Section 1.7. As shown in the following section, this large broadening arises due to the inhomogeneous broadening of the Rydberg transition of SSE in the central channel because of the variation of the pressing electric field $E_\perp$ across the channel. It is hard to account for the rather irregular asymmetric shape of the signal. In addition, it should be noted that the detection method realized here does not measure the transition rate directly. Instead, it probes the electron conductivity in response to the transition-induced heating of SSE. In order to fully account for the shape of such conductivity response one has to consider dependence of the electron temperature on V_{ch}, the corresponding change in the conductivity and measured current, etc. Also note that the electron density n_s in the central channel varies with V_{ch}.

4.2.3   Discussion

The pressing electric field $E_\perp$ acting on SSE in the central channel is due to the image-charges induced in the channel and gate electrodes by SSE and voltages applied to these electrodes. An approximate relationship between the values of $E_\perp$ and V_{ch} was established in Section 2.2.2 by using a simplified parallel-plate capacitor model, see Eq. (2.5). Note that, compared to the conventional microchannel devices, our channel depth d is significantly larger. According to Eq. (2.5) this allows us to use a larger voltage V_{ch} to reach the required pressing field $E_\perp$ to tune SSE in resonance with the applied MW radiation. This provides higher resolution for detecting the Rydberg transition by scanning the channel voltage.

Fig. 4.5 shows the values of the pressing field $E_\perp$ corresponding to the peak position of the resonance signals shown in Fig. 4.4 for each microwave frequency ω_{mw} (blue open circles). These values are obtained from the corresponding values of V_{ch} indicated by arrows in Fig. 4.4 using Eq. (2.5) in Chapter 2 with $d = 4~\mu\mathrm{m}$, $V_e = 0.2$ V and $c_1 = 0.8$
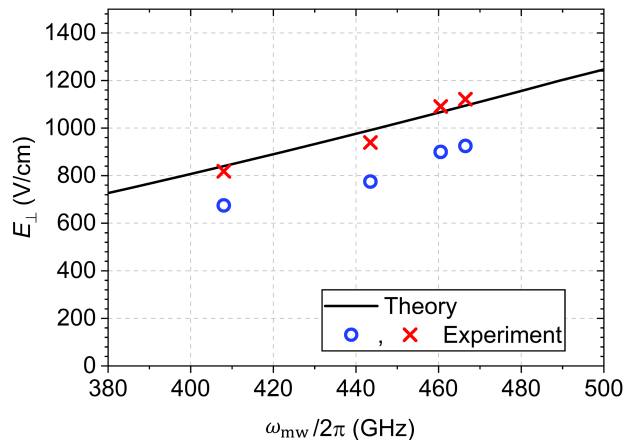
Figure 4.5: Pressing electric field $E_\perp$ corresponding to the resonant MW frequency ω for the transition from the ground state to the first excited Rydberg state calculated using the infinite-barrier approximation (solid line). The blue open circles and red crosses represent the pressing field determined from the experimental data shown in Fig. 4.4 using the parallel-plate capacitor model with $d = 4$ and 3.3 μm, respectively, as described in the text.

determined from the experimental data. For the sake of comparison, the solid line shows the relationship between the frequency ω_{21} and $E_\perp$ calculated by solving the 1D stationary Schrodinger equation for the electron motion perpendicular to the liquid surface assuming an infinitely large potential barrier at the liquid-vacuum interface, see Fig. 1.2(b) (blue line). The experimental data exhibit a similar slope of the frequency-field dependence, which indicates that the observed resonance corresponds to the MW-excited transitions from the ground state to the first excited Rydberg state. At the same time, the values of $E_\perp$ estimated from the experimental data are noticeably lower than the theoretical ones. The most probable cause for such discrepancy is the failure of the parallel-plate capacitance approximation, where we assume a flat surface of liquid helium with the depth d equal to the height of the channel walls. As mentioned in Section 2.3.1, the actual surface of liquid in a microchannel is curved due to the capillary effect and pressure exerted by SSE on the surface of liquid helium [28]. A better approximation is to consider a surface having the round shape with the radius of curvature given by Eq. (2.7). We note that the

exact value of h can not be measured in our experiment, therefore we did not attempt to take into account the deviation of the surface shape from the flat one. Nevertheless, the depression of the surface of liquid due to the curvature can be roughly taken into account by assuming somewhat lower depth of the liquid d compared with the height of the channel walls. For example, the red crosses in Fig. 4.5 show the values of $E_\perp$ estimated from the experimental data using Eq. (2.5) assuming $d = 3.3~\mu$m. Thus, we conclude that the approximate parallel-plate model already accounts reasonably well for the obtained experimental data.

The above model does not provide an estimation for the distribution of $E_\perp$ across the electron system, which is important to know in order to account for the broadening of the Rydberg resonance line. In order to get more insight into this problem, we performed FEM calculations of the electric potential distribution across the channel for an infinitely long channel using the COMSOL software, as described in Section 2.4. Similar to the parallel-plate capacitor model, in our numerical simulations we assume a flat surface of liquid helium in the channel and model the SSE as an equipotential plane at potential V_e. Fig. 4.6(a) shows the equilibrium density profiles across the channel calculated for several values of $V_{\rm ch}$ (these values are indicated by the arrows in Fig. 4.4). This result shows that for the typical values of $V_{\rm ch}$ used in our experiment the width of the electron system across the channel is close to the width of the channel. Fig. 4.6(b) shows the corresponding distribution of the pressing electric field $E_\perp$ across the electron system. In this simulation, we assumed the depth of the liquid in the channel $d = 4~\mu$m, which coincides with the height of the channels walls. Note that the average values of $E_\perp$ across SSE for each channel voltage are fairly close to those obtained from the parallel-plate capacitor model, see Fig. 4.5 (open circles).

As seen in Fig. 4.6(b), the simulations reveal the variation of $E_\perp$ on the order of 30 V/cm across the electron system. This variation leads to the inhomogeneous broadening of the Rydberg transition line for the many-electron system. For a given fixed value of the MW frequency, a portion of SSE in the channel experiencing the pressing electric
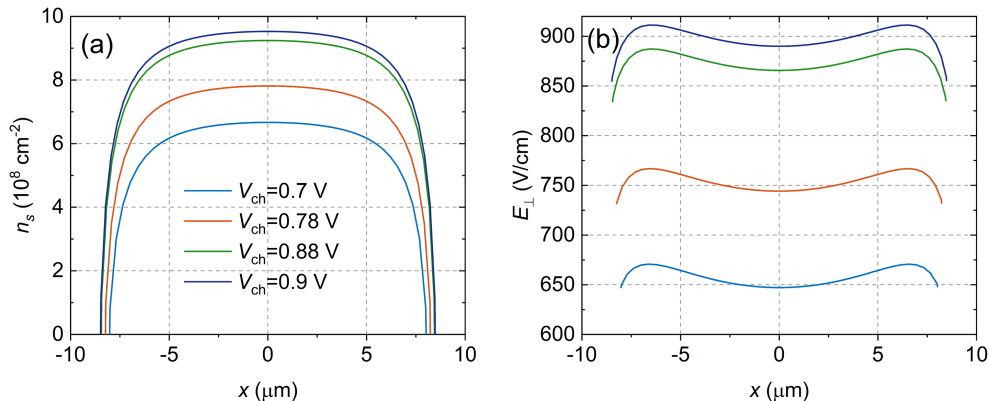
Figure 4.6: (a) The electron density n_s in the central channel versus the distance from the center of the channel calculated for different values of the channel voltage V_{ch} and fixed gate voltage $V_{ga} = 0$. In the simulation, the SSE are represented by an equipotential plane at potential $V_e = 0.2$ V, as described in the text. (b) The corresponding cross-sectional profile of the pressing electric field $E_\perp$ acting on the electrons.

field with a certain resonant value $E_\perp^{(r)}$ will be tuned in resonance with the radiation. The location of this portion and the corresponding number of resonant SSE will depend on the channel voltage V_{ch}. As V_{ch} is increased from a value far below the resonance, it is reasonable to expect that SSE away from the center of the channel, which experience the maximum $E_\perp^{(max)}$ at a given channel voltage, will be resonantly excited by the radiation, when $E_\perp^{(max)} = E_\perp^{(r)}$. As V_{ch} increases further, these electrons will become detuned from the resonance, while the electrons closer to the middle of the channel will become resonantly tuned. As mentioned earlier, it is difficult to account for the exact shape of the resonant signal as SSE are swept through the resonance by the varying field $E_\perp$. Nevertheless, it is reasonable to expect that the broadening of the observed resonance lines will be determined by the variation of $E_\perp$ across the system. Note that the variation of $E_\perp$ observed in the simulations corresponds to the variation of the transition frequency ω_{21} on the order 10 GHz, as determined from the slope of the theoretical line in Fig. 4.5. This is in a reasonable agreement with the broadening of the measured resonance signals shown in Fig. 4.4.

It is important to mention that the final goal toward building the spin qubits using

SSE is to realize the Rydberg transition detection for a single electron. In this sense, the conductivity method is not suitable, because this method is based on the transport properties of a many-electron system. Nevertheless, this work is valuable because it presents the first experimental observation of the Rydberg transition of a small number of electrons confined in a single channel, thus demonstrating feasibility of such experiments in microchannel devices.

4.3   Image-charge detection of the Rydberg resonance in SSE confined in a microchannel array

Recently, a new spectroscopic method for the Rydberg states detection, the image-charge method, has been developed and used to detect the Rydberg transition in SSE on bulk liquid helium [4]. This method is based on the vertical displacement of the excited electrons, thus it directly probes the population of the excited Rydberg states. In this section, we describe an experiment where we adopted the image-charged detection method for SSE confined in our microchannel device.

First, it is instructive to describe the image charge induced in the conducting plates due to the presence of an electron on the helium surface using the parallel-plate capacitor model, which is shown in Fig. 4.7. An electron (green dot) placed in the parallel-plate capacitor, with a distance d above the bottom plate, will induce image charge (blue dots) in both top and bottom plates. The amount of charge induced on the bottom and top plates depends on the position of the electron and are given by $q_b = eh/D$ and $q_t = ed/D$, respectively. When the electron is shifted vertically by a distance Δz, the corresponding induced charges become $q_b' = e(h - \Delta z)/D$ and $q_t' = e(d + \Delta z)/D$. As a result, the change in the image charge in the top and bottom plates is given by $\Delta q = \mp e\Delta z/D$, which conserves the total induced image charge at two plates. This amounts to $|\Delta q| \sim 10^{-5}e$ for the parallel plate disk setup with $D = 2$ mm used in the experiment by Kawakami et $al.$ [4]. For a many-electron system with density n_s, we can apply the same analysis and
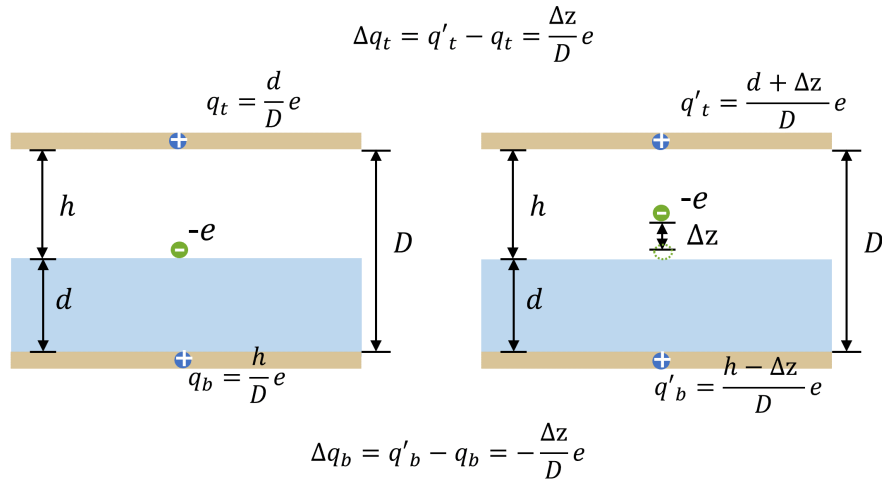
Figure 4.7: Schematic drawing of the image charge induced in a parallel-plate capacitor by an electron inside the capacitor, as described in the text.

the change of the image charge is therefore given by $|\Delta q| = n_s eS\Delta z/D$. For about 10^8 electrons used in the experiment [4], this produced a current on the order 10 pA, which was directly measured using a lock-in amplifier.

The ultimate goal is the image-charge detection of the Rydberg transition of a single electron. The simplest improvement towards increasing the sensitivity of the proposed method is immediately seen, that is increasing the change in the image charge $|\Delta q|$. As follows from the above discussion, this can be done by decreasing the distance D between the capacitor plates. Unfortunately, for a parallel-plate capacitor partially filled with liquid helium this distance can not be made less than ~ 1 mm, the capillary length of liquid helium, otherwise the capacitance will be completely filled with the liquid by the capillary action. For this reason, other electrode structures have to be sought, for example, a coplanar capacitor covered with a superfluid helium film, as was suggested in [4]. An alternative approach is to use the microchannel devices, as SSE floating on the surface of superfluid helium inside a channel are capacitively coupled to the metal electrodes comprising the top and bottom of the channel, therefore they are expected to produce a change in the image charge induced at one of the electrodes equal to $|\Delta q| = \kappa e\Delta z/d \sim 10^{-2}e$, where κ is a numerical factor order of unity, which is determined by

the ratio of the weighted contributions to the total capacitance between SSE and channel electrodes. For the microchannel device used in our experiments, $d = 4\,\mu\text{m}$, thus, the sensitivity of the image-charge detection method is expected to enhance thousandfold for SSE in a microchannel device comparing with the parallel plate disk setup.

4.3.1   Measurement setup

The microchannel device used for the image-charge detection method is similar to that for the conductivity measurements. However, since the amplitude of the image-charge current
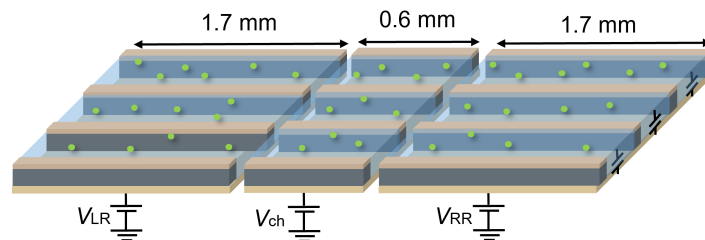
Figure 4.8: Schematic drawing of the multi-channel device.

in our microchannel device is expected to be orders of magnitude smaller than on the bulk liquid helium, due to a much smaller number of electrons, we employed a multi-channel device to increase the total area occupied by SSE. In this setup, we increased the channel length to 600 μm, and used 50 channels arranged in parallel, such that the total surface area is enlarged by 300 times. A schematic view of the multichannel device used for the image-charge detection is shown in Fig. 4.8. In addition, the room temperature current amplifier was replaced by a cryogenic voltage amplifier to enhance the signal-to-noise ratio (SNR). The electrical setup and the schematic cross-sectional view of the microchannel are shown in Fig. 4.9.

In order to estimate the image-charge signal induced by the resonant excitation of the Rydberg transition of SSE, we apply the same analysis as the one used for the parallel-plate capacitor. The change of the image-charge due to the Rydberg excitation ($n = 1 \rightarrow$
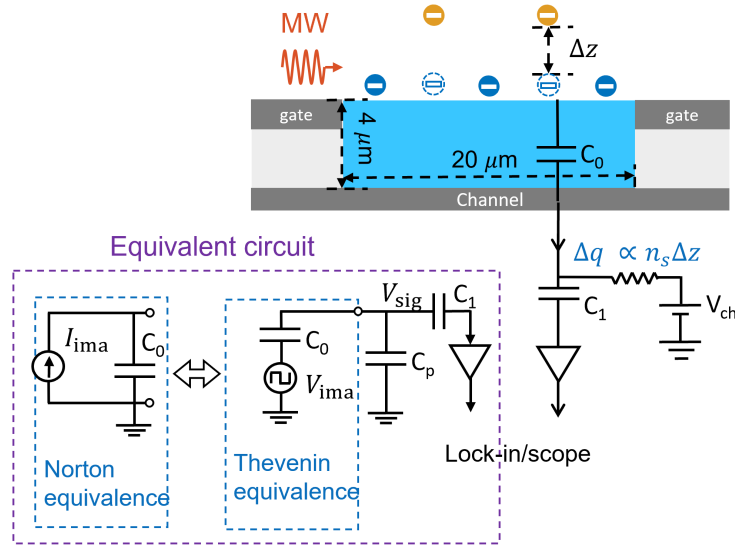
Figure 4.9: schematic view of the microchannel setup for the image charge detection and the equivalent lumped circuit model.

2) is then given by

$$\Delta q \simeq \kappa \rho_{22} S n_s \frac{\Delta z}{d} = 4\pi e n_s \rho_{22} \Delta z C_0, \tag{4.1}$$

where ρ_{22} represents the fraction of SSE excited to the first excited states, $\Delta z \simeq 35$ nm is the difference in the average distance of SSE in the ground state and the first excited Rydberg state at $E_\perp = 0$, and $C_0 \approx \kappa S/4\pi e d$ is the geometrical capacitance of the channel electrode, with $\kappa = 0.8$ estimated from the channel geometry. For typical values of $S = 20 \times 300 \times 50$ μm^2 and $d = 4$ μm, we have $C_0 \simeq 1$ pF, which is comparable to that of a parallel-plate device used in the experiment by Kawakami *et al.* [4].

The change of the image charge induces a current I_{ima} in the channel electrode, which is given by $I_{\text{ima}} = \mathrm{d}q/\mathrm{d}t$. If the fractional occupancy ρ_{22} is time-dependent and varies periodically, for example by using the pulse modulation of the MW radiation at frequency ω_{mod}, we have $\rho_{22}(t) = \rho_{22}^{(0)} \sin(\omega_{\text{mod}} t)$, thus the magnitude of the time-dependent image

current can be written as

$$I_{\text{ima}} = \frac{dq}{dt} = 4\pi e n_s \rho_{22}^{(0)} \Delta z \omega_{\text{mod}} C_0. \tag{4.2}$$

For typical values of $n_s = 10^8$ cm^{-2}, the modulation frequency $\omega_{\text{mod}}/2\pi = 100$ kHz and $\rho_{22}^{(0)} = 1\%$, we have $I_{\text{ima}} \simeq 10$ pA. Since we are measuring the voltage drop, it is reasonable to convert our current source to its Thevenin equivalent circuit, with the image charge voltage $V_{\text{ima}} = I_{\text{ima}}/\omega_{\text{mod}} C_0 \simeq 16$ μV. The measurement circuit is given in the inset of Fig. 4.9. Here, $C_p \simeq 20$ pF is the parasitic capacitance given by a short stainless-steel coaxial cable which connects the cell to the amplifier, and $C_1 = 10$ nF is the capacitance of the bias tee. C_0 and C_p form a voltage divider, therefore we have $V_{\text{sig}} = V_{\text{ima}} \frac{C_0}{C_0 + C_p} \simeq 1$ μV. The image-charge voltage V_{sig} is then amplified by a cryogenic two-stage amplifier and is detected by a standard lock-in amplifier at the reference frequency $\omega_{\text{ref}} = \omega_{\text{mod}}$.

In this experiment, we use a two-stage amplification scheme [99]. It consists of a homemade heterojunction bipolar transistor (HBT) amplifier and a commercially available cryogenic amplifier (Cosmic Microwave Technologies CITLF1). The HBT amplifier is placed in the immediate proximity to the sample cell to minimize the stray capacitance C_p. The amplifier was thermally anchored to the still plate of the dilution fridge by a copper link. The power dissipated by HBT was estimated to be around 100 μW for the relevant operating range. The output of the HBT amplifier is connected to the commercial low-noise amplifier located at the 4-K plate via a superconducting NbTi coaxial cable. The two-stage amplifier provided a total voltage gain of the order 100.

4.3.2 Results

In this section, we present our results of the image-charge measurements for SSE confined in the microchannel array and provide some qualitative analysis of the data.

Similar to the experiment described in Section 4.2, the resonant transition $(1 \rightarrow 2)$ is excited by adjusting the applied voltage V_{b} to match the transition frequency ω_{21} of SSE

and the MW frequency ω_{mw} via the Stark shift. Here V_{b} is the voltage applied to both channel and reservoir electrodes, that is $V_{\mathrm{LR/RR}} = V_{\mathrm{ch}} \equiv V_{\mathrm{b}}$, see Fig. 4.8. The measured voltage signals proportional to the image-charge current at the channel electrode are shown in Fig. 4.10(a). Here the resonance peak recorded for different MW frequencies ω_{mw} corresponds to the resonance Rydberg transition of SSE. The resonance value of V_{b} as a function of the MW frequency $\omega_{\mathrm{mw}}/2\pi$ is shown in Fig. 4.10(b) (the orange open circles). To compare this result with the theoretically predicted Stark shift of SSE, we numerically solved the time-independent Schrödinger equation for different values of $E_{\perp}$ (see Section 1.2.2), to find the relation between the transition frequency ω_{21} and $E_{\perp}$. The result is shown by the blue solid line. Comparison between the experimental data and theoretical calculation in Fig. 4.10(b) provides us with an empirical relation between $E_{\perp}$ and V_{b} in the form $E_{\perp} = kV_{\mathrm{b}} + E_{\perp}^{(0)}$, with $k \sim 600$ cm^{-1}.

The amplitude of the resonance peak depends on the MW power. According to a simple two-level model, the fractional occupancy ρ_{22} of the first excited Rydberg state is expected to increase linearly with the MW power for small powers and saturate at 50% for very high power. Fig. 4.10(c) shows the dependence of the signal amplitude on MW power given as a percentage of P_0, where P_0 is the maximum power of our MW source before the attenuator. As expected, the peak amplitude increase with increasing power. The power dependence is almost linear, which indicates that the excited state population is far from the saturation.

In addition, Fig. 4.10(a) indicates that the peak amplitude varies with MW frequencies at fixed settings of the attenuator. Note that the power output of our MW source depends on its frequency. Fig. 4.10(d) represents the output MW power measured at the output of our MW source. The color arrows represent the corresponding frequencies used to obtain the data in Fig. 4.10(a). Although the minima in the power spectrum do not exactly match the frequencies corresponding to the minimal voltage amplitude in Fig. 4.10(a), it is reasonable to suggest that the total power loss through the overmoded waveguide might also depend on the MW frequency.
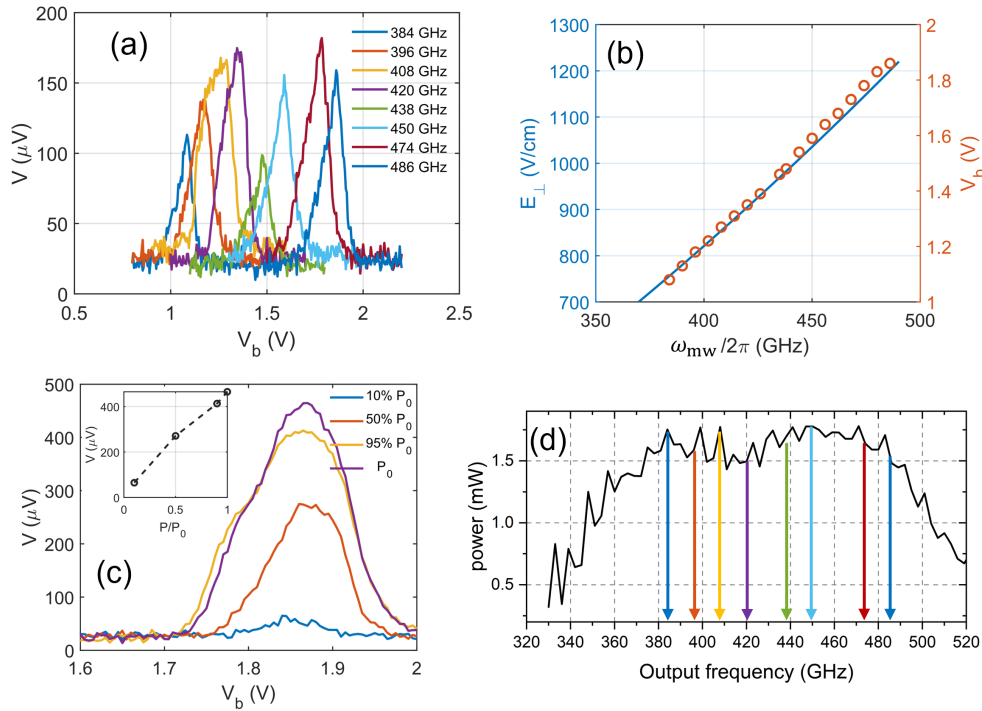
Figure 4.10: (a) Experimental traces of the image-charge signal versus the biasing voltage V_b for different MW frequencies. (b) Plot of the holding electric field (the left axis) and applied voltage V_b (the right axis) at resonance versus the transition frequency. Solid line is the result of the theoretical calculations, while the open circles represent the position of the measured resonance peaks in (a). (c) Experimental traces of the image-charge signal measured at $\omega_{mw}/2\pi = 480$ GHz for different MW powers, P_0 is the maximum power of our source. Inset: The voltage signal at the peak of the resonance vs MW power. (d) The output power of the MW radiation as a function of frequency measured by a room temperature power meter. The color arrows represent the corresponding frequencies used in (a).

Instead of tuning the transition frequency of SSE via adjusting the biasing voltage V_b, one can also vary the input MW frequency to match the transition frequency ω_{21} at a fixed applied voltage V_b. This method is not frequently used in the conventional absorption measurements because the MW power of the source depends on its frequency, see Fig. 4.10(d). Nevertheless, it is convenient to use this method in our experiment with SSE in the microchannel device. Unlike in a parallel-plate capacitor setup with the liquid level set at the middle between two plates, see Eq.(2.2), in the microchannel

device the pressing field $E_\perp$ strongly depends on the image charges induced by SSE in the bottom electrodes. Varying V_b unavoidably changes the SSE density profile across the channel, therefore the pressing field, leading to an unexpected shift and broadening of the lineshape. The typical results of frequency sweep measurements taking from two different experimental runs are shown in Fig. 4.11(a, c), while the corresponding $E_\perp$ vs V_b dependencies obtained form these data are given in Fig. 4.11(b, d). In both cases we find that the proportionality coefficient between $E_\perp$ and V_b is about $\sim 600\,\text{cm}^{-1}$, which is consistent with data shown in Fig. 4.10(b).
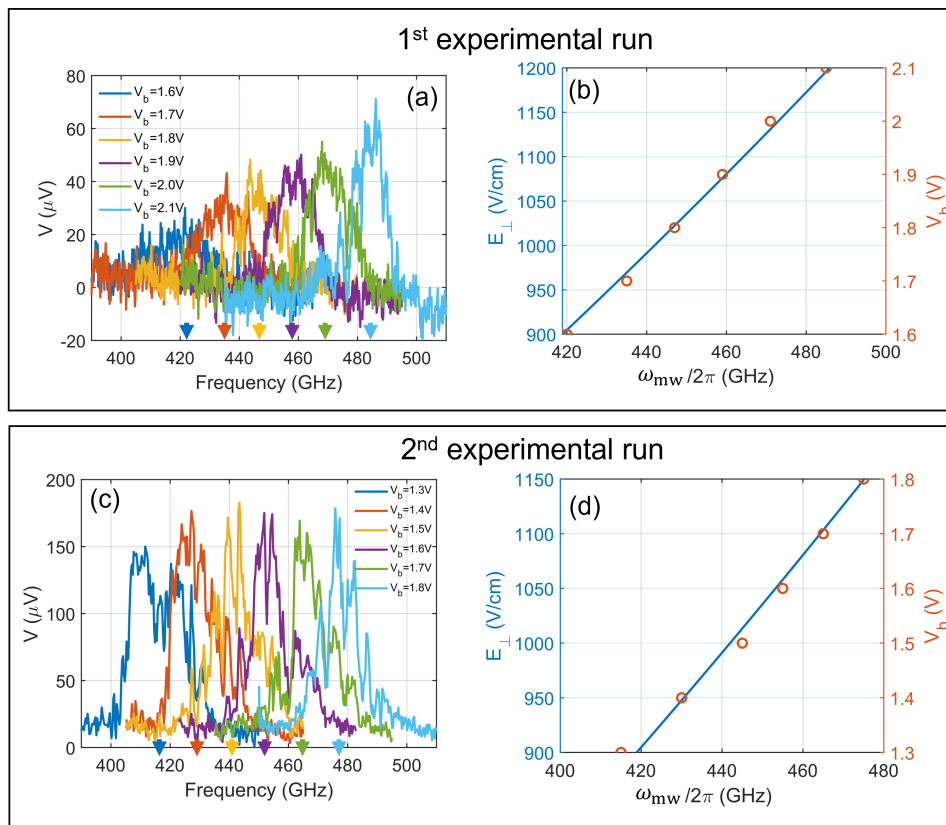
Figure 4.11: (a, c) Experimental traces of the image-charge signal versus MW frequency for different biasing voltage V_b. (b, d) Plot of the holding electric field (the left axis) and applied voltage V_b (the right axis) at resonance versus the transition frequency. Solid line is the result of the theoretical calculations, while the open circles represent the measured resonance peaks by the frequency sweeping. The color arrows represents the corresponding frequency used in (a) and (c).

4.3.3 Discussion

Here, we try to analyze the linear dependence $E_\perp = kV_b + E_\perp^{(0)}$ in terms of the analytical expression for the pressing field given by Eq. (2.5). It should be noted that in this multichannel setup we vary all the three bottom electrode voltages, V_{LR}, V_{RR} and V_{ch} simultaneously. Therefore, the potential of SSE V_e is not a fixed value but depends on the applied voltage $V_b = V_{LR} = V_{RR} = V_{ch}$. As discussed in Section 2.4.1, the potential of the uncharged surface of liquid helium in the channel can be estimated as $V_u = c_1 V_b + c_2 V_t$, where we have $c_1 = 0.8$, $c_2 = 0.2$ and $V_t = 0$. It is reasonable to assume that $V_e = V_u + \Delta V_e = c_1 V_b + \Delta V_e$, where ΔV_e is the potential difference between the charged and uncharged surface of liquid helium in the channel, and which varies for different experimental runs depending on the total number of SSE in the device. Using this relation, Eq. (2.5) can be written as

$$E_\perp = \frac{V_b}{2d} - \frac{V_e}{d}\left(1 - \frac{1}{2c_1}\right) = \frac{1 - c_1}{d} V_b + \Delta V_e, \tag{4.3}$$

For $d = 4\,\mu\text{m}$, the slop of $E_\perp$ vs V_b is $(1 - c_1)/d = 500\,\text{cm}^{-1}$, which is slightly smaller than the experimentally measured value $600\,\text{cm}^{-1}$. In order to account for the discrepancy, we can use the same argument as in Section 4.2, that is assuming that the real helium level is slightly lower than the channel depth due to the surface curvature. Then, for $k = 600\,\text{cm}^{-1}$, we estimate the liquid depth to be $d = 3.33\,\mu\text{m}$.

The experimental results presented in this section demonstrate high-level control and tunability of SSE in a device comprised of an array of microchanels. The Rydberg energy spectrum of SSE in such a device is well described by simple electrostatics, giving a very good agreement with the measured image-charge spectra. This presents SSE confined in microchannels as a promising platform for further work towards quantum-state detection and qubit implementation with electrons on helium.

4.4 Summary

In this chapter, we reviewed three different methods for detecting the Rydberg transition in SSE. It turns out that the image-charge method provides the most direct way for Rydberg states detection. The present sensitivity of this method required us to use a multichannel device to increase the number of SSE in the device. In order to apply this method for SSE in a single channel device, as well as achieve the single electron detection, it is required to improve SNR of our measurement circuits. In the next and final chapter, we describe our strategy on improving the measurement sensitivity by employing a high quality factor RLC resonating circuit. We also show some preliminary results of an experiment where we detect the Rydberg transition in SSE on the bulk liquid helium using this method.

Chapter 5

Helical resonator for the image-charge detection

The detection of a small number of charged particles is a recurring problem in the physical science. In many systems, such as the trapped ions and electrons in the semiconductor quantum dots, the charged particles are detected via a small current signal using a high quality factor radio-frequency (RF) RLC resonator [100–102]. Various theoretical and empirical methods have been developed for designing and fabricating a high quality factor resonator at a desired frequency for a given set of experimental constrains [103–107].

In the past few decades, the helical RLC resonators have been proved to be a powerful tool for high precision detection of the image-current of ions in Penning traps [108–110]. Motivated by this work, we are trying to employ the helical resonators for the image-charge detection of the Rydberg transition in SSE. One can expect that the signal-to-noise ratio of a measured signal can be significantly improved, which is important for the ultimate goal of building an image-charge readout setup for a single electron. This chapter is organized as follows. In Section 5.1, we review the basics of a resonant circuit and the two-port transmission measurements in the framework of the lumped circuit model. In Section 5.2, we discuss an analytical model of our helical resonator and present the preliminary experimental results of the application of a helical resonator for the image-charge detection

of the Rydberg transition in SSE on the bulk helium. Finally, in Section 5.3 we discuss the further optimization of a helical resonator in order to reach a higher quality factor.

5.1 Theory of a resonant circuit

5.1.1 Introduction to a RLC resonator

Let us start with some basic characteristics of the series and parallel RLC resonant circuits. Since the circuit operates at radio frequencies, for which the circuit dimensions are small relative to the wavelength, it can be treated by a lumped-circuit model. As shown in Fig. 5.1, the RLC resonator can be modeled by either series (a) or parallel circuit (b). The input impedance for each circuit is given by
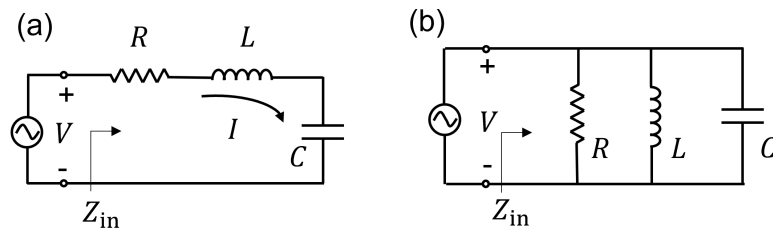
Figure 5.1: The lumped circuit model of the series (a) and parallel (b) RLC circuit.

$$Z_{\text{in}} = R + j\omega L + \frac{1}{j\omega C}, \qquad \text{for RLC in series,} \qquad (5.1)$$

$$Z_{\text{in}} = \left(\frac{1}{R} + j\omega C + \frac{1}{j\omega L} \right)^{-1}, \qquad \text{for RLC in parallel.} \qquad (5.2)$$

At a resonance frequency $\omega_0 = 1/\sqrt{LC}$, the capacitive reactance $1/j\omega_0 C$ and inductive reactance $j\omega_0 L$ cancels each other, such that the absolute value of the impedance of the circuit has an extreme value. We define the ω_0 as the resonance frequency. Fig. 5.2 represents the variation of the absolute value of the circuit impedance as a function of the frequency for series (a) and parallel (b) RLC circuit. It is clear that at $\omega = \omega_0$ the system has a minimum and maximum value of $|Z_{\text{in}}|$, respectively. Note that at the resonance
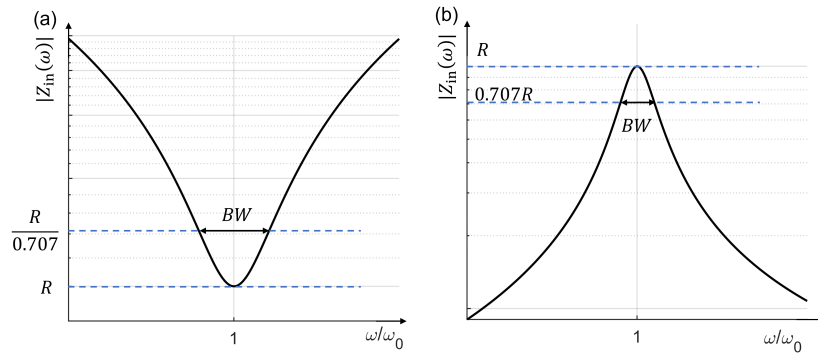
Figure 5.2: The magnitude of the input impedance versus frequency for RLC series circuit (a) and parallel circuit (b).

frequency the circuit impedance is real and equal to R.

Alternatively, the resonance frequency can be defined by the balance of the electric and magnetic energy stored in the circuit. Consider the energy delivered to each lumped element, with the magnetic energy W_m stored in the inductor L and the electric energy W_e stored in the capacitor C

$$W_m = \frac{1}{4}|I|^2 L, \; W_e = \frac{1}{4}|I|^2 \frac{1}{\omega^2 C}, \qquad \text{for series circuits,} \qquad (5.3)$$

$$W_m = \frac{1}{4}|V|^2 \frac{1}{\omega^2 L}, \; W_e = \frac{1}{4}|V|^2 C, \qquad \text{for parallel circuits.} \qquad (5.4)$$

Here, all of the components in a series connection carry the same current I, while the same voltage V is applied to all circuit components connected in parallel. From (5.3) and (5.4), it is clear that at the frequency $\omega_0 = 1/\sqrt{LC}$ the stored magnetic energy is equal to the stored electric energy in both cases, that is $W_m = W_e$. Additionally, the power dissipation P_{loss} at the series and parallel resistor R is given by

$$P_{\text{loss}} = \frac{1}{2}|I|^2 R, \quad \text{and} \quad P_{\text{loss}} = \frac{|V|^2}{2R}, \qquad (5.5)$$

respectively.

Quality factor Q

In addition to the resonance frequency, the *quality factor Q* is another important quantity describing the RLC resonant circuit. It is defined as the ratio of the total electromagnetic energy stored in the capacitor and the inductor to the power dissipation at the resistor at the resonance

$$Q = \omega_0 \frac{W_m + W_e}{P_{\text{loss}}} = \begin{cases} \omega_0 L/R = 1/\omega_0 RC, & \text{for series circuits,} \\ R/\omega_0 L = \omega_0 RC, & \text{for parallel circuits.} \end{cases} \tag{5.6}$$

The Q-factor characterises the loss of the resonance circuit, the higher Q implies lower power loss. In practice, the resonator is always coupled to some external circuitry, for example, the transmission line. This external circuitry can be considered as a load to the resonator circuit. We consider the simplest case for which the external load is a resistor R_L. If the resonator is a series RLC circuit, the load R_L adds in series with resonator resistance R, so the total resistance is $R_L + R$. According to the definition of Q-factor given by Eq. (5.6), the loaded quality Q_L for the whole system can be written as $Q_L = \omega_0 L/R_{\text{tot}}$. We define $Q_0 = \omega_0 L/R$ as the unloaded quality factor, which characterises the resonator's Q-factor in the absence of any load. In addition, we define $Q_E = \omega_0 L/R_L$ as the external quality factor accounting for the power loss at the load. Then, Q_L can be expressed as

$$\frac{1}{Q_L} = \frac{1}{Q_E} + \frac{1}{Q_0} = \frac{1}{Q_0}(1 + g), \tag{5.7}$$

where $g = Q_0/Q_e$ is the coupling constant, which characterizes the level of the coupling between the resonator and the load. The coupling constant can be tuned depending on the application. For example, to maintain a high Q value of the measurement circuit, the helical resonator should be weakly coupled to its load, with $g \ll 1$. On the other hand, in order to achieve the maximum power transfer to the resonant circuit through the external circuitry, the resonator should be optimally coupled to the load, with $g \simeq 1$. Eq. (5.7)

also applies to the parallel circuit.

Finally, we define the half-power bandwidth (BW) of the unloaded resonator, see dashed blue lines in Fig. 5.2(a, b). For the series circuit, one can rewrite $Z_{\rm in}$ in terms of the frequency ω and Q-factor, as

$$Z_{\rm in} = R + j\omega L \left(1 - \frac{1}{\omega^2 LC}\right) = R + j\omega L \left(\frac{\omega^2 - \omega_0^2}{\omega^2}\right) \simeq R + j\frac{2RQ_0\Delta\omega}{\omega_0}, \qquad (5.8)$$

where $\Delta\omega = |\omega - \omega_0|$. Note that the complex power delivered to the resonator is given by $P = \frac{1}{2}Z_{\rm in}|I|^2 = \frac{1}{2}\frac{V^2}{|Z_{\rm in}|^2}Z_{\rm in}$ and the average power $\overline{P}$ dissipated in the resonator is given by the real part of P, that is

$$\overline{P} = \frac{1}{2}\frac{V^2}{|Z_{\rm in}|^2}R = \frac{1}{2}\frac{V^2 R}{R^2 + (2RQ_0\Delta\omega/\omega_0)^2}. \qquad (5.9)$$

It is clear that at the resonance $\overline{P}$ reaches its maximum value with $\overline{P}_{\rm max} = |V|^2/2R$ and half power condition $\overline{P} = \overline{P}_{\rm max}/2$ corresponds to $|Z_{\rm in}|^2 = 2R^2$, that is $Q_0 = 2\omega_0/\Delta\omega$. If we define the bandwidth as $BW = 2(\Delta\omega/\omega_0)$, then we have $BW = 1/Q_0$. Similarly, we can get the same relation for a parallel circuit.

5.1.2 Determining unloaded Q from the two-port measurements

For practical measurements, a resonator must be coupled to the external circuitry, which makes it impossible to directly measure the unloaded Q_0 of the resonator. Practically, we first measure the loaded quality factor Q_L and then find Q_0 using the relation given by Eq. (5.7), assuming all parameters of the external circuit are known. Now, we will show how to find the unloaded Q_0 from the conventional two-port shunt measurements using a network analyzer. Fig. 5.3(a) shows a parallel RLC resonator (blue shaded area) connected to the network analyzer with the characteristic impedance $R_L = 50\,\Omega$ via two coupling capacitors C_κ (gray shaded area). In such a setup we measure the transmission coefficient S_{21}, which is defined as the ratio between the voltage amplitude of the transmitted signal

measured at port 2 and the driving voltage amplitude applied to the port 1.
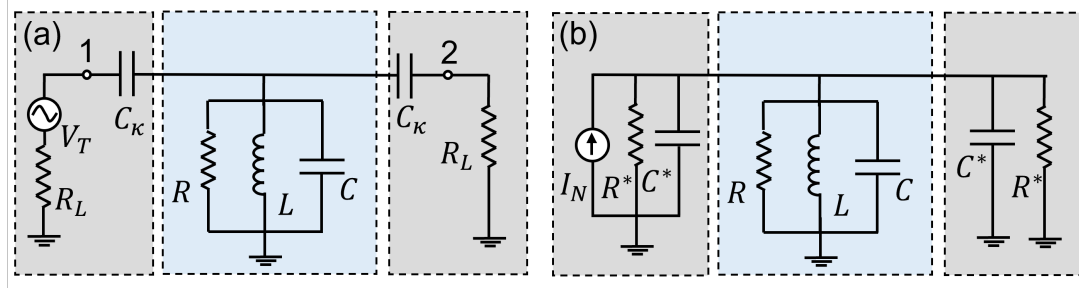
Figure 5.3: (a) Illustration of two-port shunt measurement. (b) Norton's equivalent circuit after series to parallel impedance transformation, as described in the text.

In order to understand the effect of the series capacitors C_κ, it is convenient to transform the gray shaded circuit to its Norton equivalent circuit with all components connected in parallel, see Fig. 5.3(b). The parallel and series circuits are equivalent when the output impedance $R_L + \frac{1}{j\omega C_\kappa} = (1/R^* + j\omega C^*)^{-1}$, thus R^* and C^* is given by

$$R^* = \frac{1 + \omega^2 C_\kappa^2 R_L^2}{\omega^2 C_\kappa^2 R_L}, \ C^* = \frac{C_\kappa}{1 + \omega^2 C_\kappa^2 R_L^2}. \tag{5.10}$$

Since all the elements are arranged in parallel, the total resistance and capacitance can be written as

$$R_{\text{tot}} = (2/R^* + 1/R)^{-1}, \ C_{\text{tot}} = C + 2C^*, \tag{5.11}$$

and the resonance frequency is shifted to a new value

$$\omega_0^* = \frac{1}{\sqrt{L(C + 2C^*)}}. \tag{5.12}$$

In order to make the shifted resonance frequency close to the intrinsic frequency of the resonator, one needs to choose a weak coupling, that is $C^* \ll C$. Then, the $50\,\Omega$ load resistance R_L is transformed into a very large parallel resistance R^*. Furthermore, we can

write

$$Q_L = \omega_0^* \frac{C + 2C^*}{1/R + 2/R^*} \simeq \omega_0 \frac{C}{1/R + 2/R^*}, \tag{5.13}$$

$$Q_0 = \frac{R}{\omega_0 L}, \quad Q_E = \frac{R^*}{2\omega_0 L} \quad \text{and} \quad g = \frac{Q_0}{Q_E} = 2R/R^*. \tag{5.14}$$

The loaded quality factor Q_L can be determined from the half-power bandwidth of the measured transmission coefficient S_{21}, with $Q_L = f_0/(f_2 - f_1)$, where $f_0 = \omega_0/2\pi$, f_1 and f_2 represents the frequencies at the half-power at each side of the resonance. In practice, $f_2 - f_1$ corresponds to either the $-3\,\mathrm{dB}$ bandwidth, if S_{21} is in decibels, or the 0.707 bandwidth, if S_{21} is in the voltage ratio. Note that S_{21} should be a real number at resonance and it is related to the coupling factor g by the relation

$$g = \frac{S_{21}(\omega_0)}{1 - S_{21}(\omega_0)}. \tag{5.15}$$

Note that in this expression S_{21} is in the voltage ratio. Then, one can obtain the unloaded Q-factor using the relation $Q_0 = Q_L/(1 + g)$. For practical purposes, it is convenient to use strong undercoupling, $g \ll 1$, then $Q_0 \simeq Q_L$.

5.2 Helical resonator

The helical resonator setup with high quality factor is frequently used for the non-destructive measurements of image-current induced by the trapped ions. First, we briefly review the basic measurement setup in trapped-ion systems. The equivalent circuit of the detection setup using a helical resonator is shown in Fig. 5.4, where the helical resonator is represented as a RLC parallel circuit and the image-current signal I_{ima} induced by the trapped ions is represented as a current source. The current source is coupled to the resonator shunted to the ground and the voltage drop across the resonator is given by $V = Z I_{\mathrm{ima}}$, where Z is the impedance of the resonator. As shown in Fig. 5.2(b), for a par-
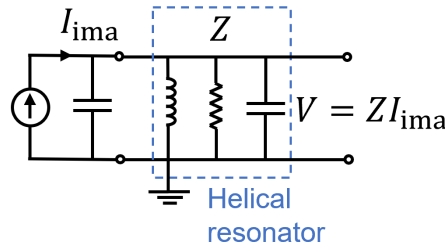
Figure 5.4: Equivalent circuit of the helical resonator coupled to an external image-current source, as described in the text.

allel RLC resonator the impedance Z has the maximum value at the resonance frequency, with $Z_{\max} = R$. Clearly, one can get the maximum voltage drop across the resonator $V_{\max} = RI_{\mathrm{ima}}$ for a given image current I_{ima}. In addition, a high quality factor is desired in this setup. According to Eq. (5.6), the resistance R of the resonator is proportional to the quality factor Q. As a result, the voltage drop can be further increased by improving the quality factor of the resonator. In the following, we adapted this techniques into our experimental setup for the image-charge detection discussed in Chapter 4.

We start from discussing the geometry of the helical resonator. The helical RLC resonator consists of a solenoidal coil mounted in the center of a cylindrical metal shield. In our experiment, the coil is a single layer of conducting wire (Cu or NbTi) wound on a insulation core [Polytetrafluoroethylene (PTFE)] with the winding pitch equal to the wire diameter. After the winding, one end of the coil is grounded to the shield and the other end is left as an open-circuit, which in experiment is coupled to the measurement circuit. Fig. 5.5(a) shows a photograph of an unassembled high-Q helical resonator made from the superconducting material, while Fig. 5.5(b) is a sketch of the assembled resonator. For convenience, we list the symbols describing the geometric parameters of the resonator in Table. 5.1. The first version of the resonator used for the image-charge detection experiment is slightly different from the one shown in Fig. 5.5(a). In the first version, the outer shield is made from a thin Cu foil with the thickness of 0.5 mm. The foil is rolled into a cylinder with the inner diameter $d_s = 45$ mm and height $l_s = 100$ mm. The two edges were soldered by tin. For the inner core, the copper wire with diameter $160\,\mu$m was
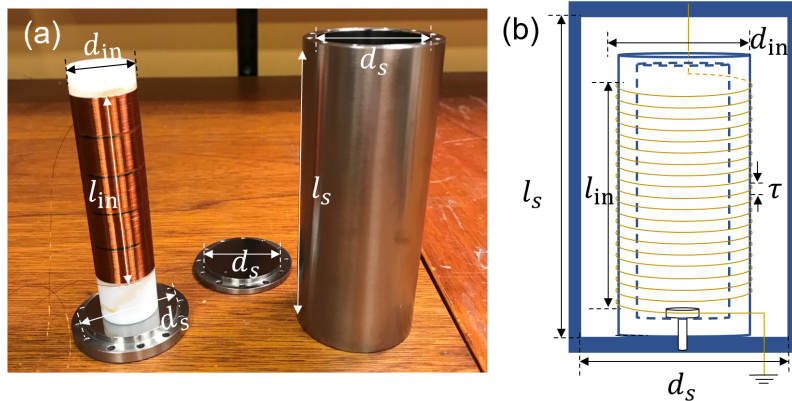
Figure 5.5: (a) Photograph of an unassembled superconducting resonator. Left: NbTi coil wound tightly on a PTFE tube (white color) with diameter $d_{in} = 23$ mm and total length = 100 mm. The winding pitch τ is equal to the wire diameter. Right: The outer metal shield (silver color) is made from NbTi, and has the inner diameter of $d_s = 38$ mm and inner height of $l_s = 110$ nm. Two lids (silver color) with inner diameter d_s are used to close the shield from both sides. (b) Sketch of the assembled resonator. The outer shield is shaded in dark blue color, while the coil is in yellow color.

tightly winded on the PTFE tube with $d_{in} = 23$ mm and $l_{in} = 6.3$ mm and tied up by the PTFE thread seal tape to ensure the mechanical stability, as well as the thermal contact with the insulation core.

d_s	inner length of the metal shield
l_s	inner diameter of the metal shield
l_{in}	length of the winding part
d_{in}	outer diameter of the insulation core
τ	winding pitch

Table 5.1: List of symbols for the geometric parameters of the helical resonator shown in Fig. 5.5.

Next, we discuss the RF properties of the resonator. The simplest estimation of the resonance frequency can be done by considering the coil inductance and capacitance between the coil and shield. The coil inductance can be simply estimated assuming an unshielded coil, while the coil capacitance can be evaluated as the capacitance of a coaxial

structure, according to

$$L = \frac{\mu_0 N^2 \pi (d_{\text{in}}/2)^2}{l_{\text{in}}}, \quad \text{[SI]} \tag{5.16}$$

$$C = \frac{2\pi \epsilon_0 l_{\text{in}}}{\ln (d_s/d_{\text{in}})}. \quad \text{[SI]} \tag{5.17}$$

For the first version of the resonator, with $d_{\text{in}} = 23$ mm, $d_s = 45$ mm and $l_{\text{in}} = 6.3$ mm, we obtain $L = 1.68$ mH, $C = 6.98$ pF and the resonance frequency $f_0 = 1.4703$ MHz. In addition, one has to consider the contribution to the total capacitance of the resonator from the capacitance between wire turns in the coil. Moreover, for sufficiently high frequencies ~ 1 MHz, the skin and proximity effects cause the winding resistance to increase and the inductance to decrease. Thus, one needs a more accurate estimation.

The first accurate study of the high frequency RF properties of shielded helical coil resonators was done by Macalpine *et al.* [105], who took the skin effect and dielectric losses into account and gave an empirical estimation of the values of inductance and capacitance. Later, these expressions were derived using the distributed element model [103–107, 111]. Fig. 5.6(a) shows the equivalent distributed element circuit of a helical resonator applicable for sufficiently high frequencies. Here, R_i and L_i represent the resistance and inductance of each wire turn, C_t and C_s represent turn-to-turn and turn-to-shield capacitance, respectively. All these parameters are strongly dependent on the resonator's geometric parameters. It is rather time-consuming to predict the electrical properties of a resonator using the distributed element model. For the sake of a quick estimation, it is instructive to further simplify this model to an equivalent lumped parameter circuit. As shown in the upper panel of Fig. 5.6(b), the resonator inductance, resistance and capacitance are represented as lumped parameters L, R and C, respectively. The conversion relation between the lumped and distributed elements can be found in Ref. [107, 111]. Note that the resistance R is called residual resistance, which is a series resistance consisting of the resistance of the shield, the coil resistance, as well as the resistance representing the dielectric losses. The capacitance C includes both turn-to-turn and turn-to-shield ca-
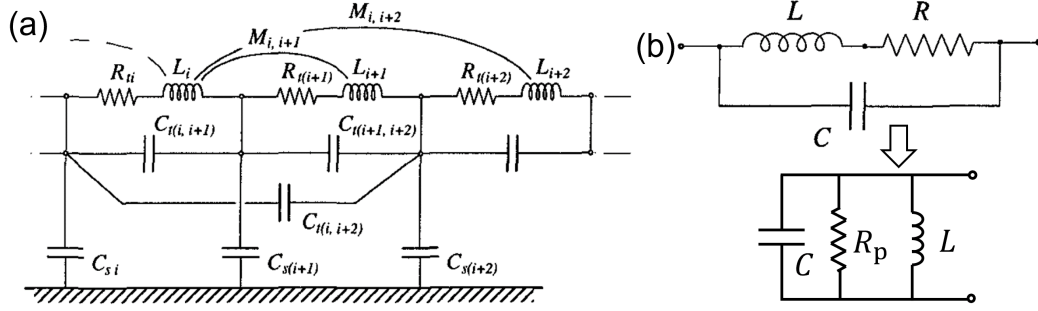
Figure 5.6: (a) Equivalent distributed element circuit of the helical resonator. Here, R_i and L_i represents the resistance and inductance of each turn, C_t and C_s represent turn-to-turn and turn-to-shield capacitance, respectively. (b) Top: the simplified lumped circuit model. The coil inductance, resistance and capacitance are depicted as lumped parameters L, R and C respectively. Bottom: the equivalent parallel circuit. Typically, C and L is almost unchanged after the series to parallel conversion, while the R_p arises significantly. The figure is taken from [107].

pacitance. The circuit can be further simplified by the series to parallel conversion. The bottom panel in Fig. 5.6(b) represents the equivalent parallel circuit. Typically, C and L are almost unchanged after the conversion, while the R_p changes significantly since it is inversely proportional to the residual resistance R. In particular, the parallel inductance L is given by the expression [105, 111]:

$$L = \frac{\pi\mu_0 N^2 (d_\mathrm{in}/2)^2}{l_\mathrm{in} + 0.9(d_\mathrm{in}/2)} \cdot \left(1 - \frac{b}{b + 1.55}\frac{d_\mathrm{in}^2}{d_\mathrm{s}^2}\right), \text{ where } b = \frac{2l_\mathrm{in}}{d_\mathrm{s} - d_\mathrm{in}}. \quad [\text{SI}] \quad (5.18)$$

For the first version of our resonator, that is $d_\mathrm{in} = 23$ mm, $d_s = 45$ mm and $l_\mathrm{in} = 6.3$ mm, we obtain $L = 0.996$ mH. Using the estimated value of L, we can obtain the values of other parameters by the transmission measurements. Using the standard two-port measurements discussed in Section 5.1.2, we obtain the resonance frequency $f_0 = 1.45$ MHz and the quality factor $Q_L = 63.4$, thus we have $C \simeq 10$ pF and $R \simeq 138\,\Omega$ (the equivalent parallel resistance R_p in Fig. 5.6(b) is $0.57\,\mathrm{M\Omega}$). Here, the coupling capacitance is chosen to be $C_\kappa = 1$ pF and $R_L = 50\,\Omega$ (with $C^* = 1\,\mathrm{pF}$ and $R^* = 241\,\mathrm{M\Omega}$ at $f_0 = 1.45$ MHz). It is clear that the resonator is weakly coupled (undercoupled) to the

load since $g = R_{\mathrm{p}}/R^* \ll 1$, thus we have $Q_0 \simeq Q_L = 63.4$.

Comparing to the simple relation given by Eq. (5.16), the inductance is reduced about 40% due to the shielding, whereas the total capacitance is also increased because we took the turn-to-turn capacitance into account. The measured frequency is still very close the value estimated by the simple model given by Eq. (5.16) and (5.17).

5.2.1 Coupling a helical resonator to the measurement circuit

Once the resonator was prepared and characterized using the transmission measurements, we incorporated it with our experimental setup. In order to achieve a larger image-charge signal, we conducted the first experiment with a large number of electrons ($\sim 10^8$) on the bulk liquid helium using the parallel-plate capacitor, see Section 2.2.1.

The photograph of the experimental setup is shown in Fig. 5.7(a), while its equivalent circuit is given in Fig. 5.7(b). The resonator is mounted on the still plate of the dilution
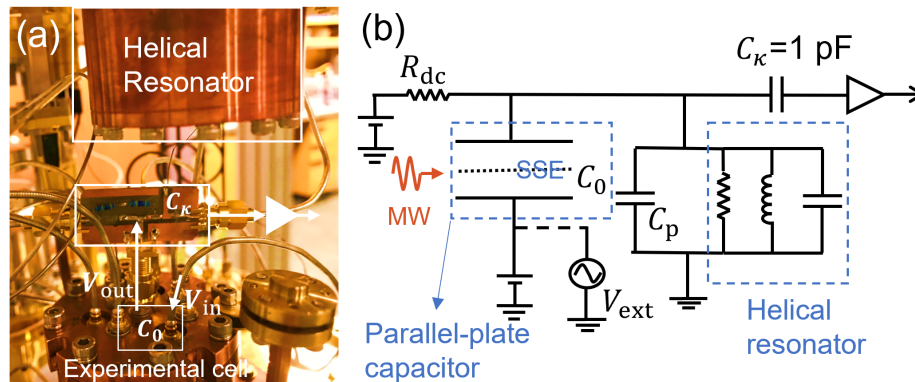
Figure 5.7: (a) The photograph of the measurement setup. The top center electrode of the Corbino disk device is connected to PCB, which provides DC bias and coupling to the resonator. The resonator is brought to a close proximity with PCB to reduce the stray capacitance of the unshielded wire. (b) The equivalent circuit of the experimental setup. For the test transmission measurements, the bottom plate of the parallel-plate capacitor is driven by an external voltage source V_{ext}.

refrigerator and the experimental cell is mounted on the mixing chamber plate. The resonator is connected to the top center electrode of the parallel-plate capacitor. Here,

C_p represents a parasitic capacitance of the wiring connecting the cell to the resonator. Note that, C_p is typically in the order of a few pF, which is comparable to the resonator capacitance. Therefore, the resonance frequency is shifted to a lower value.

To characterize the resonator, we perform a test transmission measurement, as described earlier. As shown in Fig. 5.7(b), we drive the bottom plate of the parallel-plate capacitor and measure the transmitted signal amplified by a cascode two-stage amplifier with the voltage gain about 28 at room temperature. Note that, the capacitance between the bottom and top capacitor plates is around $C_0 = 1$ pF, similar to the coupling capacitance C_κ. The measured transmission coefficient S_{21} is given by the solid blue line in Fig. 5.8. As expected, the center frequency is shifted to the lower frequency $f_0 = 1.199$ MHz, from which we estimate $C_p \simeq 5.6$ pF. The loaded quality factor is $Q_L = 61.2$ and the parallel resistance is $R_p = 0.46\,M\Omega$, similar to the previously measured values.
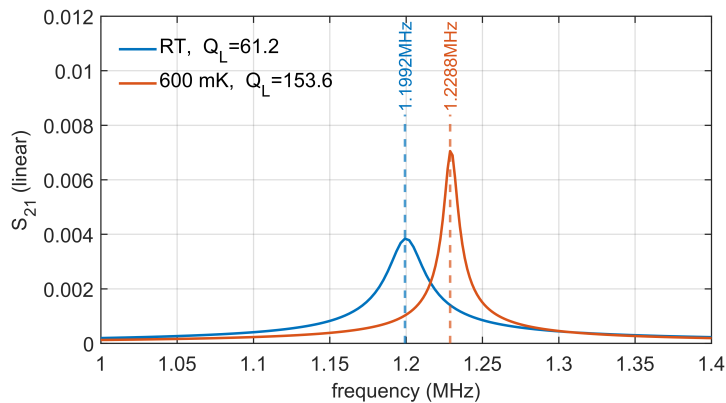
Figure 5.8: The S_{21} transmission spectrum of the experimental setup for different temperatures.

Next, we cool down the setup in the dilution refrigerator and repeat the same transmission measurements at a low temperature. The result is given by the solid orange line in Fig. 5.8. The quality factor is improved after cooling down, with $Q_L = 153.6$ at 600 mK, corresponding to the parallel resistance $R_p = 1.19\,M\Omega$. The center frequency is also slightly shifted from 1.199 MHz to 1.229 MHz because of the change of C_p after cooling

down. It should be noted that, because the cascode amplifier has the input impedance of $R_{\mathrm{in}} = 1\,\mathrm{M}\Omega$, the amplifier's voltage gain is reduced to 19 due to the effect of a voltage divider between R_{in} and R_{p}.

5.2.2 Image-charge detection using the helical resonator

In this section, we present the preliminary results of the image-charge detection of the Rydberg transition in SSE on the bulk liquid helium using the helical resonator setup. In the experiment, the parallel-plate capacitor is half-filled with liquid ^{3}He and the liquid
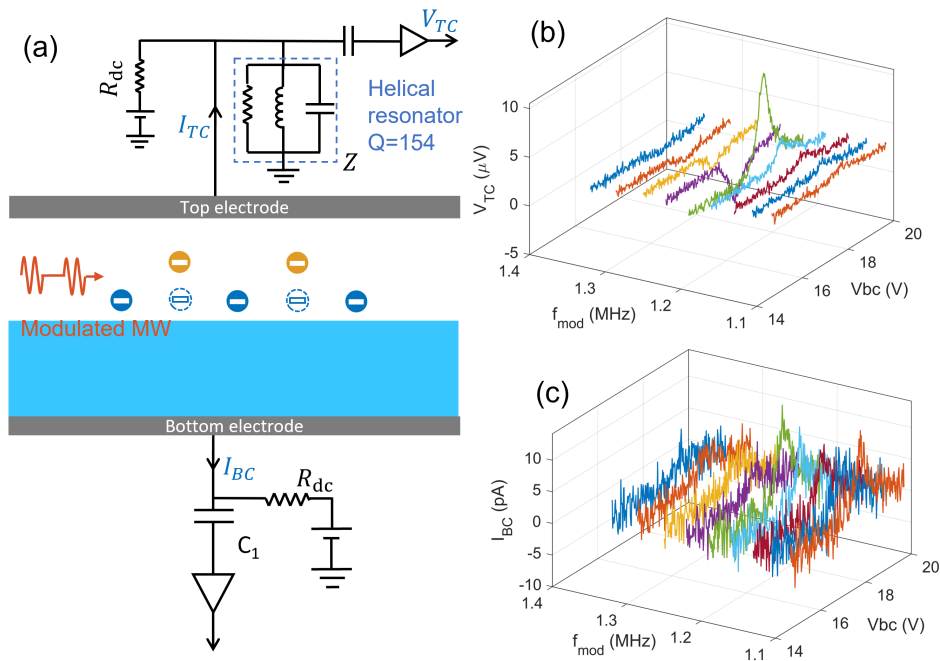
Figure 5.9: Improvement of the image charge signal by using the helical resonator. (a) Schematic of the experimental setup. (b) Image-current signal measured at the top plate versus MW modulation frequency and DC bias applied to the bottom capacitor plate (V_{bc}). When the modulation frequency matches the resonant frequency of the resonator with $f_0 = 1.23$ MHz, the image-current signal presents the highest SNR. (c) For the sake of comparison, the image charge signal measured directly at the bottom plate without using the helical resonator is shown. Comparison with panel (b) demonstrates an improvement of SNR of the image-charge detection setup.

surface is charged with SSE. Pulse-modulated MW radiation at a fixed frequency 130

GHz is transmitted into the cell and the Rydberg transition frequency ω_{12} is tuned in resonance by adjusting the DC voltage applied to the capacitor bottom electrode. The image-current signal induced by the excited SSE at the top plate produces a voltage drop at the RLC parallel resonator shunted to the ground and this voltage is amplified by the cascode amplifier. The voltage drop is given by ZI_{ima}, where I_{ima} is the image-current, see Eq. (4.2) and Z is the impedance of the RLC resonator. Since the resonator impedance Z is maximum at the frequency $f = f_0$, see Section 5.2, we tune the modulation frequency f_{mod} of the pulsed MW radiation to match the resonance frequency of the resonator. This produces the maximum output signal at $f_{\mathrm{mod}} = f_0 = 1.23$ MHz, as shown in Fig. 5.9(b). The improvement in the detection sensitivity is demonstrated by comparison with Fig. 5.9(c), where the image-current signal at the bottom plate is measured without the resonator.

5.3 Improving the quality factor of the helical resonator

In previous section, we have demonstrated that the helical resonator can improve SNR of the image-charge detection setup even for a relatively low quality factor of the resonator. In this section, we discuss the further optimization of the resonator's performance by improving its unloaded Q-factor. Table 5.2 summarizes the unloaded Q-value of the resonator for different optimization steps, where the step #0 represents the initial version of the resonator.

Optimization step	0	1	2	3
Q_0 at cryogenic temperature	151	800	1441	18692

Table 5.2: Unloaded Q-value of the resonator for different optimization steps. The details of the respective optimization steps are described in the text.

As mentioned in the previous section, the high quality factor corresponds to the low residual resistance which consists of three parts, the resistance of the shield, the coil resistance, as well as the resistance due to the dielectric losses. In the following, we aim

to reduce the effect of these three contributions.

In the first step, we use the same inner core which was used in the initial version of the resonator, while replace the outer shield with a copper cylinder housing having the inner diameter $d_s = 38$ mm and wall thickness of 5 mm. The housing is closed by two copper lids at both sides using 12 screws on each side to ensure the good electrical and thermal contact, see Fig. 5.5(a). The housing and lids are etched in acid and then cleaned with acetone in an ultrasonic bath to remove all oxidation and organics. Since the bulk material is used and cleaned up properly, the shield resistance is significantly decreased compared with the initial setup. As expected, we achieved a much higher quality factor $Q_0 = 800$.

In the second step, the inner coil is replaced by a superconducting wire with Cu plating, in order to reduce the coil resistance at low temperature below the superconducting transition. We found the unloaded quality factor increased to $Q_0 = 1441$.

In the last step, a pure superconducting material is used for both inner core and outer shield. This procedure aims to decrease the total residual resistance at the cryogenic temperatures. The inner coil is made from the $75\,\mu$m PTFE insulated NbTi wire of $50\,\mu$m conducting diameter, which is much thinner comparing to the initial copper wire coil. The outer shield is made from pure Nb, with the same geometric parameters used in earlier steps. In order to keep the same solenoid length l_{in}, we increased the number of winding turns to $N = 714$. With this, an effective inductance $L = 3.62$ mH was estimated. Fig. 5.10 shows the result of the transmission measurements. The resonant frequency is measured at $f_0 \simeq 1.379$ MHz and the parallel capacitance and resistance are calculated to be $C = 3.68$ pF and $R_{\mathrm{p}} = 585\,\mathrm{M}\Omega$. This resonator gives us the highest quality factor achieved so far, with $Q_0 = 18692$.

It is important to mention that the above transmission measurements were done in a strongly undercoupled regime, with the coupling capacitance $C_\kappa < 1$ fF. In actual experiments, it is very difficult to keep the small value of C_κ due to the coupling to the other parts of the measurement setup. For example, the coupling to the input impedance

of the amplifier as well as other low-impedance lines may limit the experimentally observed quality factors. Furthermore, the DC-biasing circuit at the top electrode contains a high-impedance metal film resistor R_{dc}, see Fig. 5.9(a). Thus, the total resistance $R_{tot} = R_{dc}||R_p$ is dominated by the smaller resistance. For a typical value of $R_{dc} = 100\,\text{M}\Omega$, the total resistance becomes $R_{tot} = 85\,\text{M}\Omega$, which dramatically decreases the loaded quality factor Q_L by 7 times, leading to a $Q_L = 2680$.
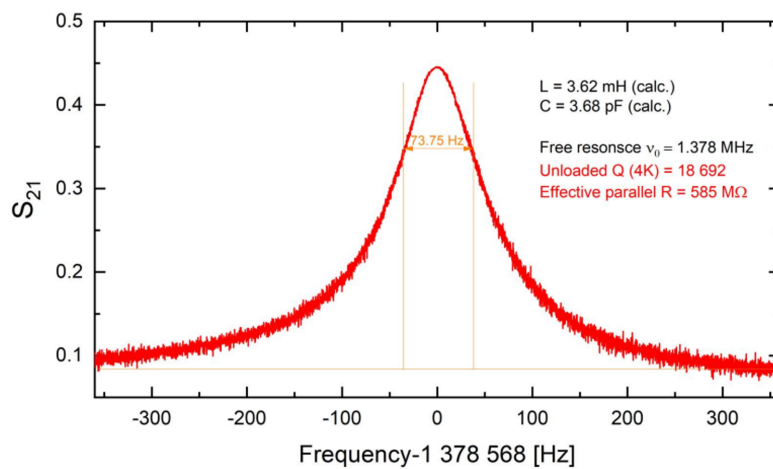
Figure 5.10: The S_{21} transmission spectrum of the superconducting resonator measured at 4.2 K.

5.4 Summary

We presented the preliminary results of our image-charge detection experiment using a parallel RLC helical resonator. It was shown that, even with a relatively low quality factor of the resonator, the measurement sensitivity significantly increases. With the ongoing optimization procedure for the quality factor, we could achieve up to 18692 of unloaded Q value. In general, a decrease of the measured Q_L because of the coupling to the lossy components in the measurement circuit is expected, therefore a further optimization of the detection circuit is required. In addition to the reduction of the losses in the detection circuit, one can try to improve the performance of the cryogenic amplifier by increasing

its effective input impedance.

Future plans and outlook

As was described in the introduction, successful implementation of the quantum-state detection and manipulation demands confinement and control of electrons at the level of a single particle. Such implementation requires a well-designed microstructured device. However, the present design of the microchannel setup have so far fallen below this goal. Our future works will focus on the following three points.

Single electron trapping

First and foremost, we need to enhance capabilities for charge manipulation in our experimental setup. A new design of the microchannel device incorporated with other submicron-scale single-electron traps is required. Fortunately, the trapping of the single electron has already been demonstrated by several groups using a single-electron transistor (SET) [6, 7, 89]. Moreover, employing a suitable microchannel geometry might provide some advantages for charge manipulation, as was already demonstrated by Rees *et al.* in experiments with a point contact device [16] and Lin *et al.* in a device with spatially periodic electrodes [112].

Single-electron Rydberg states detection

Second, for the purposes of high-precision readout of the single-electron Rydberg states, the coupling constant between an external RLC resonator with a higher quality factor and the experimental device must be carefully arranged. In addition, the device geometry and materials used for fabrication should be carefully considered in order to minimize the

dielectric loss and the stray capacitance.

Spin-states detection

So far, detection of the spin states of SSE on liquid helium is a challenging task. One potential solution is to couple the spin states to the Rydberg states, as discussed in Section 1.8.2, which can greatly facilitate the spin-state manipulation and detection. The microchannel devices are well suited for creating a sufficiently large gradient of an applied magnetic field to realize the coupling between the spin states and orbital states of SSE. For example, stripes of a ferromagnetic material, such as Cobalt or Permalloy, can be easily fabricated by evaporation and placed along the channels. Magnetization of the material in an applied uniform magnetic field would produce a nonuniform stray field outside the material, while the close proximity of the stripes to SSE confined in the microchannels can ensure that the field gradient experienced by SSE is sufficiently large. For example, our finite-element method (FEM) calculations show that 200-nm thick stripes of Cobalt placed at the bottom of a 4-μm deep channel filled with the superfluid helium would produce a gradient on the order 1 mT/μm near the liquid surface. This would result in the difference between the Zeeman splittings for the ground state and the first excited Rydberg state of SSE on the order 1 MHz. This is comparable to the intrinsic linewidth of the corresponding Rydberg transition at temperatures below 1 K [70]. Note that in the present setup the observed large broadening of the resonance is of orders of 10 GHz. This is due to inhomogeneous distribution of the pressing field in the microchannel. It seems to be feasible to significantly reduce this broadening by decreasing the width of the electron system in the channel. In particular, it has been already demonstrated that such width can be reduced to effectively a single electron across the channel [13, 113].

Bibliography

[1] P. M. Platzman and M. I. Dykman, *Quantum Computing with Electrons Floating on Liquid Helium*, Science **284**, 1967–1969 (1999).

[2] E. Kawakami, A. Elarabi, and D. Konstantinov, *Relaxation of the Excited Rydberg States of Surface Electrons on Liquid Helium*, Phys. Rev. Lett. **126**, 106802 (2021).

[3] S. A. Lyon, *Spin-based quantum computing using electrons on liquid helium*, Phys. Rev. A **74**, 052338 (2006).

[4] E. Kawakami, A. Elarabi, and D. Konstantinov, *Image-Charge Detection of the Rydberg States of Surface Electrons on Liquid Helium*, Phys. Rev. Lett. **123**, 086801 (2019).

[5] D. I. Schuster, A. Fragner, M. I. Dykman, S. A. Lyon, and R. J. Schoelkopf, *Proposal for Manipulating and Detecting Spin and Orbital States of Trapped Electrons on Helium Using Cavity Quantum Electrodynamics*, Phys. Rev. Lett. **105**, 040503 (2010).

[6] X. Zhou, G. Koolstra, X. Zhang, G. Yang, X. Han, B. Dizdar, X. Li, D. Ralu, W. Guo, K. W. Murch, D. I. Schuster, and D. Jin, *Single electrons on solid neon as a solid-state qubit platform*, Nature **605**, 46 (2022).

[7] G. Koolstra, G. Yang, and D. I. Schuster, *Coupling a single electron on superfluid helium to a superconducting resonator*, Nature Communications **10**, 5323 (2019).

[8] P. Glasson, V. Dotsenko, P. Fozooni, M. J. Lea, W. Bailey, G. Papageorgiou, S. E. Andresen, and A. Kristensen, *Observation of Dynamical Ordering in a Confined Wigner Crystal*, Phys. Rev. Lett. **87**, 176802 (2001).

[9] H. Ikegami, H. Akimoto, and K. Kono, *Nonlinear Transport of the Wigner Solid on Superfluid* ^{4}He *in a Channel Geometry*, Phys. Rev. Lett. **102**, 046807 (2009).

[10] D. G. Rees, N. R. Beysengulov, J.-J. Lin, and K. Kono, *Stick-Slip Motion of the Wigner Solid on Liquid Helium*, Phys. Rev. Lett. **116**, 206801 (2016).

[11] A. O. Badrutdinov, D. G. Rees, J. Y. Lin, A. V. Smorodin, and D. Konstantinov, *Unidirectional Charge Transport via Ripplonic Polarons in a Three-Terminal Microchannel Device*, Phys. Rev. Lett. **124**, 126803 (2020).

[12] H. Ikegami, H. Akimoto, D. G. Rees, and K. Kono, *Evidence for Reentrant Melting in a Quasi-One-Dimensional Wigner Crystal*, Phys. Rev. Lett. **109**, 236802 (2012).

[13] D. G. Rees, N. R. Beysengulov, Y. Teranishi, C.-S. Tsao, S.-S. Yeh, S.-P. Chiu, Y.-H. Lin, D. A. Tayurskii, J.-J. Lin, and K. Kono, *Structural order and melting of a quasi-one-dimensional electron system*, Phys. Rev. B **94**, 045139 (2016).

[14] F. R. Bradbury, M. Takita, T. M. Gurrieri, K. J. Wilkel, K. Eng, M. S. Carroll, and S. A. Lyon, *Efficient Clocked Electron Transfer on Superfluid Helium*, Phys. Rev. Lett. **107**, 266803 (2011).

[15] D. Kielpinski, C. Monroe, and D. J. Wineland, *Architecture for a large-scale ion-trap quantum computer*, Nature **417**, 709 (2002).

[16] D. G. Rees, I. Kuroda, C. A. Marrache-Kikuchi, M. Höfer, P. Leiderer, and K. Kono, *Point-Contact Transport Properties of Strongly Correlated Electrons on Liquid Helium*, Phys. Rev. Lett. **106**, 026803 (2011).

[17] M. W. Cole and M. H. Cohen, *Image-Potential-Induced Surface Bands in Insulators*, Phys. Rev. Lett. **23**, 1238–1241 (1969).

[18] V. Shikin, *Motion of Helium Ions near a Vapor-liquid Surface*, Zh. Eksp. Teor. Fiz **58**, 1748–1756 (1970).

[19] R. Williams, R. S. Crandall, and A. H. Willis, *Surface States of Electrons on Liquid Helium*, Phys. Rev. Lett. **26**, 7–9 (1971).

[20] R. Williams and R. S. Crandall, *Surface-State Lifetimes and Current Flow in Liquid Helium*, Phys. Rev. A **4**, 2024–2026 (1971).

[21] R. S. Crandall and R. Williams, *Properties of Electron Surface States on Liquid Helium*, Phys. Rev. A **5**, 2183–2190 (1972).

[22] W. T. Sommer and D. J. Tanner, *Mobility of Electrons on the Surface of Liquid* ^{4}He, Phys. Rev. Lett. **27**, 1345–1349 (1971).

[23] V. A. Buntar, V. N. Grigoriev, O. I. Kirichek, Y. Z. Kovdrya, Y. P. Monarkha, and S. S. Sokolov, *Kinetic properties of surface electrons over liquid helium under strong electron-electron interaction*, Journal of Low Temperature Physics **79**, 323–339 (1990).

[24] R. van Haren, G. Acres, P. Fozooni, A. Kristensen, M. Lea, P. Richardson, A. Valkering, and R. van der Heijden, *Conduction of electrons on liquid helium along channels produced by multi-layer microfabrication*, Physica B: Condensed Matter **249-251**, 656–659 (1998).

[25] T. R. Brown and C. C. Grimes, *Observation of Cyclotron Resonance in Surface-Bound Electrons on Liquid Helium*, Phys. Rev. Lett. **29**, 1233–1236 (1972).

[26] R. W. van der Heijden, M. C. M. van de Sanden, J. H. G. Surewaard, A. T. A. M. de Waele, H. M. Gijsman, and F. M. Peeters, *Quantum Magnetoconductance of a Nondegenerate Two-Dimensional Electron Gas*, Europhysics Letters (EPL) **6**, 75–80 (1988).

[27] E. Teske, Y. P. Monarkha, M. Seck, and P. Wyder, *Coulomb Narrowing of the Quantum Cyclotron Resonance in a Nondegenerate Two-Dimensional Electron Liquid*, Phys. Rev. Lett. **82**, 2772–2775 (1999).

[28] J. Klier, A. Würl, P. Leiderer, G. Mistura, and V. Shikin, *Cyclotron resonance for two-dimensional electrons on thin helium films*, Phys. Rev. B **65**, 165428 (2002).

[29] D. Konstantinov and K. Kono, *Novel Radiation-Induced Magnetoresistance Oscillations in a Nondegenerate Two-Dimensional Electron System on Liquid Helium*, Phys. Rev. Lett. **103**, 266808 (2009).

[30] L. V. Abdurakhimov, R. Yamashiro, A. O. Badrutdinov, and D. Konstantinov, *Strong Coupling of the Cyclotron Motion of Surface Electrons on Liquid Helium to a Microwave Cavity*, Phys. Rev. Lett. **117**, 056803 (2016).

[31] C. C. Grimes and G. Adams, *Evidence for a Liquid-to-Crystal Phase Transition in a Classical, Two-Dimensional Sheet of Electrons*, Phys. Rev. Lett. **42**, 795–798 (1979).

[32] C. Grimes, *Melting of a two-dimensional crystal of electrons*, Physica A: Statistical Mechanics and its Applications **106**, 102–107 (1981).

[33] R. Mehrotra, C. J. Guo, Y. Z. Ruan, D. B. Mast, and A. J. Dahm, *Density-dependent mobility of a two-dimensional electron fluid*, Phys. Rev. B **29**, 5239–5242 (1984).

[34] R. Mehrotra, B. M. Guenin, and A. J. Dahm, *Ripplon-Limited Mobility of a Two-Dimensional Crystal of Electrons: Experiment*, Phys. Rev. Lett. **48**, 641–644 (1982).

[35] C. C. Grimes and T. R. Brown, *Direct Spectroscopic Observation of Electrons in Image-Potential States Outside Liquid Helium*, Phys. Rev. Lett. **32**, 280–283 (1974).

[36] C. C. Grimes, T. R. Brown, M. L. Burns, and C. L. Zipfel, *Spectroscopy of electrons in image-potential-induced surface states outside liquid helium*, Phys. Rev. B **13**, 140–147 (1976).

[37] M. W. Cole, *Electronic surface states of liquid helium*, Rev. Mod. Phys. **46**, 451–464 (1974).

[38] W. Masselink, Y.-C. Chang, H. Morkoç, D. Reynolds, C. Litton, K. Bajaj, and P. Yu, *Shallow impurity levels in AlGaAs/GaAs semiconductor quantum wells*, Solid-State Electronics **29**, 205–214 (1986).

[39] D. Marty, *Stability of two-dimensional electrons on a fractionated helium surface*, Journal of Physics C: Solid State Physics **19**, 6097–6104 (1986).

[40] H. Ikezi and P. M. Platzman, *Stability of helium films charged with electrons*, Phys. Rev. B **23**, 1145–1148 (1981).

[41] F. Bridges and J. F. McGill, *Mobility of electrons on the surface of liquid helium*, Phys. Rev. B **15**, 1324–1339 (1977).

[42] H. J. Hovel, R. K. Willardson, and A. C. Beer, *Semiconductors and semimetals*, New York : Academic Press (1975).

[43] E. Cheng, M. W. Cole, and M. H. Cohen, *Binding of electrons to the surface of liquid helium*, Phys. Rev. B **50**, 1136–1142 (1994).

[44] Y. Monarkha and K. Kono. *Two-Dimensional Coulomb Liquids and Solids*, chapter 7. Wigner Solid. I. Dynamics on Rigid and Soft Interfaces. Springer-Verlag Berlin Heidelberg, (2004).

[45] L. D. Landau and L. M. Lifshitz, *Quantum Mechanics Non-Relativistic Theory, Third Edition: Volume 3*, Butterworth-Heinemann, 3 edition (1981).

[46] M. Saitoh, *Warm Electrons on the Liquid ^{4}He Surface*, Journal of the Physical Society of Japan **42**, 201–209 (1977).

[47] C. B. Clark, *Coulomb Interactions in the Uniform-Background Lattice Model*, Phys. Rev. **109**, 1133–1141 (1958).

[48] E. Wigner, *On the Interaction of Electrons in Metals*, Phys. Rev. **46**, 1002–1011 (1934).

[49] R. S. Crandall and R. Williams, *Crystallization of electrons on the surface of liquid helium*, Physics Letters A **34**, 404–405 (1971).

[50] P. M. Platzman and H. Fukuyama, *Phase diagram of the two-dimensional electron liquid*, Phys. Rev. B **10**, 3150–3158 (1974).

[51] R. C. Gann, S. Chakravarty, and G. V. Chester, *Monte Carlo simulation of the classical two-dimensional one-component plasma*, Phys. Rev. B **20**, 326–344 (1979).

[52] R. W. Hockney and T. R. Brown, *A lambda transition in a classical electron film*, Journal of Physics C: Solid State Physics **8**, 1813–1822 (1975).

[53] J. M. Kosterlitz and D. J. Thouless, *Ordering, metastability and phase transitions in two-dimensional systems*, Journal of Physics C: Solid State Physics **6**, 1181–1203 (1973).

[54] D. Pines and D. Bohm, *A Collective Description of Electron Interactions: II. Collective* vs *Individual Particle Aspects of the Interactions*, Phys. Rev. **85**, 338–353 (1952).

[55] L. Bonsall and A. A. Maradudin, *Some static and dynamical properties of a two-dimensional Wigner crystal*, Phys. Rev. B **15**, 1959–1973 (1977).

[56] K. R. Atkins, *THE SURFACE TENSION OF LIQUID HELIUM*, Canadian Journal of Physics **31**, 1165–1169 (1953).

[57] E. Krotscheck, S. Stringari, and J. Treiner, *Ripplon dispersion and finite-range effects in the quantum-liquid surface*, Phys. Rev. B **35**, 4754–4763 (1987).

[58] D. O. Edwards, J. R. Eckardt, and F. M. Gasparini, *Surface excitations and surface tension of superfluid* He^4, Phys. Rev. A **9**, 2070–2077 (1974).

[59] A. Lastri, F. Dalfovo, L. Pitaevskii, and S. Stringari, *Dispersion of ripplons in superfluid4He*, Journal of Low Temperature Physics **98**, 227–250 (1995).

[60] H. J. Lauter, H. Godfrin, V. L. P. Frank, and P. Leiderer, *Ripplons in* ^{4}He *films observed by neutron scattering*, Phys. Rev. Lett. **68**, 2484–2487 (1992).

[61] D. Edwards and W. Saam. *Chapter 4 The Free Surface of Liquid Helium*. volume 7 of *Progress in Low Temperature Physics*, pages 283–369. Elsevier, (1978).

[62] A. Tamura, *The ripplon and surface tension of a liquid*, Journal of Physics: Condensed Matter **10**, 10135–10140 (1998).

[63] M. W. Cole, *Properties of Image-Potential-Induced Surface States of Insulators*, Phys. Rev. B **2**, 4239–4252 (1970).

[64] Y. P. Monarkha, S. S. Sokolov, A. V. Smorodin, and N. Studart, *Decay of excited surface electron states in liquid helium and related relaxation phenomena induced by short-wavelength ripplons*, Low Temperature Physics **36**, 565–575 (2010).

[65] T. Ando, *Broadening of Inter-Subband Transitions in Image-Potential-Induced Surface States outside Liquid Helium*, Journal of the Physical Society of Japan **44**, 765–773 (1978).

[66] V. B. Shikin and Y. P. Monarkha, *On the interaction of surface electrons in liquid helium with oscillations of the vapor-liquid interface*, Journal of Low Temperature Physics **16**, 193–208 (1974).

[67] M. Abramowitz, *Handbook of Mathematical Functions, With Formulas, Graphs, and Mathematical Tables,*, Dover Publications, Inc., USA (1974).

[68] M. I. Dykman and Y. G. Rubo, *Bragg-Cherenkov Scattering and Nonlinear Conductivity of a Two-Dimensional Wigner Crystal*, Phys. Rev. Lett. **78**, 4813–4816 (1997).

[69] J.-Y. Lin, A. V. Smorodin, A. O. Badrutdinov, and D. Konstantinov, *Sliding of an electron crystal of finite size on the surface of superfluid* ^{4}He *confined in a microchannel*, Phys. Rev. B **98**, 085412 (2018).

[70] E. Collin, W. Bailey, P. Fozooni, P. G. Frayne, P. Glasson, K. Harrabi, M. J. Lea, and G. Papageorgiou, *Microwave Saturation of the Rydberg States of Electrons on Helium*, Phys. Rev. Lett. **89**, 245301 (2002).

[71] J. R. Petta, A. C. Johnson, J. M. Taylor, E. A. Laird, A. Yacoby, M. D. Lukin, C. M. Marcus, M. P. Hanson, and A. C. Gossard, *Coherent Manipulation of Coupled Electron Spins in Semiconductor Quantum Dots*, Science **309**, 2180–2184 (2005).

[72] H. Ikegami, H. Akimoto, and K. Kono, *Nonlinear Transports of Electrons on Liquid* ^{4}He *in a 1.6µm Channel*, Journal of Physics: Conference Series **400**, 012020 (2012).

[73] J.-Y. Lin, A. V. Smorodin, A. O. Badrutdinov, and D. Konstantinov, *Transport Properties of a Quasi-1D Wigner Solid on Liquid Helium Confined in a Microchannel with Periodic Potential*, Journal of Low Temperature Physics **195**, 289–299 (2019).

[74] A. O. Badrutdinov, A. V. Smorodin, D. G. Rees, J. Y. Lin, and D. Konstantinov, *Nonlinear transport of the inhomogeneous Wigner solid in a channel geometry*, Phys. Rev. B **94**, 195311 (2016).

[75] S. S. Sokolov and N. Studart, *Electron transport in a quasi-one-dimensional channel on suspended helium films*, Phys. Rev. B **66**, 075424 (2002).

[76] F. Pobell, *Matter and Methods at Low Temperatures*, Springer-Verlag Berlin Heidelberg, 3 edition (2007).

[77] H. Etz, W. Gombert, W. Idstein, and P. Leiderer, *Stability of Charged* ^{4}He *Films*, Phys. Rev. Lett. **53**, 2567–2570 (1984).

[78] X. L. Hu and A. J. Dahm, *Stability of charged thin helium films*, Phys. Rev. B **42**, 2010–2013 (1990).

[79] A. Rybalko and Y. Kovdrya, *Absorption of Electromagnetic Field Energy by an Ensemble of Electrons on the Liquid Helium Surface*, Sov. J. Low Temp. Phys. **5**, 450 (1979).

[80] F. Williams, *Collective aspects of charged-particle systems at helium interfaces*, Surface Science **113**, 371–388 (1982).

[81] V. S. Edel'man and M. I. Faley, *Investigation of electrons localized above solid hydrogen by means of the cyclotron resonance method*, Journal of Low Temperature Physics **52**, 301 (1983).

[82] K. Kono, U. Albrecht, and P. Leiderer, *Surface-state electrons on a hydrogen film. 1. Annealing of the film*, Journal of Low Temperature Physics **82**, 279 (1991).

[83] K. Kono, U. Albrecht, and P. Leiderer, *Surface state electrons on a hydrogen film. 2. Influence of adsorbed helium films*, Journal of Low Temperature Physics **85**, 423 (1991).

[84] A. M. Troyanovskii and M. S. Khalkin, *Electron mobility in two-dimensional layer over the surface of solid hydrogen*, Sov. Phys. JETP **54**, 214 (1981).

[85] K. Kajita, *A new two-dimensional electron system on the surface of solid neon*, Surface Science **142**, 86–95 (1984).

[86] K. Shirahama and K. Kono, *Sliding wigner solid on liquid ^4He*, Journal of Low Temperature Physics **104**, 237 (1996).

[87] M. J. Lea, P. Fozooni, A. Kristensen, P. J. Richardson, K. Djerfi, M. I. Dykman, C. Fang-Yen, and A. Blackburn, *Magnetoconductivity of two-dimensional electrons on liquid helium:Experiments in the fluid phase*, Phys. Rev. B **55**, 16280–16292 (1997).

[88] O. I. Kirichek, K. Shirahama, and K. Kono, *Plasma Resonance of the Wigner Solid on the Free Surface of Normal and Superfluid ^3He*, Journal of Low Temperature Physics **113**, 1103 (1998).

[89] E. Rousseau, D. Ponarin, L. Hristakos, O. Avenel, E. Varoquaux, and Y. Mukharsky, *Addition spectra of Wigner islands of electrons on superfluid helium*, Phys. Rev. B **79**, 045406 (2009).

[90] H. Ikegami, H. Akimoto, and K. Kono, *Melting of a quasi-one-dimensional Wigner crystal: Electrons on superfluid ^4He in a narrow channel*, Phys. Rev. B **82**, 201104 (2010).

[91] D. G. Rees, S.-S. Yeh, B.-C. Lee, S. K. Schnyder, F. I. B. Williams, J.-J. Lin, and K. Kono, *Dynamical decoupling and recoupling of the Wigner solid to a liquid helium substrate*, Phys. Rev. B **102**, 075439 (2020).

[92] S. Zou, D. Konstantinov, and D. G. Rees, *Dynamical ordering in a two-dimensional electron crystal confined in a narrow channel geometry*, Phys. Rev. B **104**, 045427 (2021).

[93] K. Shirahama and K. Kono, *Dynamical Transition in the Wigner Solid on a Liquid Helium Surface*, Phys. Rev. Lett. **74**, 781–784 (1995).

[94] A. Kristensen, K. Djerfi, P. Fozooni, M. J. Lea, P. J. Richardson, A. Santrich-Badal, A. Blackburn, and R. W. van der Heijden, *Hall-Velocity Limited Magnetoconductivity in a Classical Two-Dimensional Wigner Crystal*, Phys. Rev. Lett. **77**, 1350–1353 (1996).

[95] D. Konstantinov, H. Isshiki, Y. Monarkha, H. Akimoto, K. Shirahama, and K. Kono, *Microwave-Resonance-Induced Resistivity: Evidence of Ultrahot Surface-State Electrons on Liquid ^3He*, Phys. Rev. Lett. **98**, 235302 (2007).

[96] D. Konstantinov, M. I. Dykman, M. J. Lea, Y. Monarkha, and K. Kono, *Resonant Correlation-Induced Optical Bistability in an Electron System on Liquid Helium*, Phys. Rev. Lett. **103**, 096801 (2009).

[97] H. Isshiki, D. Konstantinov, H. Akimoto, K. Shirahama, and K. Kono, *Microwave Absorption of Surface-State Electrons on Liquid 3He*, Journal of the Physical Society of Japan **76**, 094704 (2007).

[98] D. Konstantinov and K. Kono, *Melting of Two-Dimensional Electron Crystal on Liquid 3He Induced by Resonance Microwave Absorption*, Journal of Low Temperature Physics **150**, 236 (2008).

[99] A. Elarabi, E. Kawakami, and D. Konstantinov, *Cryogenic amplification of image-charge detection for readout of quantum states of electrons on liquid helium*, Journal of Low Temperature Physics **202**, 456–465 (2021).

[100] R. J. Schoelkopf, P. Wahlgren, A. A. Kozhevnikov, P. Delsing, and D. E. Prober, *The Radio-Frequency Single-Electron Transistor (RF-SET): A Fast and Ultrasensitive Electrometer*, Science **280**, 1238–1242 (1998).

[101] X. Feng, M. Charlton, M. Holzscheiter, R. A. Lewis, and Y. Yamazaki, *Tank circuit model applied to particles in a Penning trap*, Journal of Applied Physics **79**, 8–13 (1996).

[102] S. Ulmer, H. Kracke, K. Blaum, S. Kreim, A. Mooser, W. Quint, C. C. Rodegheri, and J. Walz, *The quality factor of a superconducting rf resonator in a magnetic field*, Review of Scientific Instruments **80**, 123302 (2009).

[103] G. Grandi, M. Kazimierczuk, A. Massarini, and U. Reggiani, *Stray capacitances of single-layer solenoid air-core inductors*, IEEE Transactions on Industry Applications **35**, 1162–1168 (1999).

[104] J. Young and C. Butler, *Inductance of a shielded coil*, IEEE Transactions on Antennas and Propagation **49**, 944–953 (2001).

[105] W. W. Macalpine and R. O. Schildknecht., *Coaxial resonators with helical inner conductor*, Proceedings of the IRE **47**, 2099 (1959).

[106] J. D. Siverns, L. R. Simkins, S. Weidt, and W. K. Hensinger, *On the application of radio frequency voltages to ion traps via helical resonators*, Applied Physics B **107**, 921–934 (2012).

[107] G. Grandi, M. Kazimierczuk, A. Massarini, and U. Reggiani, *Stray capacitances of single-layer air-core inductors for high-frequency applications*, **3**, 1384–1388 vol.3 (1996).

[108] G. Gabrielse, X. Fei, L. A. Orozco, R. L. Tjoelker, J. Haas, H. Kalinowsky, T. A. Trainor, and W. Kells, *Cooling and slowing of trapped antiprotons below 100 meV*, Phys. Rev. Lett. **63**, 1360–1363 (1989).

[109] R. M. Weisskoff, G. P. Lafyatis, K. R. Boyce, E. A. Cornell, R. W. Flanagan, and D. E. Pritchard, *rf SQUID detector for single-ion trapping experiments*, Journal of Applied Physics **63**, 4599–4604 (1988).

[110] S. R. Jefferts, T. Heavner, P. Hayes, and G. H. Dunn, *Superconducting resonator and a cryogenic GaAs field-effect transistor amplifier as a single-ion detection system*, Review of Scientific Instruments **64**, 737–740 (1993).

[111] A. Weigel. *Development of the cryogenic detection system for ALPHATRAP and THe-Trap.* PhD thesis, University of Heidelberg, (2014).

[112] J.-Y. Lin, A. V. Smorodin, A. O. Badrutdinov, and D. Konstantinov, *Architecture for a large-scale ion-trap quantum computer*, Journal of Low Temperature Physics **195**, 289 (2019).

[113] N. R. Beysengulov, D. G. Rees, Y. Lysogorskiy, N. K. Galiullin, A. S. Vazjukov, D. A. Tayurskii, and K. Kono, *Structural Transitions in a Quasi-1D Wigner Solid on Liquid Helium*, Journal of Low Temperature Physics **182**, 28–37 (2016).